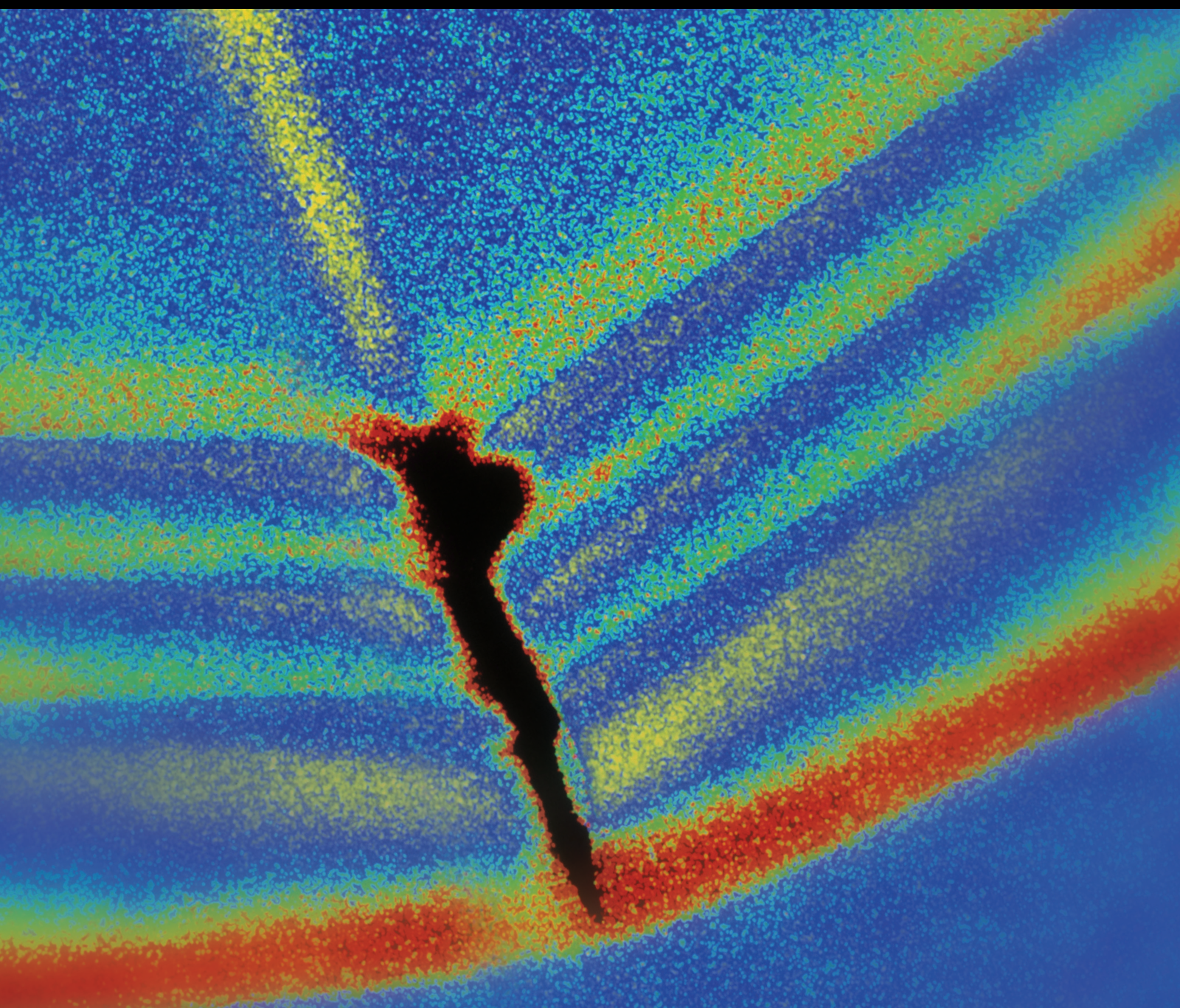


Shock and Vibration

Damage Models and Assessment Methods

Guest Editors: Gilbert-Rainer Gillich, Magd Abdel Wahab, Ruqiang Yan,
and José V. Araújo dos Santos





Damage Models and Assessment Methods

Shock and Vibration

Damage Models and Assessment Methods

Guest Editors: Gilbert-Rainer Gillich, Magd Abdel Wahab,
Ruqiang Yan, and José V. Araújo dos Santos



Copyright © 2016 Hindawi Publishing Corporation. All rights reserved.

This is a special issue published in "Shock and Vibration." All articles are open access articles distributed under the Creative Commons Attribution License, which permits unrestricted use, distribution, and reproduction in any medium, provided the original work is properly cited.

Editor-in-Chief

Mehdi Ahmadian, Virginia Polytechnic Institute and State University, USA

Editorial Board

Brij N. Agrawal, USA
Marco Alfano, Italy
Farbod Alijani, Canada
Sumeet S. Aphale, UK
Mariano Artés, Spain
Hassan Askari, Canada
Matteo Aureli, USA
Ranjan Banerjee, UK
Mahmoud Bayat, Iran
José A. Becerra Villanueva, Spain
Marco Belloli, Italy
Subhamoy Bhattacharya, UK
Ivo Caliò, Italy
Antonio Carcaterra, Italy
Dumitru I. Caruntu, USA
Noel Challamel, France
Athanasios Chasalevris, UK
Peng Chen, Japan
Ashwin Chinnayya, France
Giorgio Dalpiaz, Italy
Farhang Daneshmand, Canada
Sergio De Rosa, Italy
Dario Di Maio, UK
Longjun Dong, China
Lorenzo Dozio, Italy
Mohamed El badaoui, France
Mohammad Elahinia, USA
Fiorenzo A. Fazzolari, UK

Francesco Franco, Italy
Alessandro Gasparetto, Italy
Gianluca Gatti, Italy
Anindya Ghoshal, USA
Nere Gil-Negrete, Spain
Hassan Haddadpour, Iran
M.I. Herreros, Spain
Hamid Hosseini, Japan
Ian M. Howard, Australia
Reza Jazar, Australia
Sakdirat Kaewunruen, UK
Yuri S. Karinski, Israel
Jeong-Hoi Koo, USA
Georges Kouroussis, Belgium
Mickaël Lallart, France
Kenneth J. Loh, USA
Nuno M. Maia, Portugal
Giuseppe C. Marano, Italy
Laurent Mevel, France
Emiliano Mucchi, Italy
Tony Murmu, UK
Sundararajan Natarajan, India
Toshiaki Natsuki, Japan
Miguel Neves, Portugal
Coral Ortiz, Spain
Gyuhae Park, Republic of Korea
Aleksandar Pavic, UK
Evgeny Petrov, UK

Antonina Pirrotta, Italy
Vitamor Racic, UK
Carlo Rainieri, Italy
Didier Rémond, France
Francesco Ripamonti, Italy
Salvatore Russo, Italy
Edoardo Sabbioni, Italy
Jerzy T. Sawicki, USA
Onome E. Scott-Emuakpor, USA
Vadim V. Silberschmidt, UK
Kumar V. Singh, USA
Isabelle Sochet, France
Alba Sofi, Italy
Jussi Sopanen, Finland
Stefano Sorace, Italy
Narakorn Srinil, UK
Salvatore Strano, Italy
Chao Tao, China
Mario Terzo, Italy
Tai Thai, Australia
Carlo Trigona, Italy
Federica Tubino, Italy
Nerio Tullini, Italy
Marcello Vanali, Italy
Jörg Wallaschek, Germany
Zaili L. Yang, UK
Stana Živanović, UK
Lei Zuo, USA

Contents

Damage Models and Assessment Methods

Gilbert-Rainer Gillich, Magd Abdel Wahab, Ruqiang Yan, and José V. Araújo dos Santos
Volume 2016, Article ID 1748712, 1 page

Finite Element Model Fractional Steps Updating Strategy for Spatial Lattice Structures Based on Generalized Regression Neural Network

Caiwei Liu, Jijun Miao, and Changyong Zhao
Volume 2016, Article ID 5845326, 10 pages

Planetary Gearbox Fault Diagnosis Using Envelope Manifold Demodulation

Weigang Wen, Robert X. Gao, and Weidong Cheng
Volume 2016, Article ID 3952325, 13 pages

Development of a Vehicle-Bridge-Soil Dynamic Interaction Model for Scour Damage Modelling

L. J. Prendergast, D. Hester, and K. Gavin
Volume 2016, Article ID 7871089, 15 pages

Undecimated Lifting Wavelet Packet Transform with Boundary Treatment for Machinery Incipient Fault Diagnosis

Lixiang Duan, Yangshen Wang, Jinjiang Wang, Laibin Zhang, and Jinglong Chen
Volume 2016, Article ID 9792807, 9 pages

Experimental Study on Progressive Collapse Performance of Frame with Specially Shaped Columns Subjected to Middle Column Removal

Tiecheng Wang, Qingwei Chen, Hailong Zhao, and Lei Zhang
Volume 2016, Article ID 7956189, 13 pages

Experimental Design and Validation of an Accelerated Random Vibration Fatigue Testing Methodology

Yu Jiang, Gun Jin Yun, Li Zhao, and Junyong Tao
Volume 2015, Article ID 147871, 13 pages

Editorial

Damage Models and Assessment Methods

Gilbert-Rainer Gillich,¹ Magd Abdel Wahab,² Ruqiang Yan,³ and José V. Araújo dos Santos⁴

¹*Department of Mechanics, “Eftimie Murgu” University of Resita, Resita, Romania*

²*Laboratory Soete, Faculty of Engineering and Architecture, Ghent University, Belgium*

³*School of Instrument Science and Engineering, Southeast University, Nanjing, China*

⁴*Instituto Superior Técnico, Universidade de Lisboa, Portugal*

Correspondence should be addressed to Gilbert-Rainer Gillich; gr.gillich@uem.ro

Received 8 October 2015; Accepted 8 October 2015

Copyright © 2016 Gilbert-Rainer Gillich et al. This is an open access article distributed under the Creative Commons Attribution License, which permits unrestricted use, distribution, and reproduction in any medium, provided the original work is properly cited.

Damage assessment based on the vibration response of structures has been, in the last decades, an important research area in various engineering branches. It integrates knowledge from a variety of disciplines, such as mechanical and structural engineering, material science, computer science and signal processing, and data management. This special issue is dedicated to fundamental understanding of the vibrational behavior of damaged structures and to the development of methods and techniques that are able to tackle these specific problems. A number of 23 papers have been submitted, from which a total of 7 papers have been finally selected to integrate the present issue. Two among them are focused on failures in machineries: W. Wen et al. in the paper “Planetary Gearbox Fault Diagnosis Using Envelope Manifold Demodulation” extract fault characteristics from the vibration signals, since in “Undecimated Lifting Wavelet Packet Transform with Boundary Treatment for Machinery Incipient Fault Diagnosis” by L. Duan et al. a Volterra series assisted undecimated lifting wavelet packet transform is investigated for machinery incipient fault diagnosis. The presented approaches dramatically enhance the weak defect feature extraction. Damages in structural elements are the target of research presented in “Development of a Vehicle-Bridge-Soil Dynamic Interaction Model for Scour Damage Modelling” by L. Prendergast et al., “Feature Recognition for Mine Hoisting Wire Rope Based on Magnetic Flux Leakage Signals” by Z. Zhao et al., and “Experimental Study on Progressive Collapse Performance of Frame with Specially Shaped Columns Subjected to Middle Column Removal” by T. Wang et al. A model updating

strategy for bolt-ball joint stiffness characterization for health monitoring is presented in “Finite Element Model Fractional Steps Updating Strategy for Spatial Lattice Structures Based on Generalized Regression Neural Network” by C. Liu et al. An interesting method to perform efficient fatigue tests is proposed by Y. Jiang et al. in the paper “Experimental Design and Validation of an Accelerated Random Vibration Fatigue Testing Methodology.” They succeed to significantly reduce the test time and the sample size. The papers reflect, without doubt, significant researches and developments of this subject. We hope that readers will find all articles of the special issue useful and exciting and that the articles will stimulate further research activities in the area of damage assessment.

Acknowledgments

Acknowledgments are due to all the authors and coauthors of this special issue for their contribution.

*Gilbert-Rainer Gillich
Magd Abdel Wahab
Ruqiang Yan
José V. Araújo dos Santos*

Research Article

Finite Element Model Fractional Steps Updating Strategy for Spatial Lattice Structures Based on Generalized Regression Neural Network

Caiwei Liu, Jijun Miao, and Changyong Zhao

College of Civil Engineering, Qingdao Technological University, Qingdao 266033, China

Correspondence should be addressed to Caiwei Liu; 03150053@163.com

Received 1 July 2015; Revised 22 September 2015; Accepted 28 September 2015

Academic Editor: Magd Abdel Wahab

Copyright © 2016 Caiwei Liu et al. This is an open access article distributed under the Creative Commons Attribution License, which permits unrestricted use, distribution, and reproduction in any medium, provided the original work is properly cited.

In order to get a more accurate finite element model of a spatial lattice structure with bolt-ball joints for health monitoring, a method of modifying the bolt-ball joint stiffness coefficient was proposed. Firstly, the beam element with adjustable stiffness was used in the joint zone in this paper to reveal the semirigid characteristic of the joint. Secondly, the value of stiffness reduction factor (a_r) was limited in the range of [0.2, 0.8] and the reference value ($a_{r,0}$) of it was suggested to be 0.5 based on referenced literatures. Finally, the finite element model fractional steps updating strategy based on neural network technique was applied and the limited measuring point information was used to form the network input parameter. A single-layer latticed cylindrical shell model with 157 joints and 414 tubes was used in a shaking TABLE test. Based on the measured modal data, the presented method was verified. The results show that this model updating technique can reflect the true dynamic characters of the shell structure better. Moreover, the neural network can be simplified considerably by using this algorithm. The method can be used for model updating of a latticed shell with bolt-ball joints and has great value in engineering practice.

1. Introduction

Structural health monitoring is becoming increasingly important, not only in the prevention of catastrophic failures, but also in improving maintainability of aerospace, civil, and mechanical infrastructure. An improved understanding of the capacity and performance of a structure within its serviceability limit states is a critical need and most often implemented by means of structural identification (STI) [1].

A typical STI application involves the determination of the modified parameters of a structure and subsequent revision of its finite element model accordingly, such that the improved (calibrated) model accurately simulates the response of the structure, as verified from field measurements [2]. It is crucial that the models are calibrated through STI procedures to permit reliable simulations and genuine performance assessments.

A good finite element model that accurately predicts the dynamic response of an actual structure is a prerequisite for many damage detection techniques. Structural model

updating refines an analytical model using test data to better predict the dynamic behavior of a structure. In the last decade, finite element model updating has been intensively researched, and robust methods are now available to calculate adequate values of the selected model parameters from experimental data. Artificial neural networks (ANNs) have been successfully implemented in STI and model updating studies in the literature [3–6].

In real engineering projects, especially in long-span spatial structures, there are plenty of tubes and nodes; therefore, the number of parameters that need to be updated is large, which causes increase in the processing time and reduces the efficiency and accuracy of prediction, and the samples would lead to data explosion when training the ANN [7].

In order to solve this problem, fractional steps model updating method for different engineering structures is proposed. Both the substructure method and radial basis function neural network (RBF) were introduced into finite element model updating of single pylon cable-stayed bridges [4], which simplified the process of model updating and

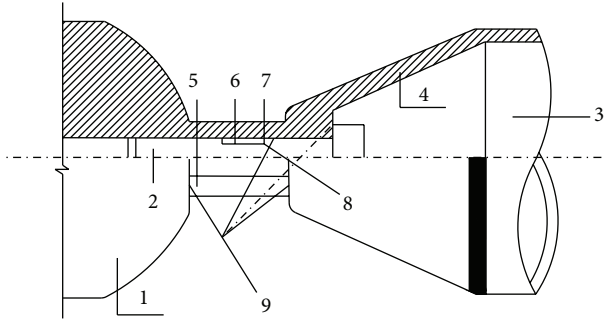


FIGURE 1: Bolt-ball joint with ball (1), ball (2), high strength bolt (3), steel tube (4), sleeve (5), end cone (6), slot (7), dowel pin (8), and deep-rich (9) contact surfaces.

greatly improved the updating efficiency. A stepwise model updating method based on substructures and ANN was presented by He et al. [6]. A single-layer reticulated dome was first divided into multilayer substructures, and model updating was then done step by step according to appropriate damage factors. However, only the elasticity modulus of tubes was updated.

There are also researches on updating the finite element models of structures with semirigid joints. In order to consider both the moment-rotation and shear-displacement characteristics of such joints, a hybrid finite element was proposed by Liu et al. [8]. Both of the characteristics of semirigid joints could be simulated by this element. However, due to the complicated operation, it is inconvenient for engineering application.

With the major advantages of material saving, aesthetic appearance, high construction speed, and high fabrication accuracy, single-layer latticed shells with bolt-ball joints are outstanding spatial structures [9]. Figure 1 illustrates the detailed structure.

Four types of fine bolt-ball joint finite element models were developed according to joints in a shaking TABLE experiment model of a single-layer latticed cylindrical shell with 157 joints and 414 tubes [10]. The friction coefficient and contact were used to simulate the sliding between the high-strength bolts and steel ball. The influences of the dowel pin and pretightening force were ignored. The $M-\theta$ (bending moment and rotating angle) curve of the bolt-ball connections was obtained. The connection was simplified to a joint element with the same inertia moment I ; the elastic modulus of the joint element was determined from the obtained curve.

When the friction coefficient and contact parameters were determined according to the results of repeated trials, the stiffness reduction factors of the four types of bolt-ball joints were obtained (i.e., 0.524, 0.466, 0.317, and 0.122). By using these factors, sound model updating results could be determined. However, this method is still not practical for engineering applications, as the modeling process is complicated, even with a number of stiffness reduction factors and simplified assumptions. In fact, there is a difference in the bolt tightness due to manual operation, which cannot be simulated correctly by this model.

The spatial lattice structure with bolt-ball joints has the characteristics of modeling difficulty and plenty of tubes and nodes. In order to get a more accurate finite element model of a spatial lattice structure with bolt-ball joints for health monitoring, a new method that is suitable for the spatial lattice structure was proposed in this paper and then was used to analyze experimental results of a single-layer latticed cylindrical shell model with 157 joints and 414 tubes tested using a shaking TABLE. Based on the measured modal data, the presented method was verified. The results show that this model updating technique can reflect the true dynamic characters of the shell structure better. Moreover, use of the general regression neural networks (GRNN) for model updating can be simplified considerably by using this approach. The method can be used for model updating of a latticed shell with bolt-ball joints and has great value in engineering practice.

2. Construction of Semirigid Model

In analysis of space structures, conventional designs and analyses of lattice shell structures are based on such an assumption that the connection behaves as either a pinned or rigid joint. However, the joints in most of the space structures are semirigid and their actual behaviors do not conform to either of the two extremities. A bolt-ball joint system with partial bend-bearing capacity is a typical semirigid joint system, which may be the main reason for the large difference in the results from dynamic testing and numerical simulation.

The accuracy of the finite element model of a spatial lattice structure depends on the connection mode between the tubes and the bolt ball. Figure 1 illustrates the detailed structure. The beam element with adjustable stiffness is used in the joint zone to reveal the semirigid characteristic of the joint, as shown in Figure 2. And then take the boundary conditions, the load cases, material property, and so on into consideration; the finite element model is finally constructed, which is called a semirigid model in this paper. L is the length of the element; a is the stiffness reduction factor (the joint element-member element stiffness ratio), where $0 < a < 1$. EI is the element stiffness of the member; aEI is the element stiffness of the joint, with coefficient a defined considering the friction coefficient, contact parameters, and prestress force.

3. Updating Strategy Basing on GRNN

3.1. ANN and GRNN. An ANN is a biologically inspired information processing system that mimics a biological nerve system to exploit the imprecision and uncertainty of problems for deriving valuable and robust models [11]. It is composed of a large number of highly interconnected processing elements that are tied together with weighted connections and work in parallel to solve specific problems.

ANNs are particularly suitable for situations where conventional constitutive modeling may be insufficient, tedious, or time consuming. One of their distinctive characteristics is the ability to learn even in cases of erroneous, incomplete, or fuzzy data and make a reliable prediction on datasets not previously seen [12, 13]. Their unique learning and prediction

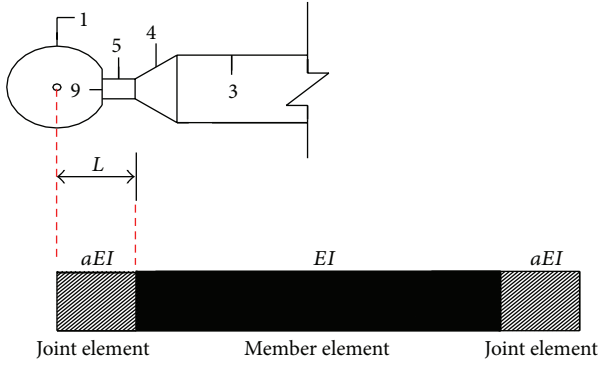


FIGURE 2: Joint element with adjustable stiffness parameters.

characteristics make them a popular tool for modeling problems encountered in various applications of civil and structural engineering.

GRNN has been proposed by Specht [14]. It uses a radial basis activation function, requires less training parameters, is difficult to become the local minimum, and is probabilistic compared to the traditional ANN [15, 16]. GRNN is often a three-layer network in which there must be one hidden neuron for each training pattern. The GRNN is a type of supervised network and also trains quickly on sparse datasets, but rather than categorizing them, GRNN applications are able to create continuous valued outputs [17]. A principal advantage of GRNN is that they involve a one-pass learning algorithm and are consequently much faster to train than the well-known back-propagation paradigm [14]. Furthermore, they differ from classical neural networks in that every weight is replaced by a distribution of weights. GRNN is related to the RBF, based on a standard statistical technique called Gaussian kernel regression [18].

3.2. Determination of GRNN Input Parameters. A structure's natural frequency can be readily obtained by testing, and the value is relatively accurate. The frequency can reflect the dynamic characteristics of the whole structure; therefore, it is a good input parameter in model updating based on ANN [19]. However, the change of mode shape is very sensitive to structural damage, which is critical when a large spatial lattice structure is undergoing damage detection. Therefore, it is necessary to adopt a reasonable combination of frequency and mode as the input parameters according to the characteristics of a spatial lattice structure. The updated model requires that the natural frequency be close to the measured data and that the modal assurance criterion (MAC) value should be close to 1 as possible [1].

In this paper, the combined parameters of frequency and mode (CPFM) are adopted as the GRNN input as follows:

$$\begin{aligned} \text{CPFM} \\ = \{ \text{FRE}_1, \text{FRE}_2, \dots, \text{FRE}_m; \text{DF}_1, \text{DF}_2, \dots, \text{DF}_n \}, \end{aligned} \quad (1)$$

where m is the order of the frequency; n is the order of the mode shape; FRE_i ($i = 1, 2, \dots, m$) is the i th order frequency; and $\text{DF}_i = (\varphi_{i1}, \varphi_{i2}, \dots, \varphi_{iq})$ and is the normalized modal

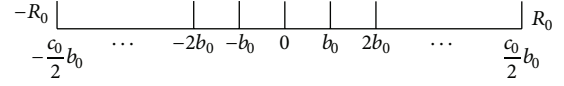


FIGURE 3: Variation ranges and steps.

vector of the q measured degrees of freedom in the i th order mode, which is calculated with the following formula:

$$\varphi_{ij} = \frac{\varphi_{ij}}{(\varphi_{ij})_{\max}} \quad (j = 1, 2, \dots, q), \quad (2)$$

where φ_{ij} is the j th degree of freedom component in the i th order mode.

For spatial lattice structures, the modes are complicated and dense, and the high order modes are difficult to excite and identify. Based on engineering testing, the order of the natural frequency should be less than the first five ($m \leq 5$) and the modal shape should be less than the first three ($n \leq 3$) to ensure the validity of the measured data [20]. A relatively simple vibration form in these ranges is preferable.

3.3. Fractional Step Updating Algorithm. The modal calculation of a spatial lattice structure with a semirigid joint was carried out with joint bending stiffness in different testing samples: that is, $a_{r0} \times (1 - (c_0/2)b_0)EI_r, \dots, a_{r0} \times (1 - b_0)EI_r, a_{r0} \times 1.0EI_r, a_{r0} \times (1 + b_0)EI_r, \dots, a_{r0} \times (1 + (c_0/2)b_0)EI_r$ ($r = 1, 2, \dots, p$, where EI is the member element bending stiffness, a_r ($r = 1, 2, \dots, p$, with p as the number of corrected parameters) is the reference value of a stiffness reduction factor assumed to be a_{r0} , b_0 is the step of training samples within the variation range of $[-R_0, R_0]$ ($R_0 < 1$), and c_0 is the number of steps, as shown in Figure 3).

Applying the calculated CPFM as the input of the GRNN, the corresponding joint stiffness reduction factor can be obtained as the output, and according to these values, the sample database for the relationship between the CPFM and the joint stiffness reduction factor can be established. The number of training samples is $(C_{(c_0+1)}^1)^p$, “ $C_0 + 1$ ” stands for the total numbers of certain corrected parameters, and “1” stands for one of the total numbers of certain corrected parameters, when a one-step updating algorithm (model updating in a single step) is adopted; however, the one-step updating algorithm induces a data explosion and decreases the nonlinear mapping capacity when it is applied to a spatial lattice structure with multiple parameters, although it is theoretically feasible.

The fractional steps updating algorithm is proposed in this paper, in order to alleviate the data explosion and mitigate the loss of mapping capacity. The detailed procedure of n th updating steps is described in the following paragraphs.

In the first updating, a_r is set to a_{r0} , the step of training samples is set to b_1 in the variation range of $[-R_0, R_0]$ ($R_0 < 1$), and c_1 is the number of steps. $a_{r0} \times (1 - (c_1/2)b_1)EI_r, \dots, a_{r0} \times (1 - b_1)EI_r, a_{r0} \times 1.0EI_r$, and $a_{r0} \times (1 + b_1)EI_r, \dots, a_{r0} \times (1 + (c_1/2)b_1)EI_r$ (where $r = 1, 2, \dots, p$) are put into the model of a spatial lattice structure with a semirigid joint; the modal calculation is then carried out.

Sample database A_1 on the relationship between the CPFM and the joint element stiffness reduction factor is established. The calculated CPFM is the input of the GRNN, and the corresponding stiffness reduction factor of the joint is the output, which is used to train the GRNN. The CPFM input of the GRNN is obtained from the results based on the measured modal data of the spatial latticed structure, and the output is the initial updating result of the stiffness reduction factor, namely, a_{r1} (where $r = 1, 2, \dots, p$).

In the second updating, the corresponding stiffness reduction factor is a_{r1} , the step of training samples is set to b_2 within the variation range of $[-R_1, R_1]$ ($R_1 < R_0$), and c_2 is the number of steps. $a_{r1} \times (1 - (c_2/2)b_2)EI_r, \dots, a_{r1} \times (1 - b_2)EI_r, a_{r1} \times 1.0EI_r$, and $a_{r1} \times (1 + b_2)EI_r, \dots, a_{r1} \times (1 + (c_2/2)b_2)EI_r$ are put into the semirigid model of the spatial lattice structure. The modal calculation is then carried out; sample database A_2 is established.

Similarly, the next updating results of the stiffness reduction factor, namely, a_{r2} , can be obtained. This continues with n th updating steps and building sample database A_n and the n th updating results of the stiffness reduction factor can be obtained, namely, a_{rn} .

When a_{r0} is in the range of $[-60\%, 60\%]$, $b_0 = 0.1$, $c_0 = 12$, and $p = 3$, the number of GRNN samples under a one-step algorithm is the value of $(C_{13}^1)^3$, which is 2197. However, when the updating is divided into three steps, namely, $R_0 = 0.6$, $b_1 = 0.6$, and $c_1 = 2$; $R_1 = 0.3$, $b_2 = 0.3$, and $c_2 = 2$; and $R_2 = 0.1$, $b_3 = 0.6$, and $c_3 = 2$, the number of GRNN samples in each step is $(C_3^1)^3$, that is, 27. Thus, the total number of samples is $3 \times 3 \times C_3^1$, that is, 81.

The ratio of the number of samples between the two types of algorithms is 0.0123 (27/2197); the ratio of the total number of samples is 0.0369 (81/2197). Obviously, the fractional steps updating algorithm greatly reduces the number of training samples. Moreover, the advantages of the fractional steps updating algorithm are more significant when the number of parameters is larger (with increasing p).

3.4. Convergence Criteria and Flowchart. Based on engineering testing and numerical simulation, the minimum frequency error between the measured results and the theoretical results is at least up to 1% [21], to assess the effectiveness of the updated model; the convergence criterion was chosen as

$$W(\omega_{(n-1)}^i, \omega_n^i) = \left| \frac{\omega_n^i - \omega_{(n-1)}^i}{\omega_n^i} \right|, \quad (3)$$

where $\omega_{(n-1)}^i$ is the i th order frequency value derived from the $(n-1)$ th updating and ω_n^i is the i th order frequency value derived from the n th updating.

With $W(\omega_{(n-1)}^i, \omega_n^i)$ under the condition of $W(\omega_{(n-1)}^i, \omega_n^i) \leq 1\%$ (where i is the needed order of the frequency), the updating is stopped with the corresponding a_{rn} (where $r = 1, 2, \dots, p$) as the final updating results of the stiffness reduction factor. Otherwise, the $(n+1)$ th updating continues.

Theoretically, model updating approaches both in multisteps and in single step must meet the same convergence

criterion, which indicates that these two approaches can attain the same accuracy.

The finite element model updating flowchart of the spatial lattice structure in consideration of the semirigid characteristics of the bolt-ball joint is shown in Figure 4.

4. Finite Element Model Updating of Single-Layer Lattice Cylindrical Shell

4.1. Correlation Analysis of Dynamic Test. The experiment test model of the single-layer lattice cylindrical shell (the test shell) with a length of 21.0 m, a width of 3.0 m, and a vector height of 0.75 m is shown in Figure 5. The test shell was constructed with a bolt ball; the stiffness of the connection was enhanced by increasing the size of the bolt and sleeve. There were 4 kinds of tubes and corresponding bolts, as shown in Table 1.

The bolt ball was a BS180 type; the 2nd column space was selected as a typical one, considering a 7-column space and its similarity in the number and type of the tubes, and is shown in Figure 6. The experiment was done in an 8-seismic array, as shown in Figure 7, at Beijing University of Technology.

The BEAM44 of ANSYS was applied to the test shell. BEAM44 is a uniaxial element with tension, compression, torsion, and bending capabilities. The element has six degrees of freedom at each node: translations in the nodal x , y , and z directions and rotations about the nodal x -, y -, and z -axes. To guarantee the precision of modal calculation, each tube was divided into five elements.

According to the modal results obtained from numerical simulation, the measuring point layout priority comprehensive scheduling method was used for the arrangement of the sensors [7]. The sensors were just placed in the Y and Z directions while no sensor was placed in the third direction for the fact that, through modal theory analysis, the vibration in the third direction is weak, as shown in Figure 5. The sinusoidal excitation method was used in the dynamic test. The first four natural frequencies and the first three modal shapes were tested with two electromagnetic exciters with output of 50 N, two DF1010 ultra-low-frequency function generators, and two KD2701 power amplifiers over the length of the test model. The method of test data processing used in this paper can be seen in [7].

Usually during engineering design of single-layer reticulated shell model, the length of a tube is usually considered to be the distance from one bolt-ball center to another; the joint connection is assumed to be rigid, which is defined as the rigid model in this paper. The frequency rate ($ER(\omega_i^t, \omega_i^c)$) and modal assurance criterion ($MAC(\varphi_i^t, \varphi_i^c)$) were adopted to assess rationality of the rigid model with the following expressions:

$$ER(\omega_i^t, \omega_i^c) = \left| \frac{\omega_i^t - \omega_i^c}{\omega_i^t} \right|, \quad (4)$$

$$MAC(\varphi_i^t, \varphi_i^c) = \frac{|\varphi_i^{tT} \varphi_i^c|^2}{|\varphi_i^{tT} \varphi_i^t| |\varphi_i^{cT} \varphi_i^c|},$$

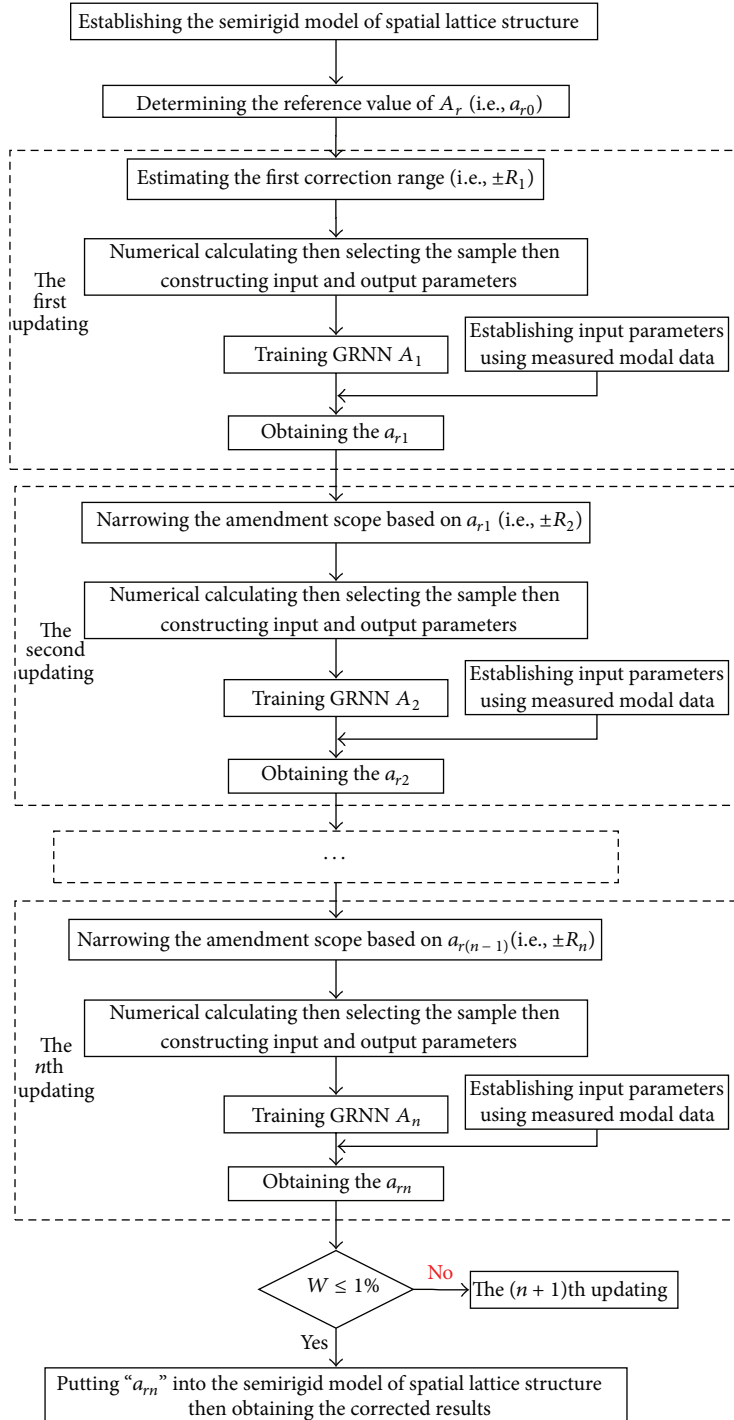


FIGURE 4: Flowchart of the finite element model fractional steps updating strategy.

TABLE 1: Tube types and specifications (mm).

Tubes numbering	1A	1B	1C	2A	3A	4A
Tubes types		Φ32 × 2.15	Φ48 × 3.5	Φ60 × 3.5	Φ89 × 3.75	
Bolts		M16	M24	M24	M27	

where ω_i^t ($i = 1, 2, \dots, n$) is the actual measured natural frequency, φ_i^t ($i = 1, 2, \dots, n$) is the measured modal shapes, ω_i^c ($i = 1, 2, \dots, n$) is the natural frequency obtained from the theoretical calculation, φ_i^c ($i = 1, 2, \dots, n$) is the modal shape obtained from the theoretical calculation, and T is the matrix transposition.

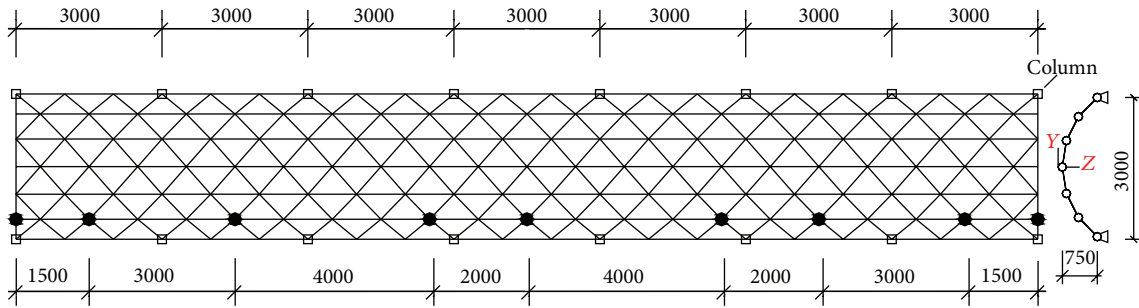


FIGURE 5: Test model of the reticulated shell (mm), with the measuring point arrangement (●), and the node numbering from left to right is 1, 25, 46, 60, 88, 109, 130, 151, and 11, respectively.

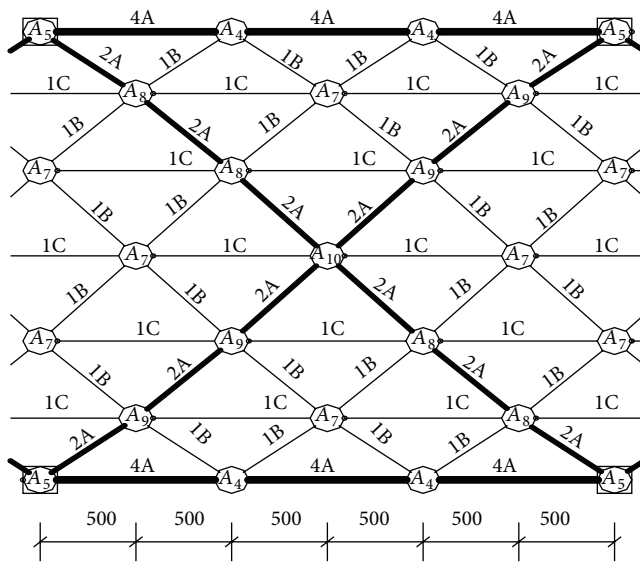


FIGURE 6: Structure's tubes.

TABLE 2: Comparison of the actual measured and rigid model results.

Modal	Measured values (Hz)	Rigid model (Hz)	ER (%)	MAC
1	6.62	7.86	18.81	0.77
2	8.40	9.79	16.58	0.69
3	10.1	13.18	30.50	0.51
4	13.89	16.63	19.73	—

The numerical model becomes more reliable as $ER(\omega_i^t, \omega_i^c)$ approaches 0 and $MAC(\varphi_i^t, \varphi_i^c)$ approaches 1 [20]. The minimum error of 16.58% (2nd order) can be seen in Table 2. The errors were induced by numerous factors, such as changes in support stiffness, and coordinate deviation of tubes and joints. However, ignoring the semirigid characteristic of bolt-ball joints is the main reason for the errors in the rigid model. Therefore, a fine numerical model was developed in this paper, by considering the semirigid characteristics of bolt-ball joints.

4.2. Corrected Parameters Determination. At present, many researches about spatial lattice structure have been reported. For example, by studying the welded spherical joints with beam element replacing nodes, Wang [22] concluded that good equivalent results were obtained when the ratio of the axial stiffness between tubes in the joint zone and the non-joint zone was within the range of 45% to 50%.

Much work has been done on the mechanical behavior of bolt-ball joints [23–26]. For example, the $M-\theta$ (bending moment and rotating angle) curve of bolt-ball joints was considered in an analysis of the seismic behavior of Kiewit-type single-layer reticulated shells with bolt-ball joints [23]. The seismic internal force coefficients of K8 and K6 single-layer spherical shells were proposed to be 1.80 and 1.44, respectively, which were bolt-ball joint stiffness reduction factors of 0.55 and 0.69 (i.e., reciprocals of 1.80 and 1.44), respectively.

Through an examination of the ultimate bearing capacities of bolt-ball joints (M20, M24, and M27) in K8 and K6 single-layer spherical shells, Fan et al. [26] concluded that the bolt-ball joint ultimate bearing capacity was approximately 0.4 to 0.8 times of that of a rigid joint.

In the literature [10, 22, 23, 26], the reference value of a_r was a_{r0} (where $r = 1, 2, 3, 4$), which was set to 0.5. In order to obtain a more realistic reduction factor for the test shell, the value of a_r was limited in the range of $[-60\%, 60\%]$, that is, in the range of $[0.2, 0.8]$. Literature [27] shows that the corrected precision requirement could be satisfied when the value of b_i ($i = 1, 2, \dots, n$) is 0.1.

There are numerous parameters in the finite element model of a spatial lattice structure, and the sensitivity of each parameter to the dynamic characteristics is different. Therefore, if all of the parameters are taken into account in the model updating process, huge amounts of calculations and computer time are required, making a very inefficient model, and the results diverge. Accordingly, the relatively sensitive parameters are always chosen as the variables of the model updating problem; the dynamic sensitivity analysis of the parameters is turned into an effective way to solve the above problem [28].

There were four types of joint connections in the test shell model (i.e., M16-32 \times 2.15, M24-48 \times 3.5, M24-60 \times 3.5, and M27-89 \times 3.75). To obtain their dynamic sensitivity,



FIGURE 7: Test model field: (a) single-layer latticed cylindrical shell; (b) electromagnetic exciter using a 50 N output.

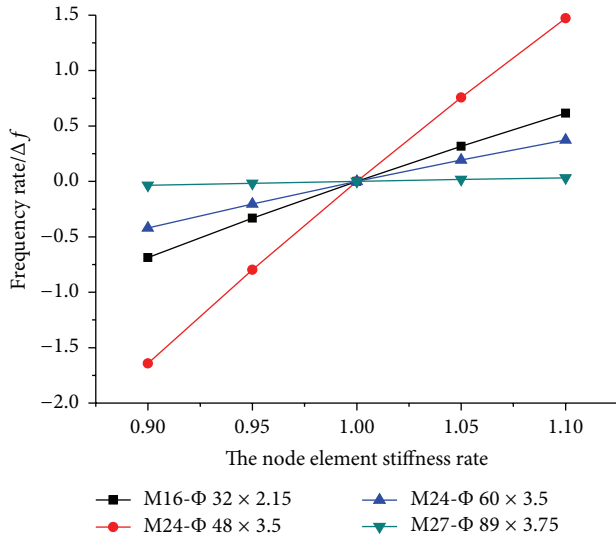


FIGURE 8: The influence of node element stiffness of connection in different types to the fundamental frequency.

frequency $f_{1,0}$ was derived from the joint element stiffness under a_{r_0} (where $r = 1, 2, 3, 4$) = 0.5, frequency f_s was derived from the joint element stiffness under $s \times a_{r_0}$ (s is magnification and equal to 0.9, 0.95, 1.05, 1.1), and the formula of frequency rate was $\Delta f = (f_s - f_{1,0})/f_{1,0}$. The calculated results are shown in Figure 8.

As shown in Figure 8, the joint element stiffness of M16-32 × 2.15, M24-48 × 3.5, and M24-60 × 3.5 makes a considerable impact on the fundamental frequency of the test model; however, the joint element stiffness of M27-Φ89 × 3.75 makes slight influence on it. The same law was evident for the frequency in the other orders. Therefore, the influence of M27-Φ89 × 3.75 was omitted in the updating process; that is, its joint element stiffness reduction factor was considered as 0.5.

In this paper, the bolt-ball joint element stiffness reduction factors of M16-Φ32 × 2.15, M24-Φ48 × 3.5, and M24-Φ60 × 3.5 were corrected by GRNN. It was assumed that

the same types of bolts had the same connection stiffness and that all connections were in sound condition; that is, the reference value of a_{r_0} ($r = 1, 2, 3$) was 0.5 and the optimized range was [0.2, 0.8].

4.3. Analysis of Corrected Results. According to Figure 4, the detailed procedures of fractional steps model updating were as follows:

- (1) For the first updating, the values of $a_{r_0} \times (1 - 0.6)EI_r$, $a_{r_0} \times 1.0EI_r$, and $a_{r_0} \times (1 + 0.6)EI_r$ ($r = 1, 2, 3$) were put into the semirigid model of the test shell. The modal calculation was carried out with $a_{10} = a_{20} = a_{30} = 0.5$, $b_1 = 0.6$, and $c_1 = 2$ and the allowable variation range for a_{r_0} was [-60%, 60%]. The CPFM (i.e., a 40×1 matrix) was derived from the first four natural frequencies and the first two modal shape components of the 18 sensors located on both y - and z -axes of the 9 positions (i.e., the solid black circles in Figure 5). Sample database A_1 for the relationship between the CPFM and the joint element stiffness reduction factor of the test shell was established.
- (2) Through the training of the GRNN with the CPFM, which was derived from the measured frequencies and modal shape components, with the input and the joint element stiffness reduction factors as the output, the joint element reduction factor of the test shell could be identified by the reverse neural network model. For further information and a complete formulation of GRNN as well as their detailed implementations steps, the reader is referred to a number of publications in the literature, such as [1, 15–18]. The initial correction results of the stiffness reduction factor were drawn ($a_{11} = 0.721$, $a_{12} = 0.573$, and $a_{13} = 0.201$).
- (2) Based on the results of the first updating, the results of the second updating were obtained ($a_{21} = 0.658$, $a_{22} = 0.563$, and $a_{23} = 0.214$) with $b_2 = 0.3$, $c_2 = 2$ and the allowable variation range of [-30%, 30%] (i.e., $R_1 = 0.3$).

TABLE 3: Results of updated frequency and $W(\omega_{(n-1)}^i, \omega_n^i)$; F_n^i is the i th order frequency under the n th updating.

Modal	F_1^i (Hz)	F_2^i (Hz)	F_3^i (Hz)	$W(\omega_1^i, \omega_2^i)$	$W(\omega_2^i, \omega_3^i)$
1	6.78	6.70	6.65	1.25%	0.75%
2	8.19	7.99	7.96	2.54%	0.42%
3	11.48	10.89	10.82	5.35%	0.66%
4	14.85	13.41	13.34	10.69%	0.54%

- (3) Based on the results of the second updating, the results of the third updating were obtained ($a_{31} = 0.606$, $a_{32} = 0.553$, and $a_{33} = 0.218$) with $b_3 = 0.1$, $c_3 = 2$ and the allowable variation range of $[-10\%, 10\%]$ (i.e., $R_2 = 0.1$).

The results of the updated frequency in the above steps and $W(\omega_{(n-1)}^i, \omega_n^i)$ are shown in Table 3. It is obvious that $W(\omega_2^i, \omega_3^i) < 1\%$ after the third updating, indicating that the results meet the convergence criterion after just 3 corrections. The results of the third updating and measured values are shown in Table 4, the comparison of frequency is shown in Figure 9, and the comparison of modal shapes is shown in Figure 10.

From Tables 3 and 4 and Figures 9 and 10, the following conclusions can be made:

- (1) The trend of the correction results after each updating showed that they subsequently became closer to the measured value. The frequency errors of any order were reduced greatly, and the corrected results of the first-order mode were in good agreement with the measured results, accurately reflecting the true value of the dynamic characteristics of the test model. The correction method proposed in this paper was shown to be reasonable and effective.
- (2) The characteristics of a huge structure and limited incentive energy in a spatial lattice structure led the lower order modes to be easily excited and the first-order mode to be a simple translation movement; therefore, the measured results were in good agreement with the corrected ones. The third-order mode was complex and local vibration modal shapes may have existed, leading to the nonideality of the measured results; therefore, the large error in the third-order mode was because the inaccurate measured results were not taking into account in the GRNN input parameters.
- (3) Although the error between the corrected and measured modes was greatly reduced, there were still some errors from other factors. For example, it was assumed that the geometry size and material properties of the tubes could be obtained accurately, and the stiffness correction of $M27-\Phi89 \times 3.75$, which had a low dynamic sensitivity, was not taken into account. GRNN may cause a little error when generalized with the experimental data. Moreover, the installation accuracy and testing environment during

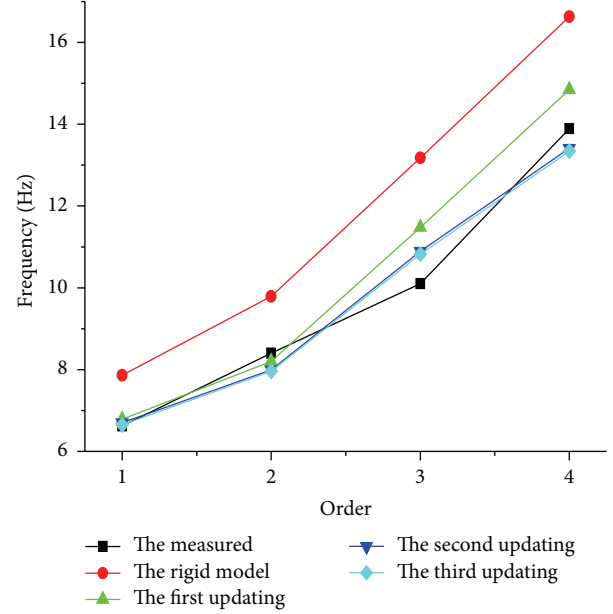


FIGURE 9: Comparison of frequency.

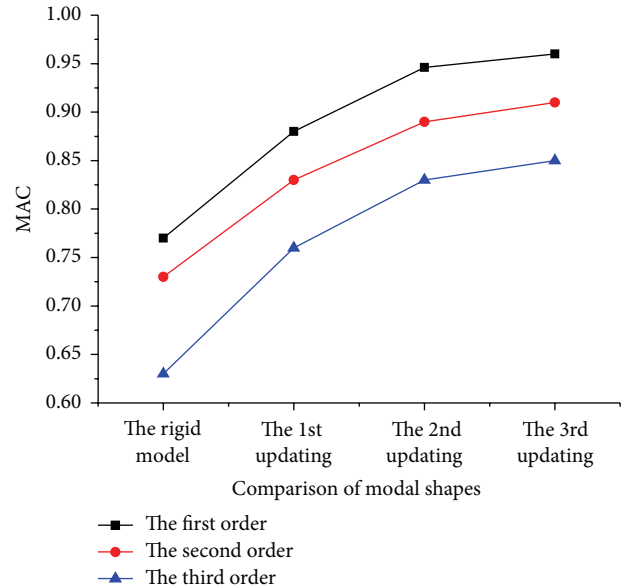


FIGURE 10: Comparison of modal shapes.

the test process could also have influenced the testing precision.

5. Conclusions

In this paper, the method that proposed the finite element model fractional steps updating strategy for a spatial lattice structure based on the GRNN authors has been proposed. It was applied to a test shell; the main conclusions are as follows:

- (1) A new algorithm, the finite element model fractional steps updating strategy for a spatial lattice structure based on the GRNN, was proven to be reasonable

TABLE 4: Results of model updating.

Modal	f (measured, Hz)	f (updated, Hz)	Correlation analysis		Modal shapes
			ER (%)	MAC	
1	6.62	6.65	0.45	0.96	Type I, the whole structure displays translational motion in the transverse direction.
2	8.40	7.96	5.23	0.91	Type II, the both ends of the structure display nonsymmetric motion in the longitudinal direction.
3	10.10	10.82	7.13	0.85	Type III, the middle of the structure displays offset to one side. The both ends of the structure display symmetric motion in the longitudinal direction.
4	13.89	13.34	3.96	—	—

and effective when applied to the test shell. Compared with the correction methods of the traditional matrixes and parametric types, the new algorithm has the advantages of definite physical meaning, low computational complexity, strong robustness, and high accuracy.

- (2) The new algorithm avoids the disadvantages of the GRNN, such as data explosion and decreased nonlinear mapping capacity. Therefore, it can be used easily and appropriately in model updating of a spatial lattice structure with the characteristics of multitudinous tubes and joints.
- (3) To address the limited number of measured points on actual structures in project monitoring, the CPMF derived from low-order modal data of the limited measurement information of the structure was adopted as the input parameter of the GRNN and applied to the test shell. It was proven to be reasonable and effective. Therefore, the new algorithm is suitable for the correction of incomplete modal data.
- (4) The method proposed in this paper is effective given the main effect factor (The semirigid characteristic of the bolt-ball joints) on the natural vibration characteristics. However, other effect factors, such as the elastic modulus of tubes and coordinate deviation of tubes and joints, also have some effect on it, so further studies considering more effect factors should be promoted.

Conflict of Interests

The authors declare that there is no conflict of interests regarding the publication of this paper.

Acknowledgment

This work is supported by the National Natural Science Foundation of China (Grant no. 51179081).

References

- [1] O. Hasançebi and T. Dumlupinar, "Linear and nonlinear model updating of reinforced concrete T-beam bridges using artificial neural networks," *Computers and Structures*, vol. 119, pp. 1–11, 2013.
- [2] D. Currie, N. Petrie, L. Mao, and Y. Lu, "A benchmark study of dynamic damage identification of plates," *Proceedings of the Institution of Civil Engineers: Engineering and Computational Mechanics*, vol. 165, no. 2, pp. 103–118, 2012.
- [3] V. Meruane and J. Mahu, "Real-time structural damage assessment using artificial neural networks and antiresonant frequencies," *Shock and Vibration*, vol. 2014, Article ID 653279, 14 pages, 2014.
- [4] D. H. Ding, *Finite Element Model Updating of Single Pylon Cable-Stayed Bridges*, Southwest Jiaotong University, Chengdu, China, 2012.
- [5] L. Li, H. P. Zhu, and K. Z. Hong, "Experimental study on damage detection of frame structured based on artificial neural network algorithm," *Journal of Vibration and Shock*, vol. 25, pp. 107–109, 2006 (Chinese).
- [6] H.-X. He, W.-M. Yan, and Z. Wang, "Stepwise model updating method based on substructures and GA-ANN," *Engineering Mechanics*, vol. 25, no. 4, pp. 99–105, 2008 (Chinese).
- [7] C. W. Liu, Y. G. Zhang, and J. Z. Wu, "Experimental study on damage location of single-layer latticed cylindrical shell based on the dynamic testing," *China Civil Engineering Journal*, vol. 47, no. 6, pp. 9–17, 2014.
- [8] Y. Liu, Z. D. Duan, and H. Liu, "Updating finite element model of structures with semi-rigid joints and boundary," in *Smart Structures and Materials 2006: Sensors and Smart Structures Technologies for Civil, Mechanical, and Aerospace Systems*, vol. 6174 of *Proceedings of SPIE*, pp. 61743L1–61743L13, 2006.
- [9] H. H. Ma, F. Fan, Z. G. Cao, M. Y. Cui, and S. Z. Shen, "Numerical simulation of semi-rigid joints in single-layer dome structures," *International Journal of Space Structures*, vol. 52, pp. 3–18, 2011.
- [10] Y. G. Zhang and Y. Z. Zhou, "Stiffness analysis and modeling simplification of the bolt-ball joints," in *Proceedings of the 12th National Symposium on Modern Structural Engineering*, Beijing, China, 2012.
- [11] N. de Alcantara, "Identification of steel bars immersed in reinforced concrete based on experimental results of eddy current testing and artificial neural network analysis," *Nondestructive Testing and Evaluation*, vol. 28, no. 1, pp. 58–71, 2013.
- [12] M. Y. Rafiq, G. Bugmann, and D. J. Easterbrook, "Neural network design for engineering applications," *Computers & Structures*, vol. 79, no. 17, pp. 1541–1552, 2001.

- [13] A. A. Javadi and M. Rezaia, "Applications of artificial intelligence and data mining techniques in soil modeling," *Geomechanics and Engineering*, vol. 1, no. 1, pp. 53–74, 2009.
- [14] D. F. Specht, "A general regression neural network," *IEEE Transactions on Neural Networks*, vol. 2, no. 6, pp. 568–576, 1991.
- [15] F. Doulati Ardejani, R. Rooki, B. Jodieri Shokri, T. Eslam Kish, A. Aryafar, and P. Tourani, "Prediction of rare earth elements in neutral alkaline mine drainage from Razi coal mine, Golestan Province, northeast Iran, using general regression neural network," *Journal of Environmental Engineering*, vol. 139, no. 6, pp. 896–907, 2013.
- [16] F. Han, D. W. Zhong, and J. Wang, "Model updating based on radial basis function neural network," *Journal of Wuhan University of Science and Technology*, vol. 34, pp. 115–118, 2011 (Chinese).
- [17] S.-F. Jiang, C.-M. Zhang, and J. Yao, "Eigen-level data fusion model by integrating rough set and probabilistic neural network for structural damage detection," *Advances in Structural Engineering*, vol. 14, no. 2, pp. 333–350, 2011.
- [18] S. Heddami, A. Bermad, and N. Dechemi, "Applications of radial-basis function and generalized regression neural networks for modeling of coagulant dosage in a drinking water-treatment plant: comparative study," *Journal of Environmental Engineering*, vol. 137, pp. 1209–1214, 2011.
- [19] H. F. Lam, J. M. Ko, and C. W. Wong, "Localization of damaged structural connections based on experimental modal and sensitivity analysis," *Journal of Sound and Vibration*, vol. 210, no. 1, pp. 91–114, 1998.
- [20] Y. G. Zhang, C. W. Liu, and J. Z. Wu, "The application of the three-step location approach in damage identification of the spatial lattice structure," *Disaster Advances*, vol. 6, supplement 3, pp. 74–80, 2013.
- [21] Y.-G. Zhang, C.-W. Liu, J.-Z. Wu, and T.-M. Peng, "Improved power spectrum peak method applied in the modal identification of spatial lattice structures," *Journal of Vibration and Shock*, vol. 32, no. 9, pp. 10–39, 2013 (Chinese).
- [22] N. Wang, *Study on fine model of single-layer cylindrical reticulated shell considering joint stiffness under strong earthquake* [Ph.D. dissertation], Beijing University of Technology, 2013.
- [23] F. Fan, M.-L. Wang, Z.-G. Cao, and S.-Z. Shen, "Seismic analysis of single-layer spherical reticulated shells with semi-rigid joint," *Journal of Harbin Institute of Technology*, vol. 41, no. 10, pp. 14–19, 2009 (Chinese).
- [24] A. López, I. Puente, and M. A. Serna, "Numerical model and experimental tests on single-layer latticed domes with semi-rigid joints," *Computers and Structures*, vol. 85, no. 7-8, pp. 360–374, 2007.
- [25] H. H. Ma, F. Fan, and S. Z. Shen, "Numerical parametric investigation of single-layer latticed domes with semirigid joints," *International Journal of Space Structures*, vol. 49, no. 158, pp. 99–110, 2008.
- [26] F. Fan, H.-H. Ma, Z.-G. Cao, and S.-Z. Shen, "Direct estimation of critical load for single-layer reticulated domes with semi-rigid joints," *International Journal of Space Structures*, vol. 25, no. 1, pp. 15–24, 2010.
- [27] Q. Xue, J. P. Hao, and Y. Zheng, "Research on steel frame parameters identification based on RBF neural networks," *Journal of Xi'an University of Architecture and Technology (Natural Science Edition)*, vol. 43, pp. 192–197, 2011 (Chinese).
- [28] D. Wang and Y.-Z. Zhu, "Mechanical characteristics analysis of sensitive parameters of long-span steel truss suspension bridge," *Advanced Materials Research*, vol. 250–253, pp. 3381–3386, 2011.

Research Article

Planetary Gearbox Fault Diagnosis Using Envelope Manifold Demodulation

Weigang Wen,^{1,2} Robert X. Gao,^{2,3} and Weidong Cheng¹

¹*School of Mechanical, Electronic and Control Engineering, Beijing Jiaotong University, Beijing 100044, China*

²*Department of Mechanical Engineering, University of Connecticut, Storrs, CT 06269, USA*

³*Mechanical and Aerospace Engineering Department, Case Western Reserve University, Cleveland, OH 44106, USA*

Correspondence should be addressed to Weigang Wen; wgwen@bjtu.edu.cn

Received 4 July 2015; Revised 16 September 2015; Accepted 27 September 2015

Academic Editor: José V. Araújo dos Santos

Copyright © 2016 Weigang Wen et al. This is an open access article distributed under the Creative Commons Attribution License, which permits unrestricted use, distribution, and reproduction in any medium, provided the original work is properly cited.

The important issue in planetary gear fault diagnosis is to extract the dependable fault characteristics from the noisy vibration signal of planetary gearbox. To address this critical problem, an envelope manifold demodulation method is proposed for planetary gear fault detection in the paper. This method combines complex wavelet, manifold learning, and frequency spectrogram to implement planetary gear fault characteristic extraction. The vibration signal of planetary gear is demodulated by wavelet enveloping. The envelope energy is adopted as an indicator to select meshing frequency band. Manifold learning is utilized to reduce the effect of noise within meshing frequency band. The fault characteristic frequency of the planetary gear is shown by spectrogram. The planetary gearbox model and test rig are established and experiments with planet gear faults are conducted for verification. All results of experiment analysis demonstrate its effectiveness and reliability.

1. Introduction

Planetary gear systems are widely used in industrial machinery because they have advantages of large transmission ratios, strong load-bearing capacity, and high transmission efficiency [1]. In practical industrial fields, the planetary gear system whose structure is more complicated than fixed-shaft gearbox is subject to be damaged under heavy load and tough working conditions. Accurate fault detection of planetary gearbox is important to reduce unscheduled machine downtime and avoid catastrophic accidents [2]. Vibration signal analysis which was used extensively in various machine condition monitoring techniques has become one of the most important methods applied for planetary gearbox fault diagnostics.

The planetary gear system is composed of sun gear, planet gears, ring gear, planet carrier, shaft, and bearings. Usually, the ring gear is stationary, the sun gear rotates around its own center, and the planet carrier rotates under very low speeds because of the large transmission ratio. Multiple planet

gears, which mesh simultaneously with the sun gear and ring gear, not only rotate around their own center but also revolve around the center of the sun gear [3]. Such behaviors cause the vibration signals of the planetary gearbox with different meshing phases and varied propagation paths [4]. The unique behavior mode of planetary gearbox presents a challenge to fault diagnosis of planetary gear system. Studies on the fault diagnosis of planetary gearboxes are gaining more attention of the researchers [5].

The fault diagnosis of planetary gearboxes comes from various methodologies. Modeling methods are useful in condition monitoring. Tooth pitting and crack on the sun gear of planetary gearboxes were modeled and the influence of faults on the gear mesh stiffness was analyzed in [6]. An approach based on physical models to detect damage of a planetary gearbox in a helicopter transmission system was proposed in [7]. The spectral structure of vibration signal of planetary gearbox in different health conditions was investigated and vibration signal models of gear damage were proposed in [8]. But the most popular fault diagnosis of

planetary gearbox is signal processing methods, for example, time-domain methods, frequency-domain methods, time-frequency-domain methods, and other signal processing methods. Time-domain signal processing methods, such as statistical indicators and time synchronous averaging, are relatively easy and direct compared to other methods. A technique for estimating the time-domain average of the tooth meshing vibration of individual planet gears and of the sun gear was demonstrated in [9]. Two special diagnostic parameters in time-domain for detecting faults of planetary gearbox were studied in [10]. In frequency-domain, the Fourier series of the vibration data from a planetary gearbox was explored and the source of the asymmetry phenomena in the frequency spectra was analyzed in [1]. The additional sidebands in frequency spectra produced by planet carrier torque modulations masking potentially the sidebands of fault in planetary gearboxes were investigated and a frequency-domain method to eliminate the effects of structural-path-caused amplitude changes was presented in [11]. The time-frequency-domain methods, such as Wigner-Ville distribution and wavelets, are developed to diagnose planetary gearboxes. The Wigner-Ville distribution of the simulated signals of fault modes in planetary gearboxes was studied in [12]. A method based on adaptive Morlet wavelets and singular value decomposition was applied to extract impulse features of a planetary gearbox in [13]. Reference [14] illustrated the spectral kurtosis for detecting a tooth crack on the ring in the planetary gearbox of a wind turbine. The cyclostationary properties of planetary gearbox vibration signals were investigated and a fault diagnosis based on spectral coherence map was developed in [15]. These literatures demonstrated the different effects of signal processing methods. The time-domain and frequency-domain methods just depict one aspect of the signal. The characteristic in time-domain and frequency-domain cannot be drawn simultaneously. Time-frequency-domain methods are generally much more effective than the other two. But it is better to combine them with other methods to implement demodulating and denoising.

The vibration signals of mechanical systems, especially for ones with fault, often show mutation, nonlinearity, and non-stationarity [16]. With the development of nonlinear dynamic theories, a number of nonlinear parameters and methods have been applied to machine condition monitoring and fault diagnosis [17–19]. Manifold learning especially is adopted to implement nonlinear dimensionality reduction for revealing the nonlinear intrinsic characteristics of vibration signal. The signal processing technique and manifold learning method are combined to strengthen the fault features of the rotating machine and reduce the impact of noise [20]. The manifold learning algorithm on the time-frequency distributions or the time-scale distributions generated manifold signature of fault to enhance nonlinear fault-induced components and suppress in-band noise in [21–23].

In planetary gearbox, the vibration signals from multiple planet gears may couple with each other leading the faulty components to be neutralized and cancelled [24]. Especially in practical industrial applications, the vibration signal is contaminated by background noise. Here, in order to extract

the fault feature of planetary gear from the noisy vibration signal, the methodology implementing decoupling, demodulating, and denoising is investigated. Because of the demodulation capability of wavelet envelope and the denoising ability of manifold learning [20, 25], these methods are integrated to achieve demodulating and denoising of the planetary gear vibration signal simultaneously in this paper.

The rest of the paper is organized as follows. In the second section, the wavelet envelope manifold demodulation method is introduced for fault diagnosis of planetary gearbox. Then in the third section, the vibration models and simulation experiments of the planetary gearbox in faulty condition are studied. In the fourth section, the practical vibration signals from planetary gearbox rig are analyzed to testify the effectiveness of the proposed method. The conclusions are finally presented in the fifth section.

2. Principle and Methodology

2.1. Framework of Methodology. In fault diagnosis of planetary gears, the accelerometers are fixed on the gearbox casing to collect vibration signals. The relative locations of sun-planet and planet-ring meshing with respect to the accelerometers are time-varying, which result in amplitude modulation (AM) effect on the meshing vibration signal. Time variation of meshing stiffness or the errors of the planetary gear also causes frequency modulation (FM) of the meshing vibration signal. The gear damage generates both AM and FM of the meshing vibration signal. These effects increase the complexity of the signal. Furthermore, there exists the random background noise in every frequency band for practical fault diagnosis of planetary gear in industrial fields. The noise can blight the signal at meshing frequency. So, extracting the meshing signal, reducing the noise effect in meshing frequency band, and demodulating the meshing vibration signal are the critical issues for fault diagnosis of planetary gearbox.

The enveloping analysis of resonance is a powerful tool to achieve demodulation of the signal of rotating machine. In the traditional way, a filter with resonance frequency and specific pass band is utilized to preprocess the vibration signal, and then the envelope of the resonance is drawn out by Hilbert transform. Here, a synthetic methodology that combines the complex wavelet transform, manifold learning method, and spectral analysis is proposed to demodulate and denoise the meshing vibration signal of planetary gears. The methodology is shown in Figure 1. At first, the continuous wavelet transform (CWT) with complex Morlet wavelet base is utilized to demodulate the vibration signal over scales to obtain the wavelet envelopes. Then, the meshing vibration sensitive indicator is built to select the specific scale band which corresponds to meshing frequency band. The first two steps both extract the envelope and filter out the noise not within the meshing frequency band. Thirdly, the manifold learning algorithm is introduced to extract the envelope manifold from the wavelet envelopes at the selected scales to reduce the in-band noise effect and reveal the envelope structure of the meshing vibration signal. Finally, the fault

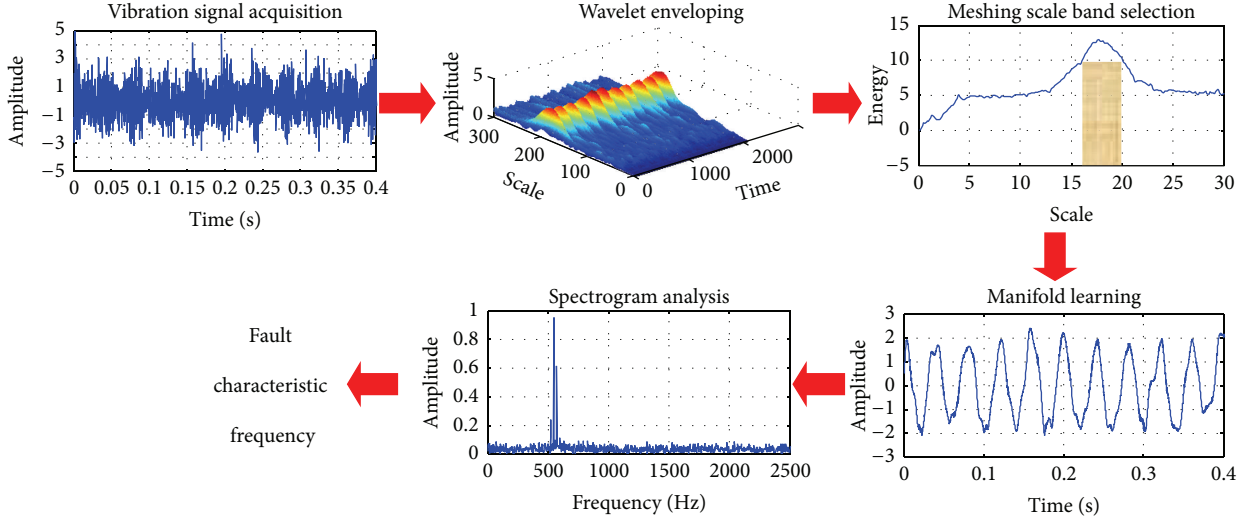


FIGURE 1: The process diagram of the methodology.

characteristic frequency is discovered by frequency spectrogram analysis.

2.2. Complex Wavelet Enveloping. It is well known that the wavelet transform can decompose a signal onto a time-scale plane [25]. The wavelet transform of a signal is equal to a set of band-pass filters with certain frequencies relevant to the scales. Continuous wavelet transform (CWT) is defined as the convolution of signal $x(t)$ with the complex conjugate of a set of wavelets. Here, complex wavelet $\varphi(t)$ is applied. The complex wavelet has the analytic property. It is defined as

$$\varphi(t) = \varphi_R(t) + j\varphi_I(t) = \varphi_R(t) + j\mathcal{H}[\varphi_R(t)], \quad (1)$$

where $\varphi_R(t)$ and $\varphi_I(t)$ represent the real and imaginary parts of the complex wavelet and $\mathcal{H}[\]$ is the Hilbert transform. Usually, the complex Morlet wavelet is used as the base wavelet for the vibration signal of rotating machine. The complex Morlet wavelet is defined as

$$\varphi(t) = \frac{1}{\sqrt{\pi f_b}} e^{-t^2/f_b} e^{j2\pi f_c t}, \quad (2)$$

where f_b is the bandwidth parameter and f_c is the wavelet center frequency. Here, the parameter optimization of the Morlet wavelet is not the research focus of this paper. The parameters are set as $f_b = 1$ and $f_c = 2$ by which the satisfied results can be achieved. The base wavelet with specific scale s is used to extract the component of frequency f in the signal. The relationship can be written as

$$f = \frac{f_c}{s\Delta}, \quad (3)$$

where Δ is the sampling period. From formula (3), the meshing frequency of the planetary gears can be estimated according to the special indicator at the scale. The wavelet

transform of the signal based on complex wavelet can be written as

$$\begin{aligned} W_C(s, \tau) &= W_R(s, \tau) + jW_I(s, \tau) \\ &= W_R(s, \tau) + j\mathcal{H}[W_R(s, \tau)]. \end{aligned} \quad (4)$$

According to the property of Hilbert transform, the envelope of signal at scale s can be computed from the modulus of the wavelet coefficients as

$$E_W(s, \tau) = \|W_C(s, \tau)\| = \sqrt{W_R^2(s, \tau) + W_I^2(s, \tau)}. \quad (5)$$

Through complex wavelet transformation and scale band selection, the band-pass filtering and enveloping can be achieved simultaneously.

2.3. Meshing Scale Band Selection. In the enveloping technique for fault diagnosis of rotating machine, the critical issue is to estimate the resonance frequency of the structure. In current literatures different indicators have been applied for decision of resonance modes. The spectral kurtosis (SK) is an effective measure to estimate the resonance frequency of impulsive components in vibration signal [26–29]. The smoothness index (SI) defined as the ratio of the arithmetic mean to the geometric mean is also utilized to measure the impulsiveness of the power spectrum of wavelet coefficient at each scale in [30]. After complex wavelet filtering and enveloping, the energy of vibration signal envelope concentrated within meshing frequency band more than the other band. The mean envelope energy can be adopted as the indicator for selection of meshing scale band. For the wavelet envelope of the signal $x(t)$, the mean energy (ME) of wavelet envelope at scale s is defined as

$$\text{ME}(s) = \frac{\sum_{\tau} E_W(s, \tau) E_W^*(s, \tau)}{N}, \quad (6)$$

where $E_W^*(s, \tau)$ is the complex conjugate of $E_W(s, \tau)$ and N is number of sample points. When the ME, SK, and SI in

frequency-domain are considered as indicators for selecting the appropriate scale for the meshing frequency in the data simulations and practical experiments, it is revealed that the ME is most suitable to select scale corresponding to the meshing frequency.

The scale corresponding to the global maximum of the indicator is defined as central scale s_C , which is utilized to evaluate the planetary gear meshing central frequency. The wavelet envelopes in meshing scale band, which construct a high-dimensional data space, contain the fault information in the meshing frequency band. The meshing scale band can be divided by the left limit s_L and right limit s_R around the central scale s_C . The left limit s_L and right limit s_R can be determined by the indicator value reducing to $1/\sqrt{2}$ of the maximum value of the indicator at the central scale s_C . So the scale band for the meshing frequency band can be defined as $s_B = [s_L, \dots, s_C, \dots, s_R]$.

The fault-induced impacts modulating the meshing frequency form the manifold structure embedded in the wavelet envelopes at this scale band. There is also another background noise within meshing frequency band. The in-band noise will corrupt the embedded manifold structure. Here, manifold learning is applied to retain the envelope manifold of the fault impacts while leaving out the in-band noise. And the n -dimension ($n = R - L + 1$, where R is the index of s_R and L is the index of s_L) data space can be reduced to m -dimension ($m \ll n$) by mean of the nonlinear dimensionality reduction for posttreatment.

2.4. Manifold Learning. There are several algorithms of manifold learning. The techniques of Isomap and locally linear embedding (LLE) were firstly proposed. Isomap is a global method because its embedding is based upon the geodesic distances between all pairs of points, while LLE is a local method because its embedding is based upon the relationship of each data point to its neighboring points [31, 32]. Laplacian eigenmap, Hessian eigenmap, local tangent alignment, diffusion map, and several other techniques were introduced.

A local approach is computationally more efficient than a global approach because the former involves sparse matrices and is more generally applicable to different types of manifolds. Laplacian eigenmap, which is a typical local approach, is applied to extract the manifold structure from the wavelet envelopes at planetary gear meshing frequency band because of its efficiency and robustness to the noise [33].

The methodology of Laplacian eigenmap algorithm consists of three steps: (1) construct K nearest neighbor graph on the set of sample points; (2) approximate the local manifold geometry within the neighborhood of each sample point; (3) minimize a global error function to obtain the global embedding [34].

Here, the number of nearest neighbor is set as $K = 40$, the reduced dimension is set as $m = 2$, and the first dimension data are taken as the signal for the next step of frequency spectrogram analysis for fault characteristic frequency extraction because of its minimum reconstruction error.

3. Simulated Signal Analysis

3.1. Simulation of Faulty Planet Gear. The planet gears mesh with ring gear and sun gear simultaneously. When there are faults on a planet gear, the meshing location of the faulty tooth and mating gear changes with the planet carrier rotation. Thus this changes the transfer path of the vibration signal of faulty tooth to the sensor and generates an extra AM effect on the meshing vibration signal. The meshing vibration amplitudes sampled by the sensor are modulated by the faulty tooth and the varied propagations synchronously [8]. Here, the faulty planet gear is analyzed. The faulty planet gear vibration signal can be written as

$$\begin{aligned} x(t) = & [1 - C \cos(2\pi f_{\text{carrier}} t)] \\ & \cdot [1 + A \cos(2\pi f_{\text{planet}} t + \theta)] \\ & \cdot \cos[2\pi f_{\text{mesh}} t + B \sin(2\pi f_{\text{planet}} t + \varphi) + \theta], \end{aligned} \quad (7)$$

where $x(t)$ is vibration signal in time-domain, f_{carrier} is planet carrier rotation frequency which represents propagation modulation, f_{planet} is planet gear rotation frequency which represents faulty planet gear modulation, f_{mesh} is meshing frequency, and θ , φ , and θ are the initial phases of AM, FM, and meshing, respectively. A , B , and C are the modulation amplitudes. After amplitude demodulation, the envelope of the meshing vibration signal is

$$\begin{aligned} y(t) = & 1 - C \cos(2\pi f_{\text{carrier}} t) + A \cos(2\pi f_{\text{planet}} t + \theta) \\ & + \frac{1}{2} AC \cos[2\pi (f_{\text{planet}} + f_{\text{carrier}}) t + \theta] \\ & + \frac{1}{2} AC \cos[2\pi (f_{\text{planet}} - f_{\text{carrier}}) t + \theta]. \end{aligned} \quad (8)$$

So the envelope amplitude spectrum is

$$\begin{aligned} Y(f) = & \delta(f) + C\delta(f - f_{\text{carrier}}) + A\delta(f - f_{\text{planet}}) \\ & + \frac{1}{2} AC\delta[f - (f_{\text{planet}} + f_{\text{carrier}})] \\ & + \frac{1}{2} AC\delta[f - (f_{\text{planet}} - f_{\text{carrier}})]. \end{aligned} \quad (9)$$

The simulation parameters of the planetary gearbox are shown in Table 1. For comparison, the time-domain diagram and frequency spectrogram are adopted to analyze the vibration signals at first. Then the envelope manifold demodulation is utilized to illustrate the advantage of this method.

The simulated vibration signal in time-domain is shown in Figure 2(a). The frequency spectrogram of the signal is shown in Figure 2(b). The meshing frequency of 437.5 Hz and the sideband can be seen in the spectrogram. It is not very clear to identify the planet carrier rotation frequency and the planet gear rotation frequency.

In envelope manifold demodulation, a series of scales of wavelet ranging from 1 to 30 are chosen to cover the meshing frequency of all the planetary gears. An increment of 0.1

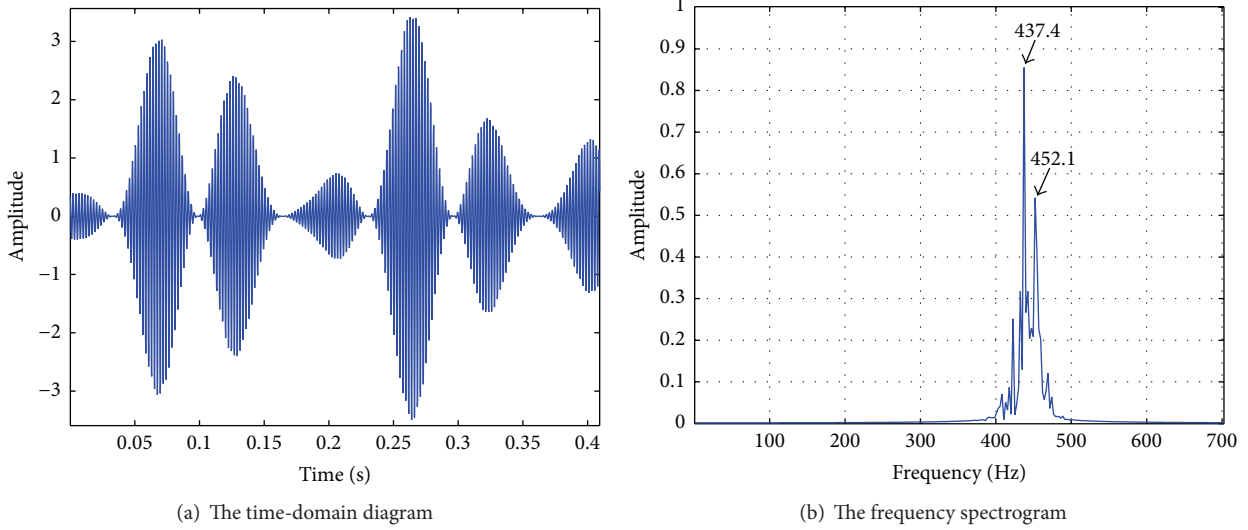


FIGURE 2: The time-domain diagram and frequency spectrogram of simulated signal.

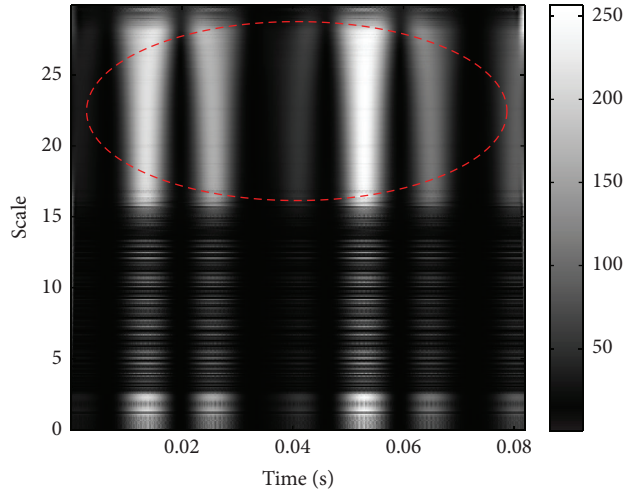


FIGURE 3: The wavelet envelope of simulated signal.

TABLE 1: The simulation parameters of faulty planet gear.

Parameters	Values
AM magnitude A	1
AM magnitude C	0.8
FM magnitude B	0.5
Meshing frequency (Hz)	437.5
Planet carrier rotation frequency (Hz)	5.468
Planet gear rotation frequency (Hz)	15.191

for scale is employed in the data experiments. The wavelet envelopes are shown in Figure 3. The lighter color in the graph illustrates greater wavelet envelopes. So the area circled by the ellipse corresponds to the greatest wavelet envelopes. The meshing frequency computed by formula (3) is the central frequency of the circled area.

The mean energy (ME), smoothness index (SI), and spectral kurtosis (SK) of wavelet envelope are utilized to choose the proper indicator of meshing frequency for comparison. The ME, SI, and SK as indicators are shown in Figures 4(a), 4(b), and 4(c). The central scale, respectively, is 22.8, 22.2, and 29.0 according to the ME, SI, and SK. The corresponding frequency, respectively, is 438.5 Hz, 450.5 Hz, and 344.8 Hz. The result from ME is closest to the meshing frequency band which is circled by the ellipse in Figure 3. The indicator ME is most accurate for selection of meshing frequency band.

The wavelet envelope at the central scale is shown in Figure 5(a) and the power spectrum of the wavelet envelope is shown in Figure 5(b). The characteristic frequencies of the power spectrum are 4.89 Hz, 9.78 Hz, 14.66 Hz, and 19.55 Hz corresponding to $f_{carrier}$, $f_{planet} - f_{carrier}$, f_{planet} , and $f_{planet} + f_{carrier}$. The characteristic frequency of faulty planet gear can be seen clearly on the spectrogram of the wavelet envelope because there is no in-band noise interference.

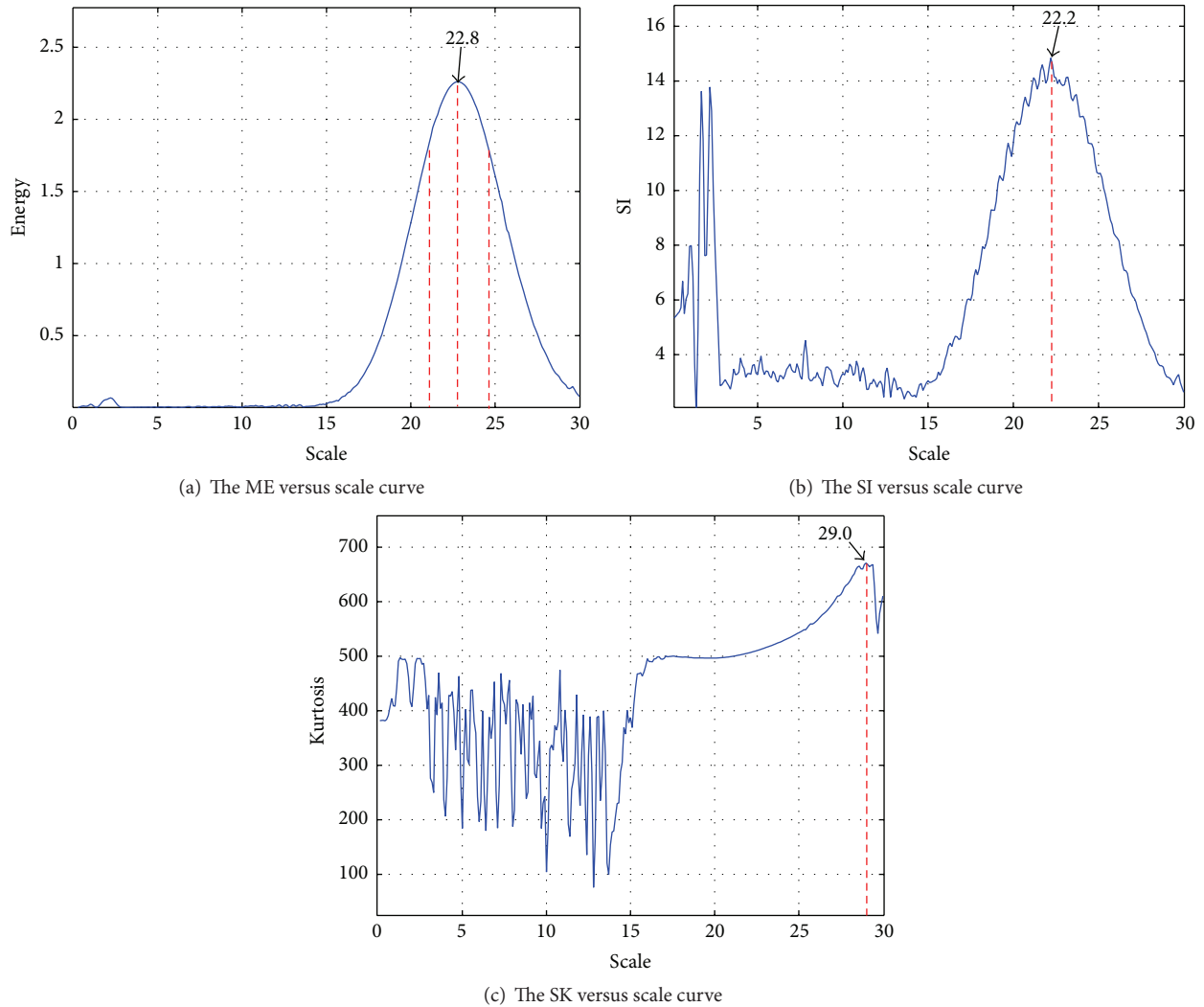


FIGURE 4: The indicators versus scale curve of simulated signal.

The wavelet envelope is proved to be adept at demodulation of planetary gear vibration signal.

3.2. Simulation of Contaminated Signal. In order to simulate the contamination of the in-band noise, the random background noise is added to the simulated signal of the faulty planet gear model to generate the contaminated signal up to SNR = -10 dB. Meanwhile, the meshing frequency is switched from 437.5 Hz to 492.0 Hz to testify the accuracy of selection of meshing frequency by ME.

For comparison, the amplitude demodulation methods based on empirical mode decomposition (EMD) and Hilbert transform are used to reveal the characteristic frequency of the planetary gears at first. It is well known that these methods are capable of demodulating the signal when it is not contaminated seriously by noise [35, 36]. But when random background noise is added to the signal, the demodulation ability of these methods diminishes dramatically. When the signal is contaminated by noise with SNR = -6 dB, the EMD

analysis results are shown in Figures 6(a) and 6(b). The fault characteristic frequency is not very clear in the spectrogram.

When the signal is contaminated by noise with SNR = -8 dB, the envelope and the frequency spectrogram of Hilbert transform after filtering are shown in Figures 7(a) and 7(b). The fault characteristic frequency cannot be seen in the envelope spectrum.

In these methods, the EMD can be seen as a process of band filter, and the band-pass filter is applied prior to the Hilbert transform. The noise out of meshing frequency band is filtered out. But the in-band noise distorts the original vibration signal causing the invisibility of faulty characteristic frequency.

When the signal is contaminated by noise with SNR = -10 dB, the wavelet envelopes can be shown in Figure 8(a). There is so much noise pollution that the original signal cannot be recognized. The ME as indicator is shown in Figure 8(b). The central scale 20.3 according to the ME is the central frequency of 492.6 Hz. The results show that the indicator of ME is accurate and robust to the noise

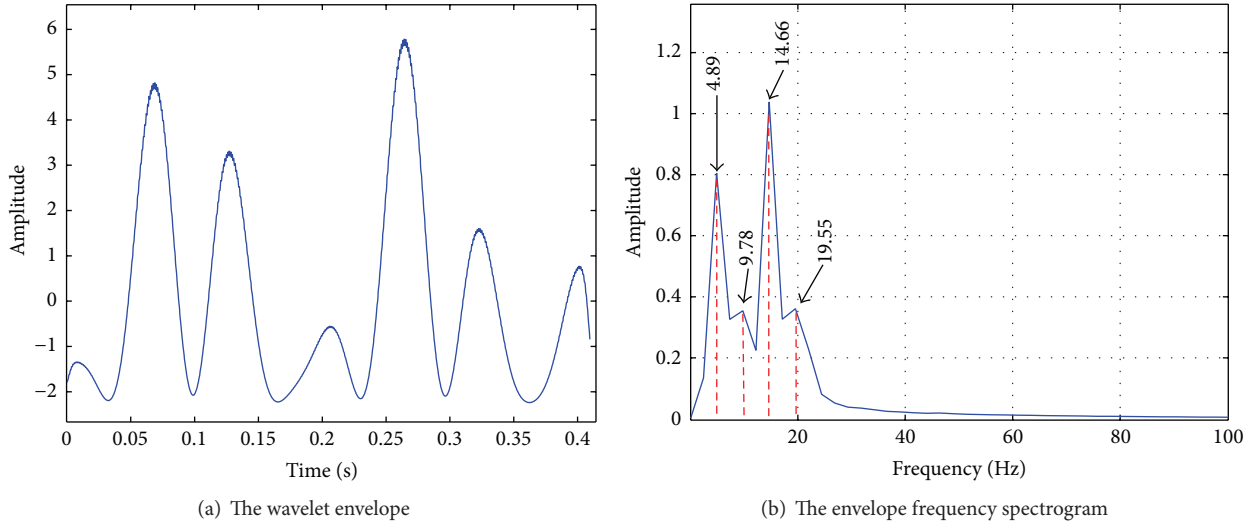


FIGURE 5: The wavelet envelope and spectrogram at the central scale of simulated signal.

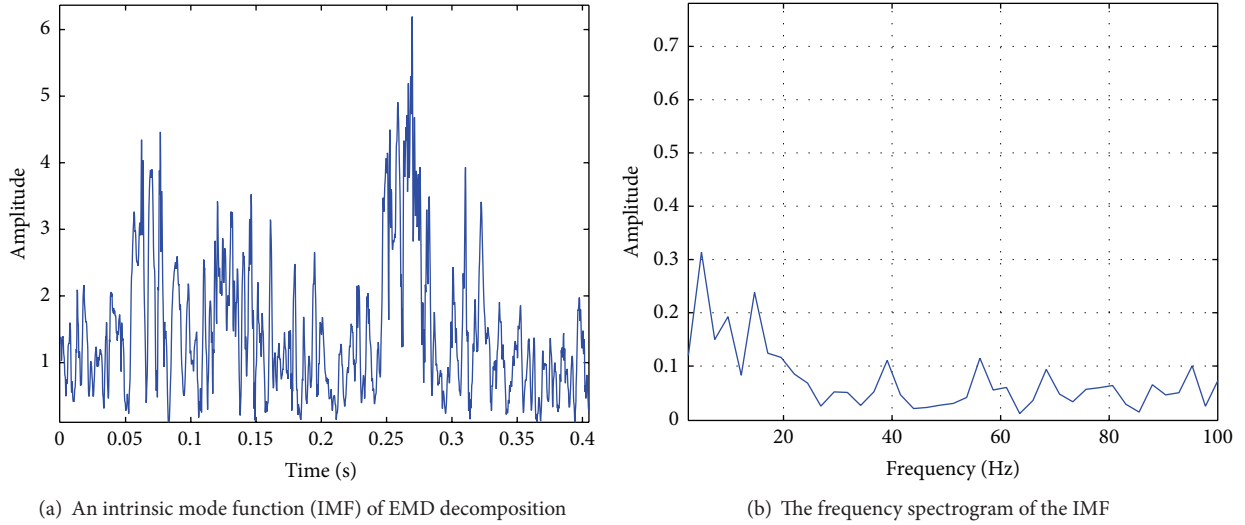


FIGURE 6: The EMD analysis result of contaminated signal with SNR = -6 dB.

up to SNR = -10 dB. After manifold learning, the wavelet envelope and the power spectrum are shown in Figures 8(c) and 8(d). All the characteristic frequencies can be seen in the envelope manifold spectrogram. These data experiments fully demonstrate the superiority of the envelope manifold demodulation method.

4. Experimental Signal Analysis

4.1. Experiment Design. In this section, the cases of practical experiments are studied to verify the effectiveness of the envelope manifold demodulation methodology. The planetary gearbox test rig is shown in Figure 9. The planetary gear set in the gearbox is shown in Figure 10. The motor drives the input shaft of planetary gearbox through coupler. The input shaft is coupled to the sun gear, the ring gear is standstill, and the planet carrier is coupled to the output shaft which

TABLE 2: The planetary gearbox parameters.

Parameters	Values
Planet gear teeth	36
Sun gear teeth	28
Ring gear teeth	100
Number of planet gears	3

drives the other load gearboxes and load motor. The rotation speed of the planetary gearbox input shaft is measured by the tachometer. The vibration signals are collected by the accelerometer mounted on the planetary gearbox. The experimental planet gears are shown in Figure 11. The parameters of planetary gearbox are listed in Table 2.

Three experiments are designed for comparison. The first case is the experiment of the normal planet gear, the second

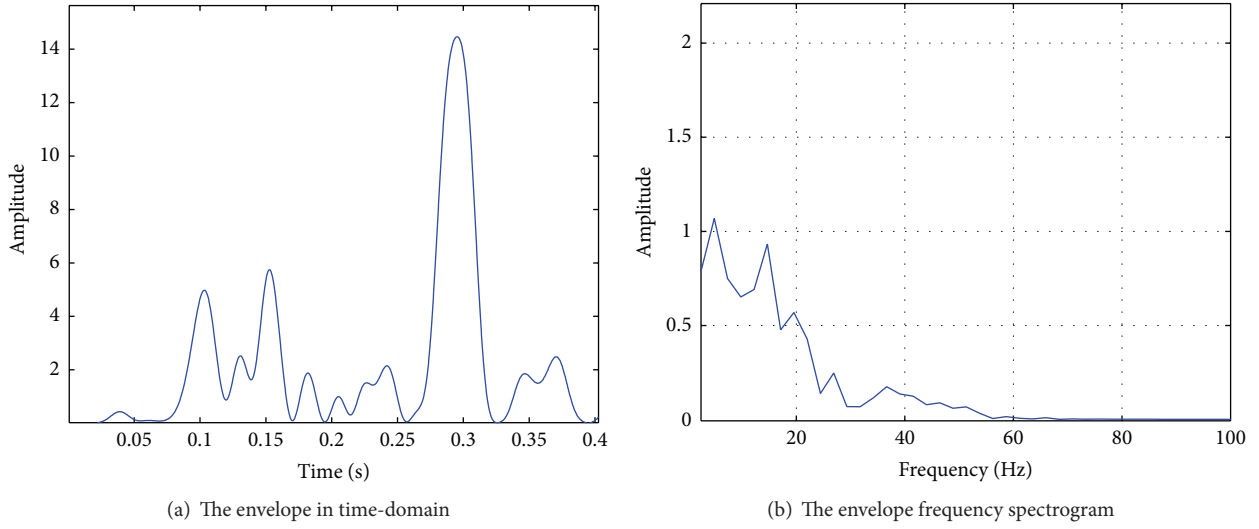


FIGURE 7: The Hilbert analysis result of contaminated signal with SNR = -8 dB.

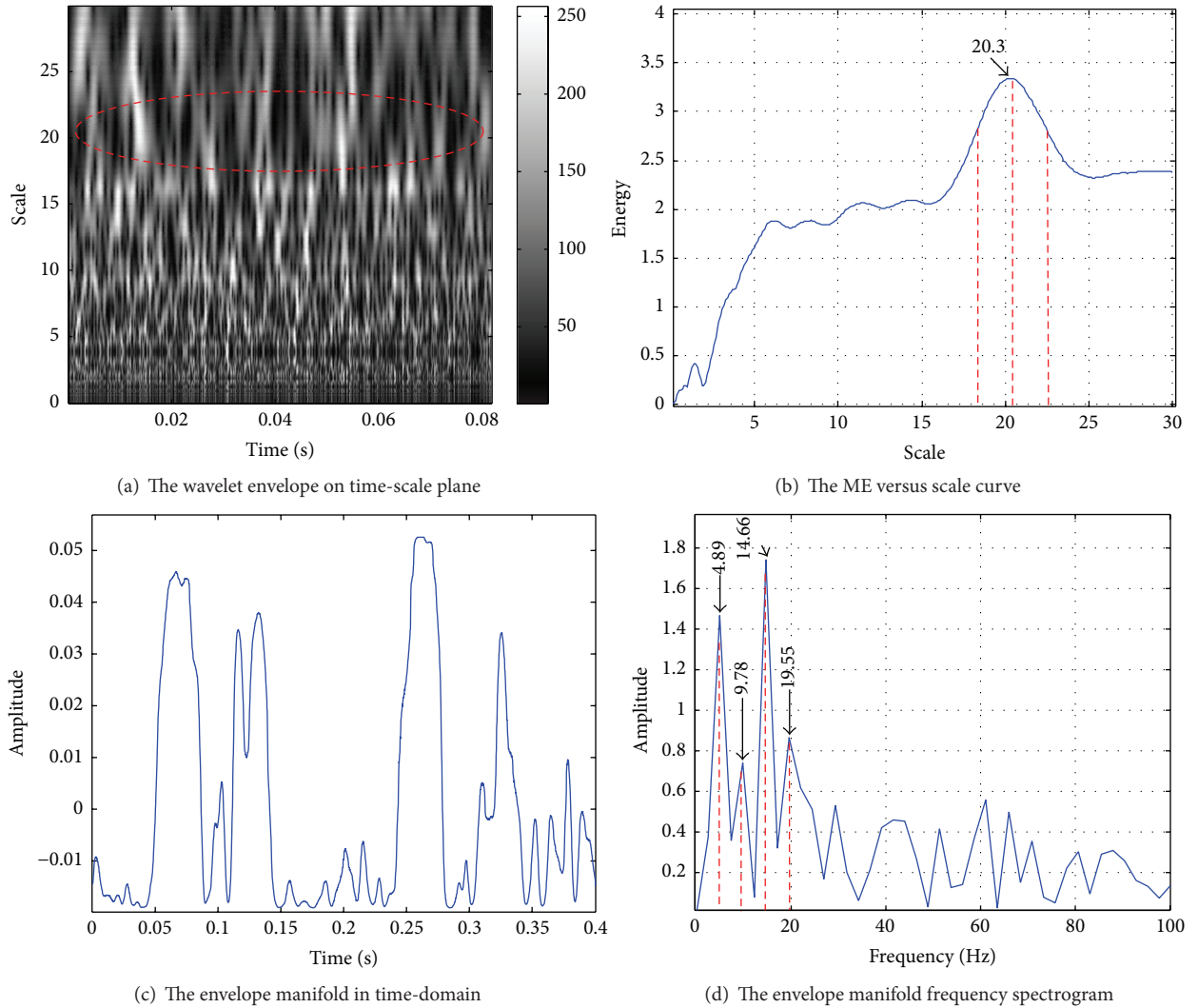


FIGURE 8: The envelope manifold result of contaminated signal with SNR = -10 dB.

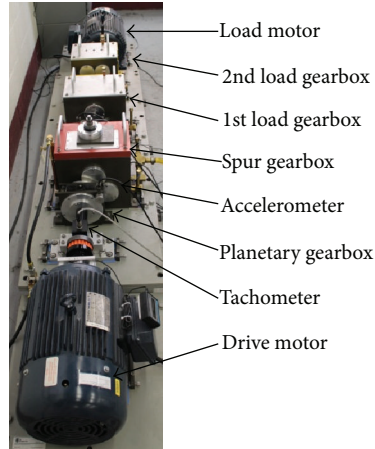


FIGURE 9: The planetary gearbox rig.

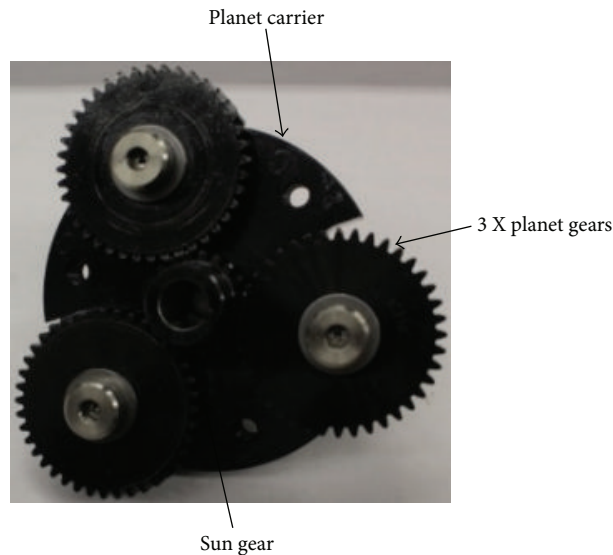


FIGURE 10: The planetary gear set.

TABLE 3: The working parameters of experiments.

Parameters	Value (Hz)
Sun gear frequency (f_s)	25
Planet gear meshing frequency (f_m)	546.88
Planet carrier rotation frequency (f_{ca})	5.47
Planet gear pass frequency (f_{pp})	21.88
Planet gear rotation frequency (f_{pr})	9.72
Faulty planet gear frequency (f_{pf})	15.19

is the man-made tooth missing planet gear that simulates the local fault, and the third is the teeth surface worn planet gear that simulates the distributed fault.

During experiments, the rotation speed of drive motor is set to 1500 rpm. The working parameters of the planetary gearbox in the experiments can be computed which are listed

in Table 3. The collected vibration signals in practical experiments are very complicated because of the abundant components in every frequency band. These practical vibration signals are analyzed with envelope manifold demodulation method to extract the fault features properly as follows.

4.2. Experiment Analysis

4.2.1. Normal Planet Gear. In order to demonstrate the denoising effect of envelope manifold demodulation at first, the wavelet envelope at the central scale and the envelope manifold are studied for comparison. The central scale is 18.2 according to ME indicator. The corresponding meshing frequency, respectively, is 549.5 Hz. But the central scale, respectively, is 8.0 or 1.8 according to SI or SK. The corresponding frequency, respectively, is 1250 Hz or 5555.6 Hz. So the ME indicator is most suitable for identifying the planet gear meshing frequency in the practical experiments.

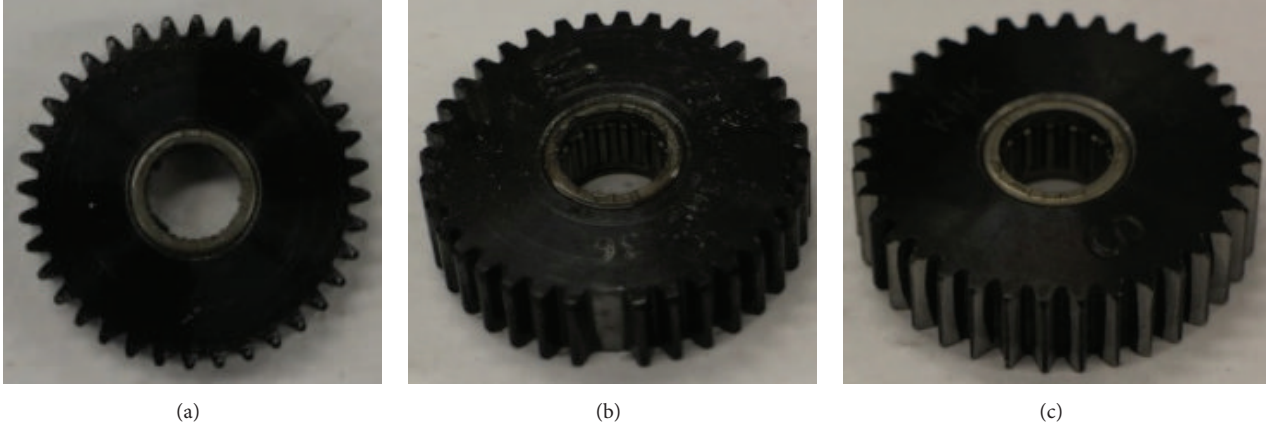


FIGURE 11: The experimental planet gears.

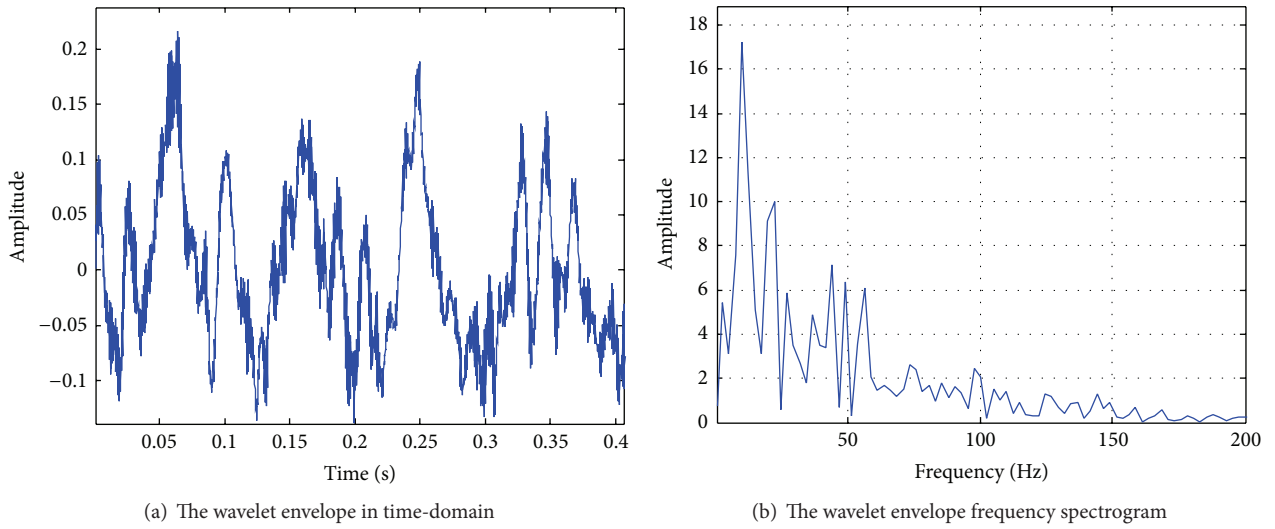


FIGURE 12: The wavelet envelope at the central scale of normal planet gear.

The wavelet envelope at the central scale is shown in Figure 12(a) and the wavelet envelope frequency spectrogram is shown in Figure 12(b). After manifold learning, the envelope manifold and the frequency spectrogram are shown in Figure 13. The in-band noise causes the distortion of wavelet envelope. The characteristic frequency of envelope manifold is clearer than the wavelet envelope by comparing the frequency spectrograms in these figures.

The meshing vibration signal of planetary gearbox is modulated by different meshing phases, varied propagation paths, and even the manufacture error of the gear pairs. So in the envelope manifold spectrogram of the normal planet gear shown in Figure 13(b), the characteristic frequencies of f_{pp} , f_{pr} , $f_{pp} + f_{ca}$, $f_{pp} + 2f_{ca}$, $2f_{pp}$, $2f_{pp} + f_{ca}$, $2f_{pp} + 2f_{ca}$, ... can be recognized. The characteristic frequencies are related to f_{pp} , f_{pr} , and f_{ca} but not associated with the faulty planet gear frequency. From spectrogram, we can find the characteristic frequencies caused by the manufacture error, that is, the unbalance of the planet carrier and multiple planet gears.

Their amplitudes are not big. So there is no fault on the planet gears.

4.2.2. Tooth Missing Planet Gear. The envelope manifold of the tooth missing planet gear is shown in Figure 14. The characteristic frequencies of f_{pf} , f_{pr} , $f_{pp} + f_{pf}$, $f_{pp} + f_{ca}$, $f_{pp} + 2f_{ca}$, ... can be seen in the frequency spectrogram. The modulating frequency of faulty planet gear f_{pf} can be extracted from the demodulated spectrum. f_{pf} , f_{pp} , and f_{pr} jointly modulated the meshing frequency of the planet gear. f_{pf} and $f_{pp} + f_{pf}$ become the mainly modulating frequencies besides those characteristic frequencies of normal planet gear. The faulty planet gear frequency and the harmonic frequencies can be distinguished in the frequency spectrogram.

4.2.3. Teeth Surface Worn Planet Gear. The envelope manifold of the teeth surface worn planet gear is shown in Figure 15. The characteristic frequencies of f_{ca} , $f_{pp} + f_{pf}$,

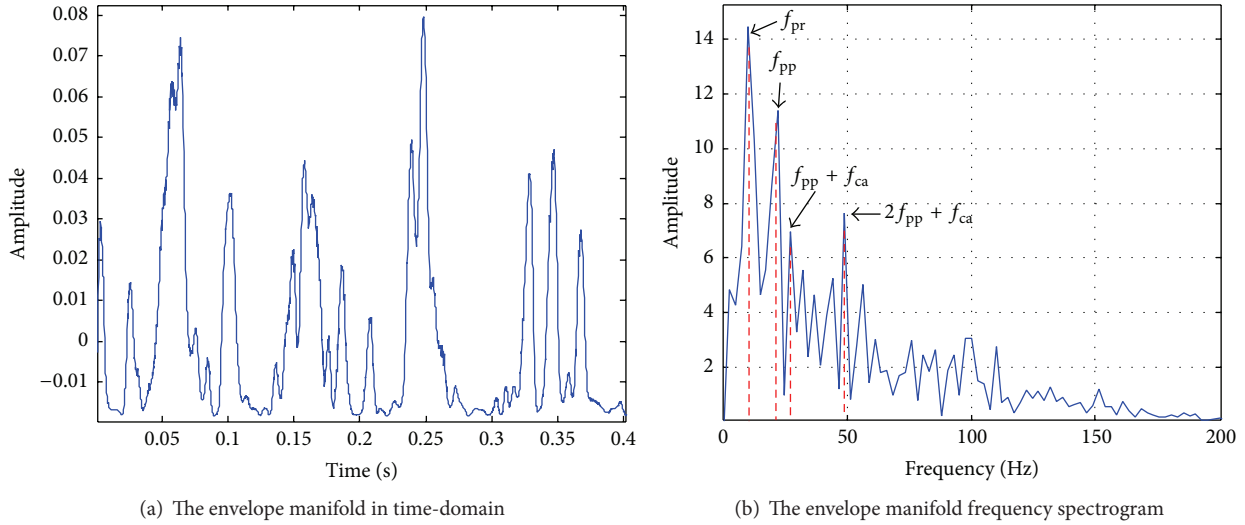


FIGURE 13: The envelope manifold of normal planet gear.

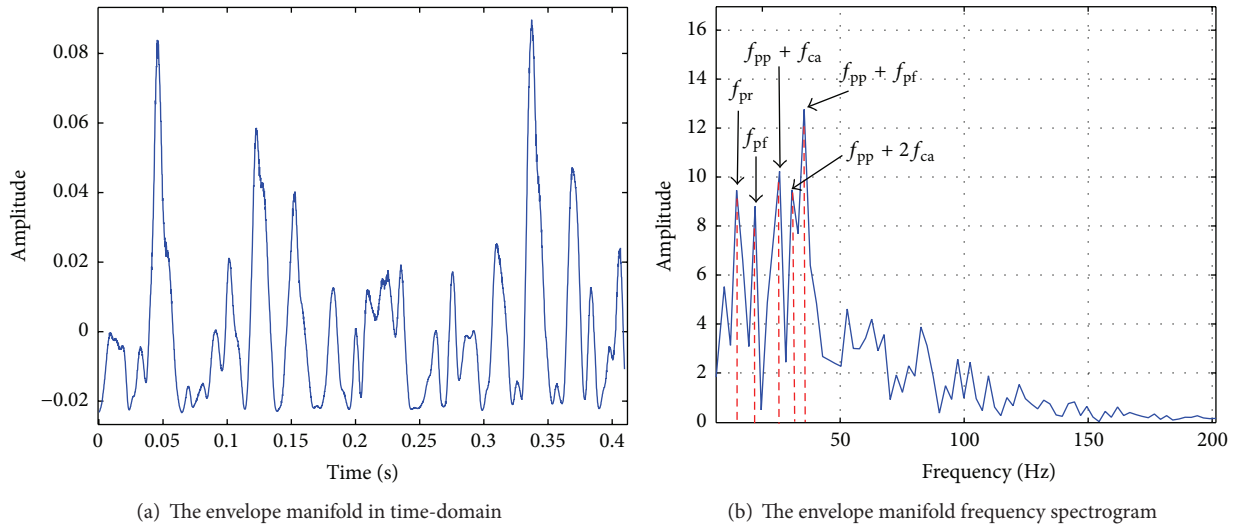


FIGURE 14: The envelope manifold of tooth missing planet gear.

$f_{pp} + 2f_{ca}$, $f_{pf} + f_{ca}$, $f_{pf} + f_{pr}$, ... can be viewed in the frequency spectrogram. Because there is just one teeth surface worn planet gear in the gearbox, the unbalance of the planet carrier increases dramatically. The effect of planet carrier characteristic frequency is enhanced. When the teeth surface worn planet gear meshes with mating gears, it can cause the faulty planet gear characteristic frequency. And so the frequencies of $f_{pf} + f_{pr}$ and $f_{pf} + f_{ca}$ appear in the power spectrogram. The teeth surface worn planet gear can be identified by this way.

The planetary gearbox rig sets and experiment conditions are different from each other. All the experiment results are based on the special rig set and experiment condition, but the experiments validate the effectiveness of the envelope manifold demodulation methodology.

5. Conclusions

In this paper, the envelope manifold demodulation methodology was introduced to implement the fault diagnosis of planetary gearbox. The method consisted of the complex wavelet transform, manifold learning, and frequency spectrogram analysis method. The continuous wavelet transform with complex Morlet wavelet was utilized to extract the envelope for demodulation of the planetary gears meshing vibration signal at first. The scale band selection was actualized through mean envelope energy (ME) indicator to locate the meshing frequency and remove the noisy signal not within the meshing frequency band. Then, the manifold learning method is applied to extract the intrinsic manifold of the envelope and reduce the effect of in-band noise. At last,

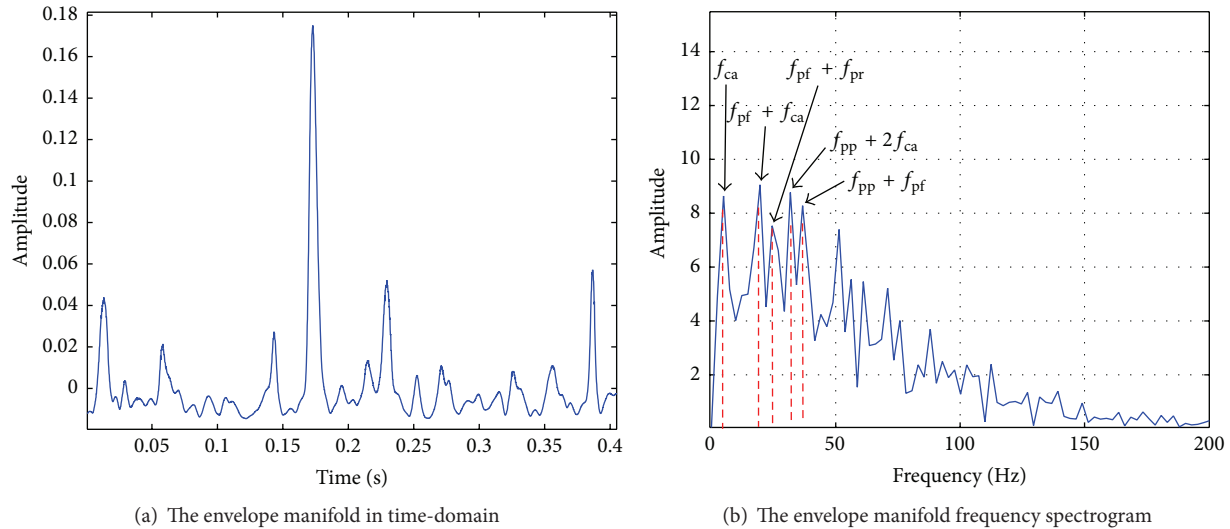


FIGURE 15: The envelope manifold of teeth surface worn planet gear.

the frequency spectrogram is used to show the characteristic frequency of the faulty planetary gears meshing envelope. By this method, the effect of noise among the vibration signals was immensely weakened, the envelope manifold structure was clearly revealed, and the fault characteristics of planetary gearbox were conveniently extracted. The result of simulated signal and experimental dataset all verified the effectiveness of the method. This method revealed the intrinsic characteristics of the planetary gearbox vibration signal. It was observed that this method outperformed other approaches in various conditions. The further work of us will be research on the exact mechanism of the planetary gearbox vibrations based on the results of this paper.

Conflict of Interests

The authors declare that there is no conflict of interests regarding the publication of this paper.

Acknowledgments

This project is supported by the National Natural Science Foundation of China (51275030) and the Fundamental Research Funds for the Central Universities (2011JBM093).

References

- [1] J. McNames, "Fourier series analysis of epicyclic gearbox vibration," *Journal of Vibration and Acoustics*, vol. 124, no. 1, pp. 150–152, 2002.
- [2] J. L. Chen, Y. Y. Zi, Z. J. He, and X. D. Wang, "Construction of adaptive redundant multiwavelet packet and its application to compound faults detection of rotating machinery," *Science China Technological Sciences*, vol. 55, no. 8, pp. 2083–2090, 2012.
- [3] H. L. Sun, Y. Y. Zi, Z. J. He, J. Yuan, X. Wang, and L. Chen, "Customized multiwavelets for planetary gearbox fault detection based on vibration sensor signals," *Sensors*, vol. 13, no. 1, pp. 1183–1209, 2013.
- [4] Y. G. Lei, D. Han, J. Lin, and Z. He, "Planetary gearbox fault diagnosis using an adaptive stochastic resonance method," *Mechanical Systems and Signal Processing*, vol. 38, no. 1, pp. 113–124, 2013.
- [5] Y. G. Lei, J. Lin, M. J. Zuo, and Z. J. He, "Condition monitoring and fault diagnosis of planetary gearboxes: a review," *Measurement*, vol. 48, no. 2, pp. 292–305, 2014.
- [6] F. Chaari, T. Fakhfakh, and M. Haddar, "Analytical investigation on the effect of gear teeth faults on the dynamic response of a planetary gear set," *Noise & Vibration Worldwide*, vol. 37, no. 8, pp. 9–15, 2006.
- [7] Z. Cheng and N. Q. Hu, "Quantitative damage detection for planetary gear sets based on physical models," *Chinese Journal of Mechanical Engineering*, vol. 25, no. 1, pp. 190–196, 2012.
- [8] Z. Feng and M. J. Zuo, "Vibration signal models for fault diagnosis of planetary gearboxes," *Journal of Sound and Vibration*, vol. 331, no. 22, pp. 4919–4939, 2012.
- [9] P. D. McFadden, "A technique for calculating the time domain averages of the vibration of the individual planet gears and the sun gear in an epicyclic gearbox," *Journal of Sound and Vibration*, vol. 144, no. 1, pp. 163–172, 1991.
- [10] Y. G. Lei, D. T. Kong, J. Lin, and M. J. Zuo, "Fault detection of planetary gearboxes using new diagnostic parameters," *Measurement Science and Technology*, vol. 23, no. 5, Article ID 055605, 2012.
- [11] W. D. Mark, "Stationary transducer response to planetary-gear vibration excitation II: effects of torque modulations," *Mechanical Systems and Signal Processing*, vol. 23, no. 7, pp. 2253–2259, 2009.
- [12] F. Chaari, T. Fakhfakh, and M. Haddar, "Dynamic analysis of a planetary gear failure caused by tooth pitting and cracking," *Journal of Failure Analysis and Prevention*, vol. 6, no. 2, pp. 73–78, 2006.
- [13] Y. Jiang, B. Tang, Y. Qin, and W. Liu, "Feature extraction method of wind turbine based on adaptive Morlet wavelet and SVD," *Renewable Energy*, vol. 36, no. 8, pp. 2146–2153, 2011.
- [14] T. Barszcz and R. B. Randall, "Application of spectral kurtosis for detection of a tooth crack in the planetary gear of a wind

- turbine,” *Mechanical Systems and Signal Processing*, vol. 23, no. 4, pp. 1352–1365, 2009.
- [15] R. Zimroz and W. Bartelmus, “Gearbox condition estimation using cyclostationary properties of vibration signal,” *Key Engineering Materials*, vol. 413–414, no. 1, pp. 471–478, 2009.
- [16] J. Zheng, J. Cheng, and Y. Yang, “Multi-scale permutation entropy based rolling bearing fault diagnosis,” *Shock and Vibration*, vol. 2014, Article ID 154291, 8 pages, 2014.
- [17] W. Caesarendra, B. Kosasih, A. K. Tieu, and C. A. S. Moodie, “Application of the largest Lyapunov exponent algorithm for feature extraction in low speed slew bearing condition monitoring,” *Mechanical Systems and Signal Processing*, vol. 50–51, no. 1, pp. 116–138, 2015.
- [18] R. Q. Yan and R. X. Gao, “Approximate entropy as a diagnostic tool for machine health monitoring,” *Mechanical Systems and Signal Processing*, vol. 21, no. 2, pp. 824–839, 2007.
- [19] W. J. Wang, Z. T. Wu, and J. Chen, “Fault identification in rotating machinery using the correlation dimension and bispectra,” *Nonlinear Dynamics*, vol. 25, no. 4, pp. 383–393, 2001.
- [20] J. Wang, Q. B. He, and F. R. Kong, “Multiscale envelope manifold for enhanced fault diagnosis of rotating machines,” *Mechanical Systems and Signal Processing*, vol. 52–53, no. 1, pp. 376–392, 2015.
- [21] Q. He, Y. Liu, Q. Long, and J. Wang, “Time-frequency manifold as a signature for machine health diagnosis,” *IEEE Transactions on Instrumentation and Measurement*, vol. 61, no. 5, pp. 1218–1230, 2012.
- [22] J. Wang, Q. B. He, and F. R. Kong, “Automatic fault diagnosis of rotating machines by time-scale manifold ridge analysis,” *Mechanical Systems and Signal Processing*, vol. 40, no. 1, pp. 237–256, 2013.
- [23] J. Wang and Q. B. He, “Exchanged ridge demodulation of time-scale manifold for enhanced fault diagnosis of rotating machinery,” *Journal of Sound and Vibration*, vol. 333, no. 11, pp. 2450–2464, 2014.
- [24] D. M. Blunt and J. A. Keller, “Detection of a fatigue crack in a UH-60A planet gear carrier using vibration analysis,” *Mechanical Systems and Signal Processing*, vol. 20, no. 8, pp. 2095–2111, 2006.
- [25] R. Q. Yan and R. X. Gao, “Multi-scale enveloping spectrogram for vibration analysis in bearing defect diagnosis,” *Tribology International*, vol. 42, no. 2, pp. 293–302, 2009.
- [26] J. Antoni, “The spectral kurtosis: a useful tool for characterising non-stationary signals,” *Mechanical Systems and Signal Processing*, vol. 20, no. 2, pp. 282–307, 2006.
- [27] X. H. Zhang, J. S. Kang, L. Xiao, J. Zhao, and H. Teng, “A new improved kurtogram and its application to bearing fault diagnosis,” *Shock and Vibration*, vol. 2015, Article ID 385412, 22 pages, 2015.
- [28] Y. X. Wang and M. Liang, “Identification of multiple transient faults based on the adaptive spectral kurtosis method,” *Journal of Sound and Vibration*, vol. 331, no. 2, pp. 470–486, 2012.
- [29] P. W. Tse and D. Wang, “The design of a new sparsogram for fast bearing fault diagnosis: part 1 of the two related manuscripts that have a joint title as ‘two automatic vibration-based fault diagnostic methods using the novel sparsity measurement—parts 1 and 2,’” *Mechanical Systems and Signal Processing*, vol. 40, no. 2, pp. 499–519, 2013.
- [30] I. S. Bozchalooi and M. Liang, “A joint resonance frequency estimation and in-band noise reduction method for enhancing the detectability of bearing fault signals,” *Mechanical Systems and Signal Processing*, vol. 22, no. 4, pp. 915–933, 2008.
- [31] S. T. Roweis and L. K. Saul, “Nonlinear dimensionality reduction by locally linear embedding,” *Science*, vol. 290, no. 5500, pp. 2323–2326, 2000.
- [32] J. B. Tenenbaum, V. De Silva, and J. C. Langford, “A global geometric framework for nonlinear dimensionality reduction,” *Science*, vol. 290, no. 5500, pp. 2319–2323, 2000.
- [33] A. J. Izenman, “Introduction to manifold learning,” *Wiley Interdisciplinary Reviews: Computational Statistics*, vol. 4, no. 5, pp. 439–446, 2012.
- [34] M. Belkin and P. Niyogi, “Laplacian eigenmaps and spectral techniques for embedding and clustering,” in *Advances in Neural Information Processing Systems*, vol. 14, pp. 585–591, MIT Press, 2002.
- [35] S. Natarajan, “Gear box fault diagnosis using hilbert transform and study on classification of features by support vector machine,” *International Journal of Hybrid Information Technology*, vol. 7, no. 4, pp. 69–82, 2014.
- [36] P. Flandrin, G. Rilling, and P. Gonçalvés, “Empirical mode decomposition as a filter bank,” *IEEE Signal Processing Letters*, vol. 11, no. 2, pp. 112–114, 2004.

Research Article

Development of a Vehicle-Bridge-Soil Dynamic Interaction Model for Scour Damage Modelling

L. J. Prendergast,¹ D. Hester,² and K. Gavin¹

¹*School of Civil, Structural and Environmental Engineering, University College Dublin, Newstead, Belfield, Dublin 4, Ireland*

²*School of Planning, Architecture and Civil Engineering, Queen's University Belfast, University Road, Belfast BT7 1NN, UK*

Correspondence should be addressed to L. J. Prendergast; luke.prendergast@ucdconnect.ie

Received 1 July 2015; Revised 19 August 2015; Accepted 23 August 2015

Academic Editor: Ruqiang Yan

Copyright © 2016 L. J. Prendergast et al. This is an open access article distributed under the Creative Commons Attribution License, which permits unrestricted use, distribution, and reproduction in any medium, provided the original work is properly cited.

Damage detection in bridges using vibration-based methods is an area of growing research interest. Improved assessment methodologies combined with state-of-the-art sensor technology are rapidly making these approaches applicable for real-world structures. Applying these techniques to the detection and monitoring of scour around bridge foundations has remained challenging; however this area has gained attraction in recent years. Several authors have investigated a range of methods but there is still significant work required to achieve a rounded and widely applicable methodology to detect and monitor scour. This paper presents a novel Vehicle-Bridge-Soil Dynamic Interaction (VBSDI) model which can be used to simulate the effect of scour on an integral bridge. The model outputs dynamic signals which can be analysed to determine modal parameters and the variation of these parameters with respect to scour can be examined. The key novelty of this model is that it is the first numerical model for simulating scour that combines a realistic vehicle loading model with a robust foundation soil response model. This paper provides a description of the model development and explains the mathematical theory underlying the model. Finally a case study application of the model using typical bridge, soil, and vehicle properties is provided.

1. Introduction

1.1. Motivation for Modelling Damage in Civil Engineering Structures. Farrar and Worden [1] give a very useful overview of the area of structural health monitoring (SHM). They point out that the motivation for governments and private companies implementing this technology is due to the economic and potentially lifesaving impact it can have. Dimarogonas [2] points out that online damage detection/monitoring started in the early 1970s when power companies started looking at developing ways of identifying defects in rotating shafts while machinery was in use. To date this kind of condition monitoring of rotating machinery has been the most successful application of SHM and it is almost entirely non-model based [1]. Effectively these machines have quite a narrow range of operating behaviours so anomalies are relatively easy to identify. As there were many of these machines in service, over time it was thus possible to develop databases that allowed specific types of damage (e.g., chipped gear teeth or damaged bearings) to be identified from particular features

of the machine's vibration signature. This concept of looking for damage-sensitive features in a response signal is central to SHM. Typically an SHM algorithm works by seeking a damage feature in a response signal or by identifying a change in some characteristic of the structure when it is damaged, for example, natural frequency, mode shapes, or damping. For rotating machinery these damage features could be identified relatively easily through experiments or by correlating monitoring data with subsequent servicing records. The first instance of applying the SHM philosophy to large scale civil engineering structures was in the 1970s and 80s when the oil industry began attempting to apply this technology to offshore platforms. In comparison to damage arising in rotating machines, this time the structures were large and multiple damage locations/severities were possible so the nature of the damage features was typically unknown. Therefore, it was necessary to simulate candidate damage scenarios using numerical models, in order to, for example, observe how that damage affected the frequency of the platform. The idea behind this was that if this frequency was

subsequently observed in the field it could be correlated to a given damage scenario. In general the challenges of applying vibration-based SHM to offshore platforms are significant as factors such as variations in the mass of the structure due to changes in the mass of the storage tanks and changes in the amount of marine growth on the structure can prove problematic.

The development of SHM tools for bridge engineering faces the same challenges as the oil industry in that it is very rare that one can take a full size test piece and apply damage for the purpose of developing monitoring tools. In fact it is practically unheard of in bridge engineering, as the structures themselves are just too valuable/important to interfere with. Therefore when researchers wish to try and develop a new SHM algorithm to detect a particular type of defect in the structure, the first task is to try and understand how damage affects the response of the structure. To establish this, their options (broadly speaking) are to use a computer model [3] and/or a laboratory experiment using a scaled model of the structure [4]. Occasionally it will be possible to test at full scale when a bridge is due to be retrofitted, for example, a scoured but retrofitted bridge in Italy; see [5]. However, in many cases the first option is a computer model to undertake simulations of candidate damage scenarios. The challenge, therefore, is to develop a model that outputs realistic results. A numerical model that outputs signals that are representative of those likely to be encountered on the real structure is a very useful tool when trying to develop new SHM algorithms. This paper aims to develop just such a model, as, by including vehicle-bridge interaction and soil-structure interaction, every effort is made to make the loading (applied to the bridge) and the (soil) boundary conditions of the model as realistic as possible. It should be noted that the aim of this paper is not to develop a new SHM technique for scour detection but to present the basis of a model to make it easy for others to test emerging SHM techniques by allowing them to generate realistic bridge response signals occurring due to foundation scour. Section 1.2 gives some examples of numerical models developed to simulate damage in beam-like structures, where the model outputs (e.g., acceleration, velocity, or displacement signals) were subsequently used as inputs to damage detection algorithms. This section also provides a discussion on previous works focussed on modelling scour damage.

1.2. Modelling Structural Damage for SHM Algorithm Development. Over the past two decades several authors have prepared models of damaged structures with a view to developing SHM algorithms to detect this type of damage. A particular focus has been given to models which represent localised damage in a structure (e.g., cracking or section loss). Ostachowicz and Krawczak [6] describe the different methods commonly used to model structural stiffness loss due to damage. Friswell and Penny [7] give a very useful overview on crack modelling for SHM. They point out that approaches for modelling cracks in beam type structures typically fall into three categories: local stiffness reduction [8], discrete spring models [9], and complex models in two or three dimensions. They compare the three approaches and

broadly speaking they conclude that, for structural health monitoring which utilises low frequency vibration, simple models of crack flexibility based on beam elements are adequate.

Other authors have developed models to simulate the response signals of damaged beam structures to moving loads and then used the signals from these models as inputs to SHM algorithms. A number of authors have simulated the structure as having a localised loss in stiffness and then calculated the response to a moving point force [10]. Hester and González [11] modelled a similar type of damage; however they modelled the moving load as a sprung vehicle to incorporate vehicle-bridge interaction effects, that is, to make the simulated response signals as realistic as possible. This is important when numerically testing the versatility of a new SHM algorithm before applying it to a real structure. Others have postulated that the occurrence of damage will affect the damping of the bridge and prepared numerical models to simulate this by analysing the vehicle acceleration signals output from the model [12]; that is, this is an indirect monitoring approach as the vehicle response passing over a damaged bridge is used to detect the damage feature.

In terms of scour modelling, several authors have investigated the effect of scour on the static and dynamic properties of bridges using numerical methods. The principle underlying these approaches is that, during scour, loss of soil contact occurs which leads to higher applied stress over the area of soil remaining in contact with the foundation. This, coupled with the nonlinear stiffness of soils, leads to lower operational system stiffness [13]. Therefore scour presence should be detectable as a change in the dynamic properties of the structure. Ju [14] developed a 3D FE model of a bridge incorporating soil-structure and fluid-structure interaction to assess the magnitude of the change in natural frequency of the bridge with increasing scour. They validated the bridge natural frequencies from the model against a full-scale field experiment and then used the numerical model to study various scour conditions and how it affected the bridge's natural frequency. They concluded that scour causes a reduction in bridge natural frequency but the magnitude of the frequency change with scour is affected by varying foundation geometry and layering in foundation soils. Chen et al. [15] developed a full FE model of a cable-stayed bridge with a pylon and a pier. They updated the model properties to obtain a match to modal data obtained from the actual structure. They then used known data about the pylon foundation condition to obtain representative soil stiffness (matching the stiffness of the actual soil). The numerical model was then used to update the scour depth around the pier until the predicted frequency data matched the observed data. In this case, the numerical model was used to ascertain the actual scour condition around the real pier and this paper serves as a successful real-life application of a vibration-based scour detection method. Klinga and Alipour [16] developed a numerical model to assess the effect of scour on various static and dynamic performance features of a bridge. They used their model to perform pushover analyses, buckling analyses, and modal analyses under extreme scour conditions to assess the effect of scour on the various bridge elements such as

the piles and columns. They present a number of case studies of affected performance features due to scour.

Unlike authors working in the area of bridge damage via cracking and so forth, for the purpose of scour detection, many authors have developed models to specifically perform a single task only, that is, to establish the depth of scour around a foundation element or assess the change in bridge performance under scoured conditions. No authors to date have developed a model capable of rapidly modelling a variety of bridge scour scenarios with the flexibility to test emerging SHM techniques. This paper aims to develop a numerical model that can generate dynamic signals (displacement, velocity, and acceleration) from a bridge under a variety of input loading/scour scenarios in order to allow users to develop and/or test SHM algorithms. Because of the increasing popularity of integral bridges, the structure modelled in this paper is a two-span integral bridge. Details about this type of bridge are given in Section 2.1. Section 1.3 summarises the aims of the model presented in this paper.

1.3. Generic Algorithm for Modelling Integral Bridge Scour

1.3.1. Method. In order to develop a representative vehicle-bridge interaction model for the purpose of simulating the effect of scour on the dynamic response of an integral bridge, a number of key assumptions are made. In the first instance, to aid in the rapid generation of dynamic data, the integral bridge is assumed to act as a 2D frame system. The reason behind this is twofold: (i) it is assumed that the dynamic movements of interest for scour on an integral bridge predominately take place in the longitudinal direction (it is acknowledged that this assumption may not hold true for other bridge types; e.g., [15] found that for a cable-stayed bridge the first horizontal flexural and second torsional mode of the pylon were the most sensitive to scour) and (ii) 3D numerical modelling is very user and computationally costly and the resulting signals of interest are not expected to vary significantly from those in a 2D system. For these reasons, transverse and torsional motion of the integral bridge is neglected. The benefit of a 2D frame system is that a variety of representative bridges can be rapidly modelled, as the user only has to specify a relatively small number of parameters (bridge element structural and geometric properties, vehicle parameters such as axle spacing and mass). For the purpose of generating signals to test emerging SHM concepts, this is deemed adequate.

Scour can be modelled around both the central pier and the left and right abutments of the bridge and is considered as the increase in effective length of the bridge pier/abutments corresponding to a decrease in bed elevation level. The stiffness of the soil can be varied to be representative of soils from loose to dense in situ conditions that are typical of the range of ground conditions encountered in riverine environments. The foundation scour model used in this paper is derived from previously validated work undertaken by the authors (see Section 1.3.2). The method for modelling the various bridge elements, namely, deck, abutments, pier, and soil, is discussed in detail in Section 2.

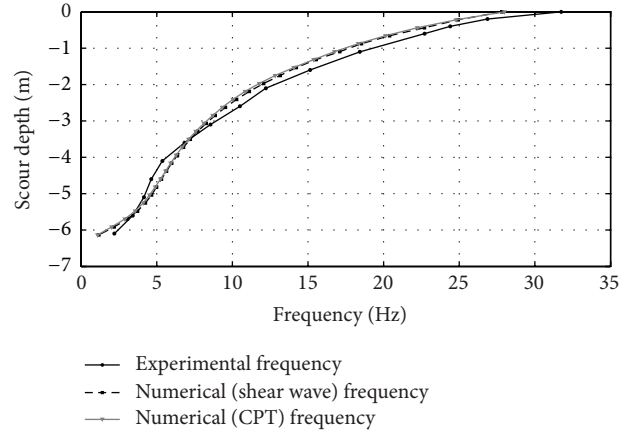


FIGURE 1: Frequency change with scour for experimental and numerical models [17].

1.3.2. Validation of Scour Model. The greatest uncertainty with regard to bridge input parameters relates to the soil stiffness. It is imperative to specify soil properties that adequately reflect the boundary stiffness effects of the soil likely to be encountered in the field for the purpose of accurate scour modelling. The method for deriving soil stiffness for scour evaluation comes from an experimental investigation undertaken by [17]. In this work, the authors measured the change in the natural frequency of a full-scale pile to manually induced scour. The field measurements were compared to numerical models developed using a Winkler spring-beam methodology (see Section 2.3). Two different methods were used to estimate the soil stiffness; the first derived soil stiffness based on the shear modulus of the soil obtained from the Multichannel Analysis of Surface Waves (MASW) (see [18]); the second method used estimates of shear modulus from a correlation to measured Cone Penetration Test (CPT) tip resistance (q_c) data measured at the experimental site. The results of the frequency change with scour are reproduced in Figure 1.

Figure 1 shows that the experimental data and the numerical predictions from both numerical models match well. Therefore, for the purpose of scour modelling, the method developed in [17, 19] is used to generate representative soil profiles (and corresponding spring stiffness coefficients) for a range of soil density states. This is further discussed in the next sections.

2. Structural Model Development

The numerical model is developed in the MATLAB programming environment. The various components of the model are described in the following subsections. Section 2.1 describes the integral bridge to be modelled. Section 2.2 describes the mathematical modelling philosophy. Sections 2.3 and 2.4 describe how the interaction effects with foundation soil and vehicle are considered, respectively.

2.1. Integral Bridges. Integral bridges are becoming increasingly popular as they do not require a conventional expansion

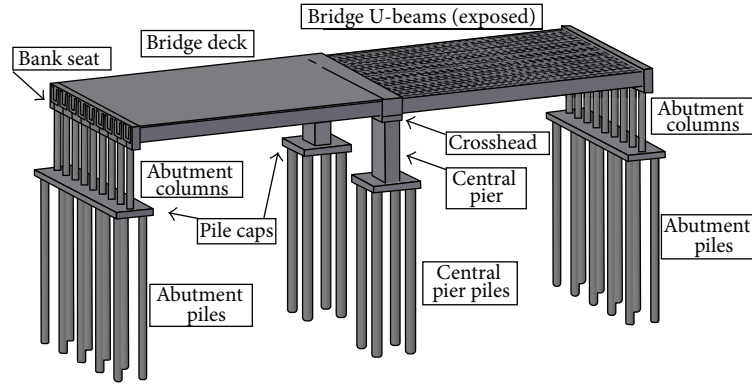


FIGURE 2: 3D rendering showing typical structural arrangement of a two-span integral bridge with flexible abutment supports.

joint. The desire to (where possible) avoid using expansion joints is due to the fact that they tend to give maintenance problems. For example, after surveying approximately two hundred concrete highway bridges in the UK, Wallbank (1989) (cited in [20]) found that expansion joints were a source of costly and disruptive maintenance work. In response to this finding, in 1996 the UK Highways Agency published Technical Note BA 42 which recommended (with some exceptions) that for new bridges up to 60 m in length integral construction should be considered.

The Steel Construction Institute (2015) [21] gives a useful summary on the different types of integral bridges that have been used over the years. Broadly speaking integral bridges can be split into 4 types; (i) *frame abutments*: this is when the abutments form a portal frame with the bridge superstructure; (ii) *bank pad abutments*: in this type the bank pad end support is integral to the deck and the bank pad is able to slide and rotate on the soil; (iii) *flexible support abutments*: this is where the bank pad is supported by piles/columns that are not in contact with the soil; that is, they have an annular space around them, and this makes them more flexible and therefore better able to absorb the thermal movements of the bridge deck; and (iv) *semi-integral* (screen end abutments): in this case there is an end screen wall (at the end of the deck) which is integral to the deck beams; however this wall does not provide support to the beams. Instead support is provided by some other structural element (e.g., a piled bank seat) and bearings are used to accommodate deck movements.

In this paper the flexible support abutment type is modelled, as this form of construction is most commonly used. Figure 2 shows an annotated schematic 3D rendering of a typical two-span integral bridge with flexible abutment columns. The deck is formed from prestressed concrete U-beams and an in situ slab. The outline of the ends of the beams can be seen at the left hand end of the deck where the beams are cast into an end diaphragm/bank seat that is supported on the flexible columns. The deck beams can be seen on the right hand span (the deck slab is removed for illustrative purposes). No dimensions are indicated on the figure as the numerical model that is developed is intended to model bridges of this type but span length, pile length,

section modulus, and so forth can be defined by the user. In this model the longitudinal stability of the bridge is provided primarily by the central pier which is significantly stiffer (longitudinally) than the abutment columns. Figure 3 shows an integral bridge (flexible abutment type) in its completed state. For aesthetic reasons the abutment columns are often hidden from view in the completed structure, typically using reinforced earth, which is the approach used on the bridge shown in Figure 3.

2.2. Bridge Elements. The bridge structure is modelled as a 2D frame, whereby grouped geometric properties are used to model the various structural elements, namely, the deck, abutments, central pier, and the foundation piles. The bridge elements are modelled using 6-degree-of-freedom (6-DOF) Euler-Bernoulli frame elements [22]. The individual bridge elements are assembled together to create global mass $[\mathbf{M}_G]$ and stiffness $[\mathbf{K}_G]$ matrices for the full structure, using the assembly procedure outlined in [22]. The dynamic response of the bridge is governed by the second-order matrix differential equation shown in

$$\begin{aligned}
 & [\mathbf{M}_G] \begin{Bmatrix} \ddot{\mathbf{x}}_1(t) \\ \ddot{\mathbf{x}}_2(t) \\ \vdots \\ \ddot{\mathbf{x}}_N(t) \end{Bmatrix} + [\mathbf{C}_G] \begin{Bmatrix} \dot{\mathbf{x}}_1(t) \\ \dot{\mathbf{x}}_2(t) \\ \vdots \\ \dot{\mathbf{x}}_N(t) \end{Bmatrix} + [\mathbf{K}_G] \begin{Bmatrix} \mathbf{x}_1(t) \\ \mathbf{x}_2(t) \\ \vdots \\ \mathbf{x}_N(t) \end{Bmatrix} \\
 & = \begin{Bmatrix} \mathbf{F}_1(t) \\ \mathbf{F}_2(t) \\ \vdots \\ \mathbf{F}_N(t) \end{Bmatrix}, \tag{1}
 \end{aligned}$$

where $[\mathbf{M}_G]$, $[\mathbf{C}_G]$, and $[\mathbf{K}_G]$ are the $(N \times N)$ global mass, damping, and stiffness matrices for the model, respectively, and N is the total number of degrees of freedom in the system. The vector $\{\mathbf{x}(t)\}$ describes the displacement of every degree of freedom for each time step in the analysis. Similarly the vectors $\{\dot{\mathbf{x}}(t)\}$ and $\{\ddot{\mathbf{x}}(t)\}$ describe the velocity and acceleration of every degree of freedom for each time step. The vector

$\{\mathbf{F}(t)\}$ describes the external forces acting on each of the degrees of freedom for a given time step in the numerical model. The damping matrix $[\mathbf{C}_G]$ is calculated assuming a Rayleigh approach in line with the recommendations of [23]. The time-domain dynamic response of the system is obtained by solving (1) using numerical integration. In the model described in this paper, the Wilson- θ integration scheme is employed which is a special case of the linear acceleration method [24].

2.3. Winkler Soil Modelling. Dynamic soil-structure interaction covers a broad spectrum of applications from large-strain cyclic load-displacement regimes to small-strain low amplitude vibrations. Soil behaviour is highly nonlinear and in particular its stiffness changes nonlinearly with strain. The response of soil-structure systems is heavily dependent on the magnitude and the nature of external loading and a variety of methods exist that aim to accurately capture the behaviour of foundation systems. In this paper, it is assumed that the external loading from vehicles passing over the bridge will lead to very small lateral strains being imparted into the soil surrounding the piles. Therefore, it is assumed that the strains remain within the “small-strain” linear-elastic region of the soil response curve. This means the discretised soil impedances can be characterised by fixed value constants independent of the strain. The methods for modelling the contribution of the soil are discussed in the following subsections, namely, the mathematical assumptions underlying the process (Section 2.3.1) and the derivation of representative soil stiffness coefficients (Section 2.3.2).

2.3.1. Mathematical Assumptions. The bridge foundation comprises piled foundation elements embedded in soil. The soil is modelled using a Winkler framework, whereby the continuous soil layers are replaced by representative discrete, mutually independent, and closely spaced spring elements [25, 26]. These spring elements have two translational degrees of freedom (2 DOFs) and permit one-dimensional uniaxial movement along the longitudinal axis of the spring. For the purpose of dynamic interaction modelling with the bridge structure, the soil springs are assumed to provide dynamic impedance only and inertial effects are ignored. In modelling terms, the springs have a null mass matrix. The stiffness matrix formulation $[\mathbf{K}_{s,i}]$ for these spring elements is shown in

$$[\mathbf{K}_{s,i}] = k_{s,i} \begin{bmatrix} 1 & -1 \\ -1 & 1 \end{bmatrix}, \quad k_{s,i} \geq 0, \quad (2)$$

where $k_{s,i}$ is the stiffness coefficient of the i th spring element. As discussed previously $k_{s,i}$ remains constant with strain in the spring due to the assumption of linear-elasticity with small soil displacements. These springs are added/integrated into the global stiffness matrix $[\mathbf{K}_G]$ (for the full bridge structure) by coupling/“attaching” one end of the spring to the pile nodes in the model, that is, the pile nodes located below the assumed ground line. The free end of each spring is restricted from motion to model the confining effect of the soil by setting the permissible displacement of each of these



FIGURE 3: Two-span integral bridge with flexible abutment supports.

degrees of freedom to zero. Effectively every spring added to the model adds one extra degree of freedom to the global matrices $[\mathbf{M}_G]$, $[\mathbf{C}_G]$, and $[\mathbf{K}_G]$. A visualisation of the spring elements is shown in Figure 5.

2.3.2. Derivation of Soil Spring Stiffness Coefficients ($k_{s,i}$). Using a discrete spring modelling framework as per the Winkler regime, it is imperative to specify spring stiffness coefficients that accurately model the small-strain continuum soil behaviour at the soil-pile interfaces. In this paper, the method described in Prendergast et al. [19] is used to calculate representative soil stiffness coefficients for a range of soil states from loose to very dense sand.

The process involves (i) generating synthetic Cone Penetration Test (CPT) q_c profiles that correspond to the stresses measured when a cone tip passes through a loose, medium dense, and dense sand deposit (Section 2.3.2(1)), (ii) correlating these CPT q_c profiles to profiles of the small-strain shear modulus (G_0) for the three soil profiles adopted (Section 2.3.2(2)), and (iii) converting the shear modulus profiles into profiles of modulus of subgrade reaction (K) and hence into individual spring coefficients ($k_{s,i}$) (Section 2.3.2(3)).

(1) Hypothetical CPT q_c Profile. As part of a standard geotechnical site investigation, Cone Penetration Tests are often carried out whereby an instrumented cone is pushed into the soil at a constant rate and the tip stresses and side sleeve friction are measured at discrete depth intervals. Lunne and Christoffersen [27] proposed an expression relating the cone tip resistance q_c value with the soil’s effective stress (σ'_v) and relative density (D_r). A rearranged version of this expression is shown in

$$q_c = 60 (\sigma'_v)^{0.7} \exp(2.91D_r). \quad (3)$$

Using (3), a hypothetical CPT q_c profile can be derived from effective stress and relative density conditions. D_r values of 0.3 (30%), 0.5 (50%), and 0.8 (80%) are assumed to correspond to the properties of a loose, medium dense, and dense sand deposit, respectively [28], and are assumed constant with depth for uniform soils. The vertical effective stress can be calculated assuming values of bulk unit weight (γ_b) of 18, 19, and 20 kN m^{-3} to approximate loose, medium dense, and dense sand deposits and the bulk unit weight of water (γ_w) is assumed as 10 kN m^{-3} . Although these synthetic CPT q_c profiles are idealised, they do conform quite well to the values expected for the given soil conditions [29].

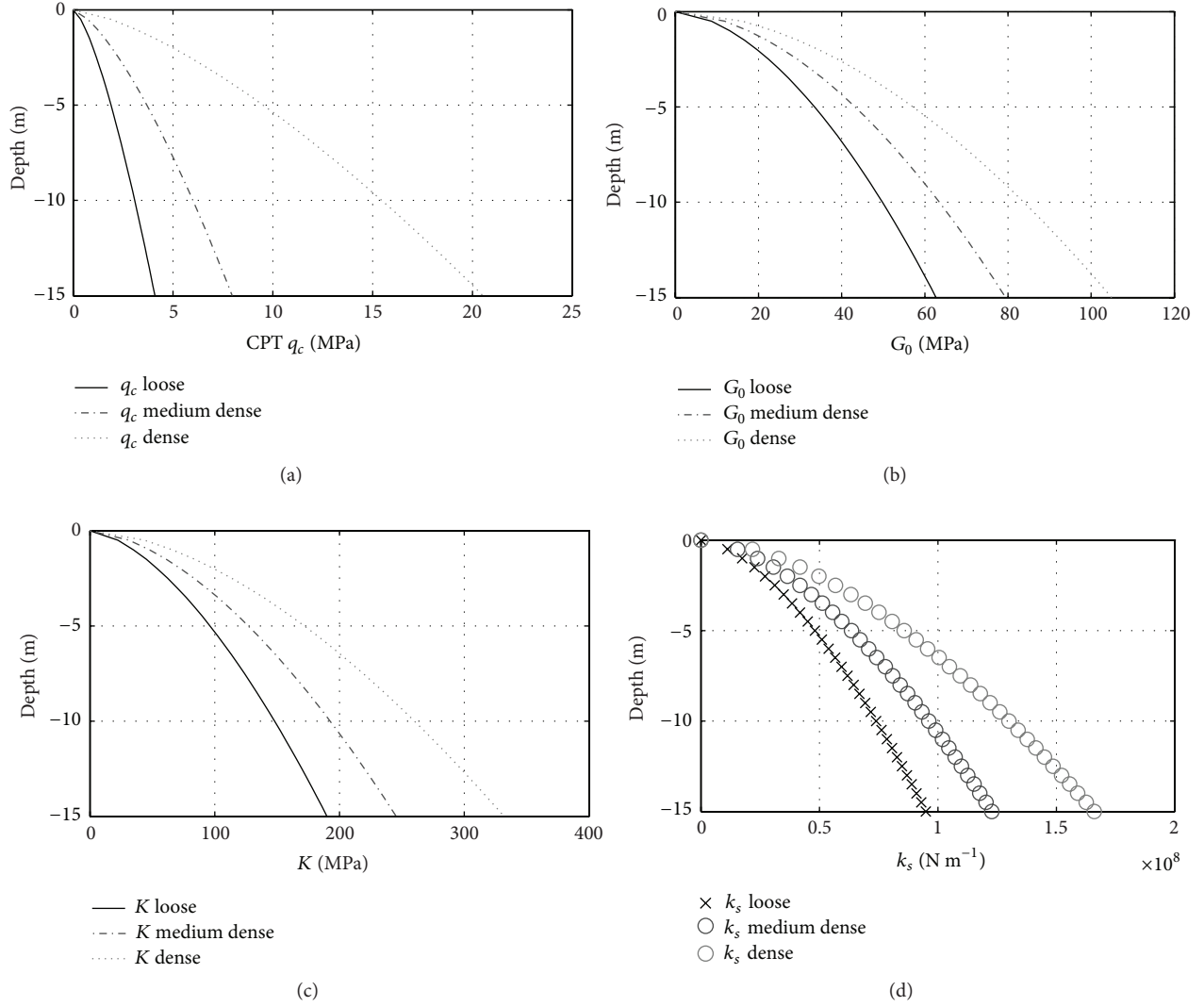


FIGURE 4: Example soil profiles. (a) CPT q_c profiles for loose, medium dense, and dense sand, (b) G_0 profiles, (c) modulus of subgrade reaction (K) profiles, and (d) individual k_s values for loose, medium dense, and dense sand.

Figure 4(a) shows typical q_c profiles generated using this approach.

(2) *Convert CPT q_c to Profiles of G_0 .* There are a number of correlations linking the CPT q_c value to the small-strain shear modulus (G_0) for a given soil deposit. In this paper, the expression suggested in the Imperial College design method (IC-05) for driven piles in sand and clays [30] is used. This expression was originally suggested by Baldi et al. [31] and is shown in

$$G_0 = q_c [A + B\eta - C\eta^2]^{-1}, \quad (4)$$

where $A = 0.0203$, $B = 0.00125$, $C = 1.216E - 6$, and $\eta = q_c (P_a \sigma'_v)^{-0.5}$, with $P_a = 100$ kPa and σ'_v = vertical effective stress (kPa). Using (4), the synthetic q_c profiles for loose, medium dense, and dense sand may be converted to profiles

of the small-strain shear modulus. An example of this for a 15 m deep stratum is shown in Figure 4(b).

(3) *Calculate Modulus of Subgrade Reaction (K) Profile.* The first step in calculating the modulus of subgrade reaction from G_0 is to convert G_0 data to small-strain Young's modulus (E_0) data using the relation shown in

$$E_0 = 2G_0 (1 + \nu), \quad (5)$$

where ν , Poisson's ratio, is assumed as 0.1. Using E_0 profile for the soil, the modulus of subgrade reaction (K) for the soil-pile interface may be calculated using the expression shown in [17, 32]

$$K = \frac{1.0E_0}{1 - \nu^2} \left[\frac{E_0 D^4}{E_p I_p} \right]^{1/12}, \quad (6)$$

where D is the effective diameter of the pile group (m), E_p is Young's modulus of the pile material (N m^{-2}), and I_p is

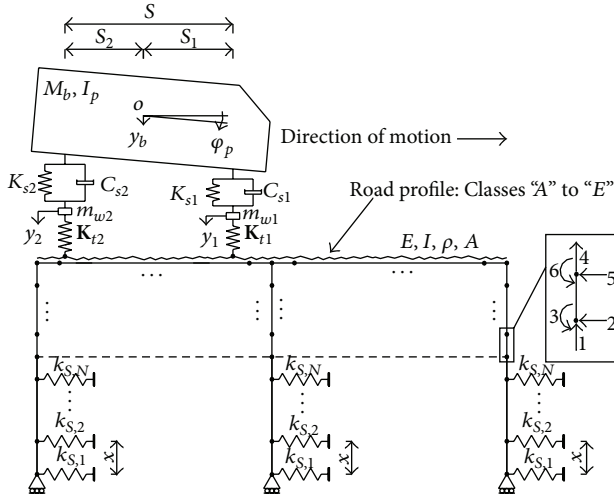


FIGURE 5: Continuum model of half car crossing an integral bridge (not to scale).

the effective moment of inertia of the pile group (m^4). The effective diameter of the pile group is obtained by summing the diameters of the individual piles in the group and the effective moment of inertia of the pile group is obtained in the same way. Individual soil stiffness coefficients ($k_{s,i}$) are calculated by multiplying K value at a given spring depth by the spacing between springs at that depth.

An example of converting G_0 data from Figure 4(b) into a profile of the modulus of subgrade reaction (K) is shown in Figure 4(c) and hence that into individual spring coefficients ($k_{s,i}$) is shown in Figure 4(d). In this figure, the effective diameter of the pile group is taken as 6 m (8 piles \times 0.75 m diameter each) and the pile material is assumed to be concrete.

2.4. Vehicle Model and Interaction

2.4.1. Overview of Vehicle-Bridge Interaction (VBI) Problem.

Having developed a finite element model of bridge-soil interaction the next step toward implementing a Vehicle-Bridge-Soil Dynamic Interaction (VBSDI) model is to model how the vehicle applies loading to the bridge as it passes over it. The important point to note is that as a vehicle passes over a bridge the loading it applies to the bridge is not constant as it is affected by the road profile (surface roughness), the speed of the vehicle, and the properties of the vehicle.

The fundamental challenge with vehicle-bridge interaction modelling is that the movement of the bridge influences movements of the vehicle, which in turn influence movements of the bridge. When studying vehicle-bridge interaction problems two sets of equations can be written: one set for the vehicle and one set for the bridge. To satisfy compatibility the contact forces in both subsystems must be the same and it is these contact forces that make the two sets of equations coupled. Yang et al. [23] give an overview of the problem as well as a description of some commonly used techniques such as the iterative method, the dynamic condensation method, and Yang's VBI element. Each of the

TABLE 1: Typical parameters for truck model.

Dimensional data		
Dimensions (m)	Wheel base (S)	5.5
	Dist. from centre of mass to front axle (S_1)	3.66
	Dist. from centre of mass to rear axle (S_2)	1.84
Mass and inertia		
Mass (kg)	Front wheel/axle mass (m_{w1})	700
	Rear wheel/axle mass (m_{w2})	1,100
	Sprung body mass (m_b)	13,300
Inertia (kg m^2)	Pitch moment of inertia of truck (I_p)	41,008
Suspension		
Spring stiffness (kN m^{-1})	Front axle (K_{s1})	400
	Rear axle (K_{s2})	1,000
Damping (kN s m^{-1})	Front axle (C_{s1})	10
	Rear axle (C_{s2})	10
Tyre stiffness (kN m^{-1})	Front axle (K_{t1})	1,750
	Rear axle (K_{t2})	3,500

methods has certain advantages and disadvantages; however, for the purposes of this study the iterative approach was suitable. Iterative techniques have been used by Green and Cebon [33] and Yang and Fonder [34] and are described in more detail in Section 2.4.4.

Before describing how vehicle-bridge interaction is implemented it is first useful to look at the bridge-vehicle model; see Figure 5. In this arrangement the vehicle has 4 degrees of freedom: the pitch of the sprung body mass $\varphi_p(t)$, the displacement of the sprung body mass $y_b(t)$, the displacement of unsprung mass 1 $y_1(t)$, and the displacement of unsprung mass 2 $y_2(t)$. Unsprung masses 1 and 2 represent the masses of the front and rear axle assembly.

2.4.2. Vehicle Properties.

In this study the vehicle modelled is a two-axle truck. The geometry of the test truck can be tailored by the user to represent any type of two-axle truck; that is, the sprung body mass, axle spacing, unsprung axle mass, suspension damping and stiffness, and so forth can all be modified by the user. Harris et al. [35] give the typical suspension and tyre properties for this kind of vehicle and Table 1 gives a summary of the vehicle properties that were used in this study.

2.4.3. Generating a Road Profile.

The road profile is simply an array of numbers that defines the height of the road surface at discrete intervals along the length of the bridge (e.g., every 1 cm). The length of road profile necessary depends on the span of the bridge, the wheel base of the vehicle, and the desired approach distance. The purpose of modelling the movement of the vehicle as it approaches the bridge is to allow it to reach a steady state of vibration before it reaches the bridge, thereby making its subsequent interaction with the bridge more realistic. A typical approach length used is of the order of 100 m. Cebon [36] describes how the topography of a given road profile can be classified in accordance with the

ISO standard; for example, a road profile can be classified as “very good,” “good,” “average,” “poor,” or “very poor.” Cebon also describes how an artificial road surface topography of a given roughness/classification can be generated for use in time-domain vehicle vibration simulations. While the road profile generator defines the height of equally spaced points along the road (e.g., spatially distributed every 1 cm), it is inappropriate to use these heights directly in the model. The reason for this is that the wheel of the truck is not supported by just one road profile ordinate. Typical truck tyres span approximately 24 cm; therefore the wheel rests upon 24 road profile ordinates simultaneously (for ordinates spaced at 1 cm intervals). To take account of this fact the road profile used in the model is obtained by applying a moving average filter to the road profile given by the road profile generator to obtain the average ordinate height over the span of the wheel. Finally it is necessary to extract from the global road profile the road profile experienced by the front axle on the approach section $r_{1A}(t)$ and on the bridge section $r_1(t)$ and to do the same for the rear axle. (The road profile is generated spatially; however for simulation purposes the important thing to know is the height of the road profile ordinate under each axle at each time step.) It is also important to note that the purpose behind incorporating a road profile in the model is to afford a more realistic treatment of the vehicle-bridge interaction problem and to allow researchers to test the resilience of emerging SHM techniques under a variety of conditions. Road profiles are generated randomly according to the specified road profile classification and it is not intended to model the road profile of a specific bridge. Figure 6 shows example road profiles generated for a 50 m long bridge span. The road surface roughness is varied from Class “A” (very good) to Class “E” (very poor) for the purpose of illustration.

2.4.4. Iterative VBI Procedure. By using the equations of Fryba [37] it is possible to develop a stiffness $[\mathbf{K}_v]$, mass $[\mathbf{M}_v]$, and damping $[\mathbf{C}_v]$ matrix for the vehicle. The dynamic response of the vehicle is modelled as shown in

$$[\mathbf{M}_v] \begin{Bmatrix} \ddot{\varphi}_p(t) \\ \ddot{y}_b(t) \\ \ddot{y}_1(t) \\ \ddot{y}_2(t) \end{Bmatrix} + [\mathbf{C}_v] \begin{Bmatrix} \dot{\varphi}_p(t) \\ \dot{y}_b(t) \\ \dot{y}_1(t) \\ \dot{y}_2(t) \end{Bmatrix} + [\mathbf{K}_v] \begin{Bmatrix} \varphi_p(t) \\ y_b(t) \\ y_1(t) \\ y_2(t) \end{Bmatrix} = \{\mathbf{F}_v\}, \quad (7)$$

where \mathbf{F}_v is the vector of forces acting on the vehicle degrees of freedom for a given time step. In the first instance, the vehicle is run across the bridge assuming the bridge does not experience any deflection. The displacement of each vehicle axle, $y_1(t)$ and $y_2(t)$, is then obtained using the Wilson- θ method applied to (7) and the contact forces between the vehicle and the road surface for each time step are calculated in

$$\begin{Bmatrix} \mathbf{F}_1(t) \\ \mathbf{F}_2(t) \end{Bmatrix} = \begin{bmatrix} \mathbf{K}_{t1} & \mathbf{0} \\ \mathbf{0} & \mathbf{K}_{t2} \end{bmatrix} \begin{Bmatrix} y_1(t) \\ y_2(t) \end{Bmatrix}, \quad (8)$$

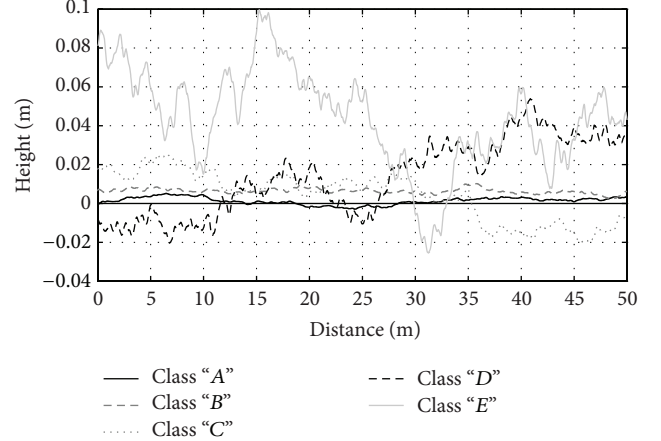


FIGURE 6: Example road profiles: Class “A” to Class “E” for a 50 m long bridge.

where \mathbf{K}_{t1} and \mathbf{K}_{t2} are the front and rear tyre stiffness, respectively. The contact forces obtained in (8) can then be applied to the FE model of the bridge. This is achieved by defining $\mathbf{F}(t)$ in (1) using Hermitian shape functions to apportion the axle loads $\mathbf{F}_1(t)$ and $\mathbf{F}_2(t)$ to the bridge nodes since the position of the loads $\mathbf{x}(t)$ at every time step is known. Once $\mathbf{F}(t)$ has been populated the Wilson- θ method is used to calculate the displacement of each of the bridge degrees of freedom at each time step. Since the first run of the vehicle assumed no bridge displacement, the process must be iterated to take account of the bridge displacement changing the height of the road profile experienced by each axle at each time step. The latest road profile affects the contact forces, which in turn affect the bridge displacement, which affects the road profile and so forth. The road profile is continually updated by subtracting the bridge displacements until convergence is achieved. Guidance on convergence for simulations of this type is given in [33]. Convergence in this study is deemed to have occurred when the maximum difference in displacement (for all degrees of freedom) between the current time step and the previous time step is less than 1% of the max displacement of the bridge; see

$$\left| \frac{\Delta_i - \Delta_{i-1}}{\Delta_{\max}} \right| \leq 0.01. \quad (9)$$

3. Modelling Algorithms

3.1. Scour Modelling. In this section, the output of signals of interest from the system and the postprocessing required to make them “analysis ready” is discussed. As mentioned in previous sections, the model is capable of outputting dynamic displacement, velocity, and acceleration signals from a multitude of points on the bridge structure. Moreover, the model is also capable of outputting dynamic displacement, velocity, and acceleration signals from the vehicle model as it traverses the bridge. Using the signals arising on the bridge structure itself allows the user to test *direct* SHM techniques, that is, methods that rely on sensors being placed on the actual

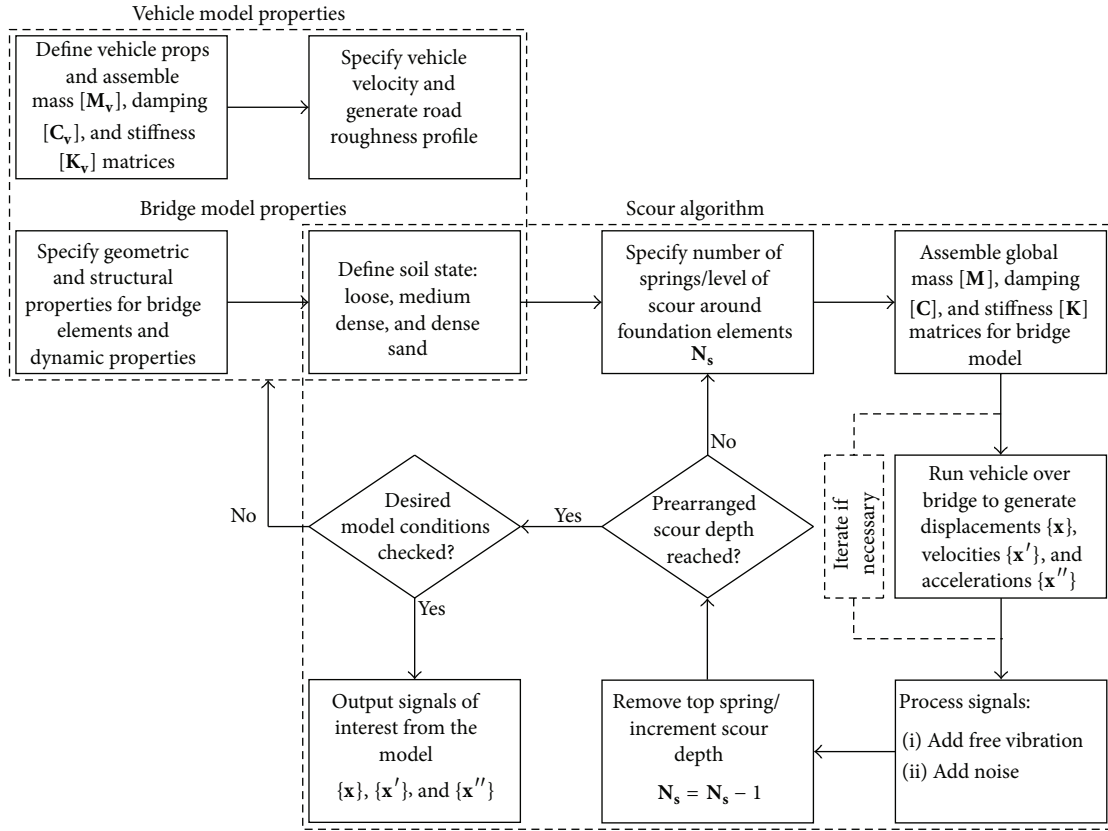


FIGURE 7: Scour modelling algorithm to generate analysis signals.

structure to detect damage features. Using the signals arising on the vehicle system allows the user to test *indirect* methods of damage detection, which use sensors placed on the vehicle (i.e., axles, body) to detect damage on the bridge as it traverses. The generic algorithm to generate signals of interest from the bridge is shown in the flow diagram in Figure 7. In order to create usable signals for analysis, it is often necessary to simulate damped free vibration of the bridge after the vehicle has departed the structure (this is because high vehicle speeds can result in very short signals which is often problematic from a signal processing point of view). The model also has the facility to add “measurement noise” that would be present in real signals. This is discussed in Section 3.2. Scour is modelled as the removal of springs from around the foundation element of interest (pier, abutments) starting with the spring nearest the top.

3.2. Adding Noise to Numerical Signals. Signals recorded on a real structure will contain measurement noise; therefore for the purpose of a fair assessment of a given SHM algorithm, the presence of noise in the numerically generated signals should be accounted for. The model developed in this paper allows for two different methods to add noise to the “clean” numerical signals. The first method is based on Zhu and Law [10] and the second method is based on Lyons [38]. The Zhu and Law approach allows the user to specify

a percentage noise level to be added to the signal of interest and is formulated as follows:

$$\text{sig}_{\text{NOISE}} = \text{sig}_{\text{CLEAN}} + E_p N_{\text{NOISE}} \sigma(\text{sig}_{\text{CLEAN}}), \quad (10)$$

where $\text{sig}_{\text{NOISE}}$ is the noisy (corrupted) signal, E_p is the percentage of added noise, N_{NOISE} is a standard normal distribution vector with zero mean value and unit standard deviation, $\text{sig}_{\text{CLEAN}}$ is the calculated signal from the model, and $\sigma(\text{sig}_{\text{CLEAN}})$ is the standard deviation. Specifying E_p values of 0.01 to 0.05 adds 1% to 5% of noise, respectively, to the clean signal, for example.

The second method used to add noise is based on the signal-to-noise ratio (SNR), given in [38]

$$\text{SNR} = 10 \log_{10} \frac{\text{Signal Power}}{\text{Noise Power}}, \quad (11)$$

where SNR is the ratio of the strength of a signal carrying information equating to that of unwanted interference. This equation can be rearranged to give

$$\sigma_N = \sqrt{\text{Noise Power}} = \sqrt{\frac{\text{Signal Power}}{\exp((\text{SNR} \cdot \log_e(10))/10)}}, \quad (12)$$

where σ_N is the variance of the noise. Using (12), noise signals with different signal-to-noise ratios can be added to

TABLE 2: Case study bridge properties.

Bridge deck			
Young's modulus (E) (MPa)	35000	X-sectional area (m^2)	9.516
Moment of inertia (m^4)	2.9487	Concrete density ($kg\ m^{-3}$)	2400
Spans	2	Span length (m)	25
Bridge abutment columns			
Young's modulus (E) (MPa)	35000	Total X-sectional area (m^2)	1.7671
Total moment of inertia (m^4)	0.0276	Concrete density ($kg\ m^{-3}$)	2400
Number of columns	9	Column length (m)	6
Bridge pier			
Young's modulus (E) (MPa)	35000	Total X-sectional area (m^2)	7.22
Total moment of inertia (m^4)	1.137	Concrete density ($kg\ m^{-3}$)	2400
Number of columns	2	Column length (m)	6
Abutment piles			
Young's modulus (E) (MPa)	35000	Total X-sectional area (m^2)	2.827
Total moment of inertia (m^4)	0.0636	Concrete density ($kg\ m^{-3}$)	2400
Number of piles	10	Pile length (m)	15
Pier piles			
Young's modulus (E) (MPa)	35000	Total X-sectional area (m^2)	3.534
Total moment of inertia (m^4)	0.1243	Concrete density ($kg\ m^{-3}$)	2400
Number of piles	8	Pile length (m)	15

the original “clean” signal obtained directly from the numerical model. This process is shown in

$$\text{Sig}_{\text{NOISE}} = \sigma_N [\text{rand}] + \text{Sig}_{\text{CLEAN}}. \quad (13)$$

The addition of noise to the signals allows for a more robust testing of a given SHM scheme as, in general, measurement noise can inhibit the accuracy of a given SHM scheme.

4. Example Signals from Developed Model

In this section, some example signals simulated by the model and their response features are shown. Section 4.1 displays some typical bridge signals and Section 4.2 displays some vehicle signals calculated when the vehicle is crossing the bridge. The case study bridge modelled is a two-span integral bridge with flexible abutments; each span is 25 m in length (Figure 2 shows a 3D schematic of the bridge). The bridge deck is formed using nine U10 bridge beams [39] supporting a 200 mm thick deck slab. The bridge abutments are formulated with nine concrete columns supporting the bridge beams, each column 500 mm in diameter, and spaced at 1900 mm centres. Two stiff piers support the deck at the centre and have plan dimensions of 1375 mm \times 2625 mm. The abutment columns rest on a pile cap under which ten, 15 m long (0.6 m diameter) bored concrete piles are placed. A loose sand soil profile is generated as per the analysis in Section 2.3.2. For the purpose of modelling, scour around an individual foundation element is assumed to be uniform along the transverse length of a given support. As mentioned previously, the model is idealised as a 2D frame with group properties adopted for the various structural members. The structural properties shown in Table 2 are used for the simulations presented in this section.

4.1. Bridge Signals. Some typical response signals from the bridge due to the vehicle crossing are shown in Figure 8. For this analysis, the vehicle (properties shown in Table 1) traverses the bridge at 50 km hr⁻¹ over a Class “A” road surface (shown in Figure 6) and a zero scour condition is assumed. Ten seconds of free vibration is also calculated and the analysis assumes damped vibration at 2%. The three plots on the left side of the figure (i.e., (a), (c), and (e)) show the vertical displacement, velocity, and acceleration of the midpoint of the left span (span 1) of the bridge resulting from the passage of the vehicle across the bridge. The displacement response in part (a) of the figure is dominated by the static bridge response. When the truck is on span 1, the span deflects downwards, and while there are some dynamic movements evident their amplitude is small relative to the static displacement. As the truck passes onto span 2 the mid-span of span 1 deflects upwards slightly. Once the truck leaves the bridge at time, $t = 4$ seconds, the deck goes into free vibration, but the amplitudes of the displacements are very small relative to the static displacement. Figure 8(c) shows the corresponding vertical velocity response at the mid-span of span 1. While the static movements are still evident in the velocity signal the dynamic movements are much clearer. Figure 8(e) shows the vertical acceleration response of the mid-span of span 1. This time the dynamic movements of the bridge dominate the signal and high amplitude localised peaks are visible in the acceleration signal as the front and rear axles enter/leave the bridge. The logarithmic decay of the acceleration signal when the bridge goes into free vibration is also evident in part (e) of the figure. The three plots on the right side of the figure (i.e., (b), (d), and (f)) show the horizontal displacement, velocity, and acceleration of the top of the pier resulting from the passage of the vehicle across

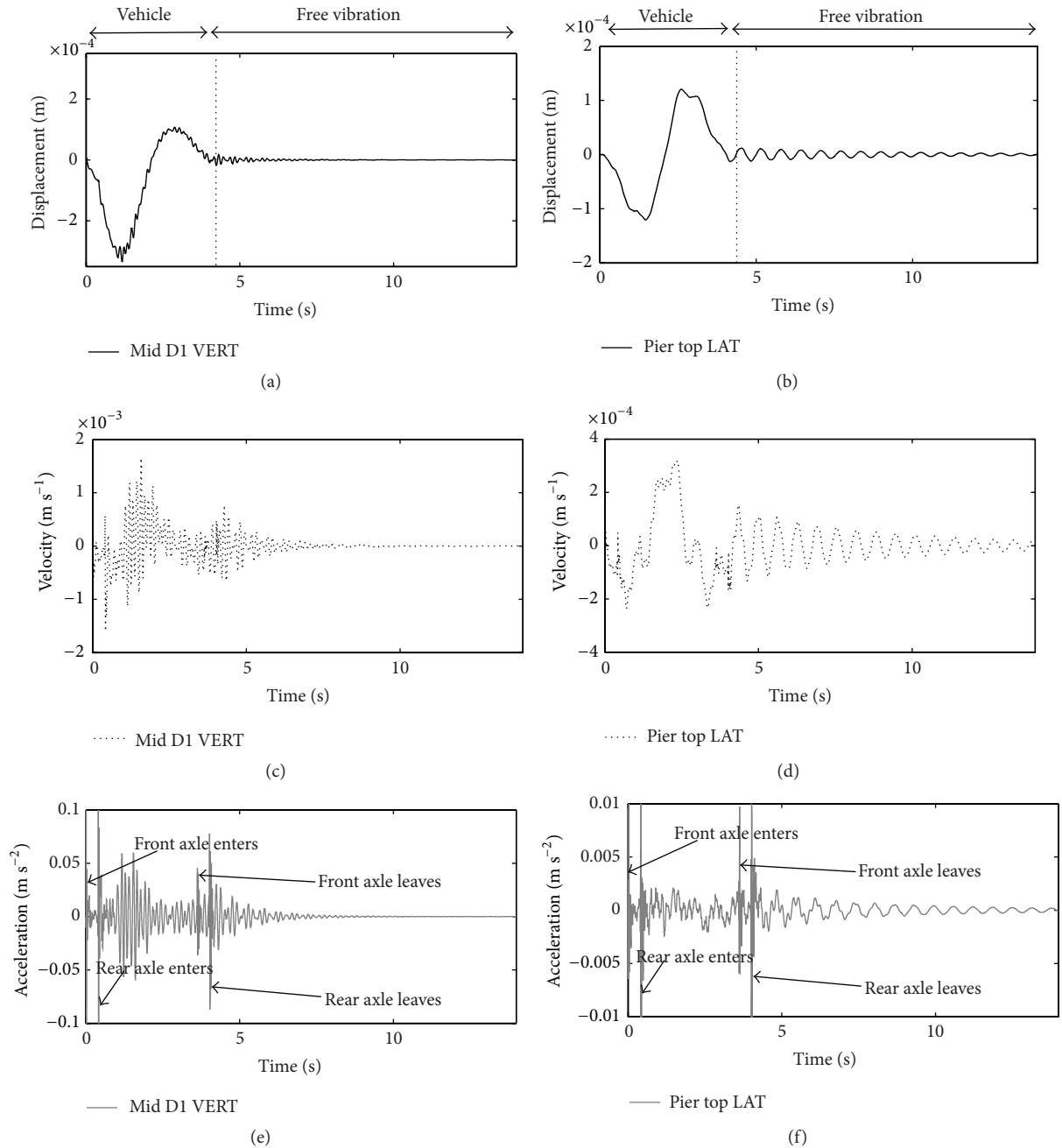


FIGURE 8: Example signals from model for vehicle traversing at 50 km hr^{-1} with 10 seconds of free vibration and a Class “A” road profile. (a) Vertical displacement response at mid-span of span 1; (b) horizontal displacement at top of pier; (c) vertical velocity response at mid-span of span 1; (d) horizontal velocity at top of pier; (e) vertical acceleration response at mid-span of span 1; (f) horizontal acceleration at top of pier. All signals are damped at 2%.

the bridge. When the vehicle is on span 1 the head of the pier moves to the left (negative displacement) and when the vehicle is on span 2 the head of the pier moves to the right (positive displacement). Although there is little dynamic movement evident when the vehicle is on the bridge, once the bridge goes into free vibration the dynamic movements are clearly evident. The horizontal velocity signal shown in part (d) of the figure shows a clear dynamic component, and the frequency is noticeably lower than the frequency

evident in the plot of vertical mid-span velocity (Figure 8(c)). Figure 8(f) shows the horizontal acceleration response at the top of the pier and again the peaks due to the axles entering/leaving the bridge are evident.

For the purpose of scour detection, the lateral bridge response is often the response of most interest, in that this is the response typically affected by scour in bridges of this type [16, 40]. Therefore it is of interest to examine the parameters that affect the ability for a vehicle traversing the bridge to

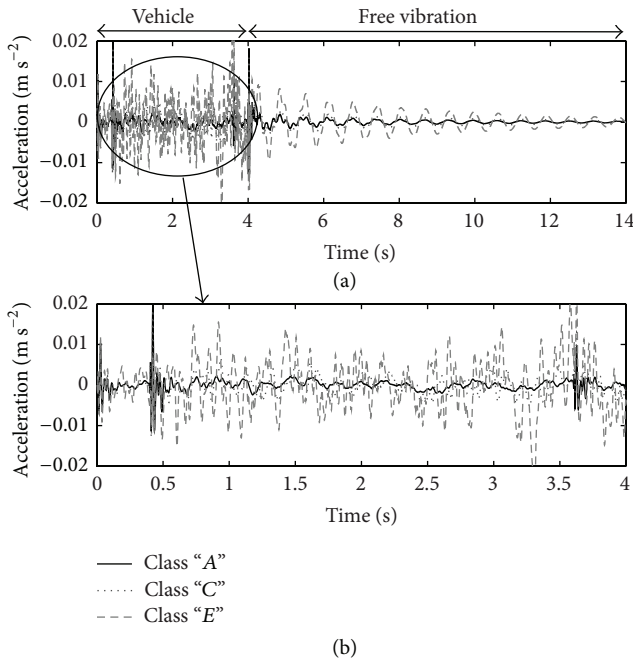


FIGURE 9: Effect of road surface roughness on lateral pier top acceleration response, (a) forced and free vibration for Classes A, C, and E and (b) forced vibration only.

excite the lateral response of the structure. Figures 8(b), 8(d), and 8(e) show the lateral displacement, velocity, and acceleration response of the pier top due to the passage of a vehicle over a Class "A" road surface. The effect of increased road surface roughness on the lateral pier top acceleration is examined in Figure 9. The vehicle traverses the bridge at 50 km hr^{-1} and 10 seconds of free vibration (damped at 2%) is assumed after the vehicle leaves the bridge.

Figure 9 shows the effect of increasing road surface roughness from A to C to E on the resulting lateral acceleration response at the pier top (see Figure 6 for road profiles). The effect of increasing the surface roughness leads to higher magnitude acceleration responses for both the forced and free vibration components of the response signal. As the forced vibration component is difficult to see in Figure 9(a), part (b) shows only the forced component of the signal.

The effect of scour on the lateral acceleration response of the pier top is examined in Figure 10, whereby 5 m of scour is induced around the central pier foundation. For this analysis, the vehicle once again traverses the bridge at 50 km hr^{-1} over a Class "A" road surface with 10 seconds of subsequent free vibration.

Figure 10 shows the effect of 5 m of pier scour on the lateral acceleration response measured at the pier top due to the passing vehicle at 50 km hr^{-1} . In this figure, the period of the signal has increased with scour (see the insert showing a zoomed-in portion of the signal between 4.5 and 7 seconds). This is sensible as the effect of scour is to increase the effective length of the pier thus making it more flexible so an increased period is expected. The amplitude of the scoured signal has reduced in the free vibration. The reason for this is twofold. (i) The effect of scour reducing the confining stiffness effect

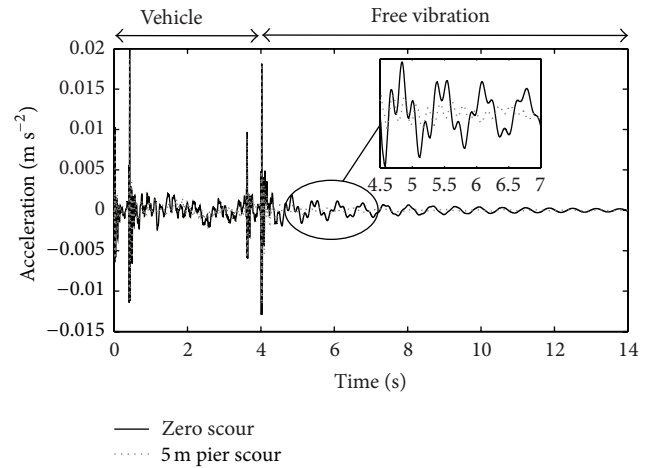


FIGURE 10: Difference in lateral pier top acceleration for 0 and 5 m scour.

of the soil leads to higher lateral translation of the pier at lower depths, meaning the pier top translation is lessened. This manifests itself as a lower pier top dynamic displacement and acceleration for increased pier scour. (ii) Interaction effects between the bridge's natural oscillation period and the velocity of the vehicle lead to differences in the free vibration amplitude depending on where the vehicle is on the bridge at a given time increment relative to the (lateral) oscillation state of the bridge itself. The location of the vehicle at a certain time means it can either increase or diminish the bridge's natural oscillatory response.

In terms of damage detection using vibrations, many SHM algorithms can be sensitive to the presence of measurement noise as well as other external disturbances. Figure 11 shows the effect of artificially adding noise to the simulated acceleration signals. For this analysis, the process outlined in (11)–(13) is used whereby noise is added by utilising the signal-to-noise ratio (SNR) as per [38]. Once again, this analysis is for a vehicle traversing at 50 km hr^{-1} , a Class "A" road profile, loose sand profile, 10 seconds of free vibration, zero scour, and the lateral acceleration generated at the pier top. SNRs of 20, 10, and 5 are used to show the increasing effect of noise on the time-domain acceleration signals.

Figure 11 shows the effect of increasing the noise level present in the lateral acceleration response at the top of the bridge pier. In Figure 11(a) the characteristics of the signal are easily discernible and the individual oscillations in the free vibration can be seen clearly. On the contrary, in Figure 11(d) with a $\text{SNR} = 5$, the individual oscillations are difficult to identify and it is clear that the addition of noise has significantly reduced the clarity of the signal. The addition of noise to the signals allows researchers to test the resilience of emerging SHM algorithms under increasingly challenging conditions that might be experienced in the field.

4.2. Vehicle Signals. In this section, some typical vehicle response signals are shown. The purpose of using vehicle signals as mentioned previously is to allow researchers to test indirect methods of SHM, whereby the response of the

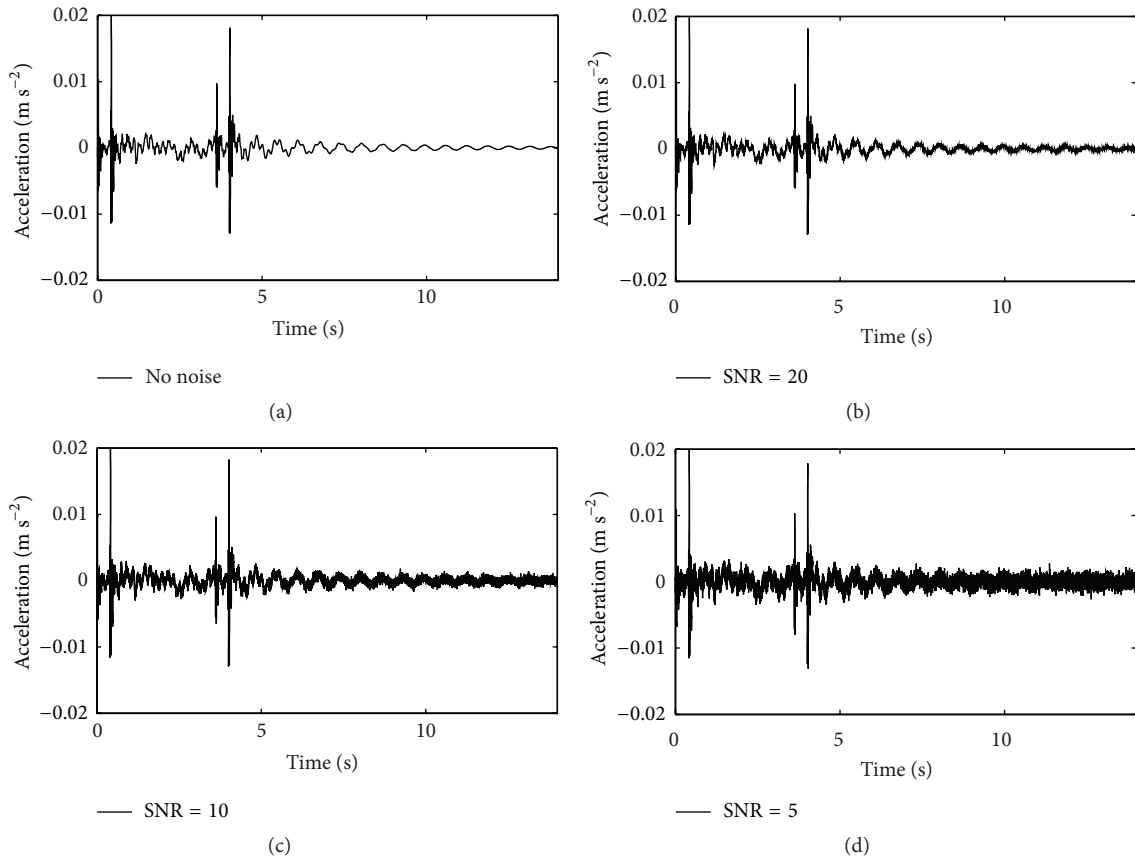


FIGURE 11: Effect of noise on lateral pier acceleration response. (a) Noise-free signal; (b) signal with SNR = 20; (c) signal with SNR = 10; (d) signal with SNR = 5.

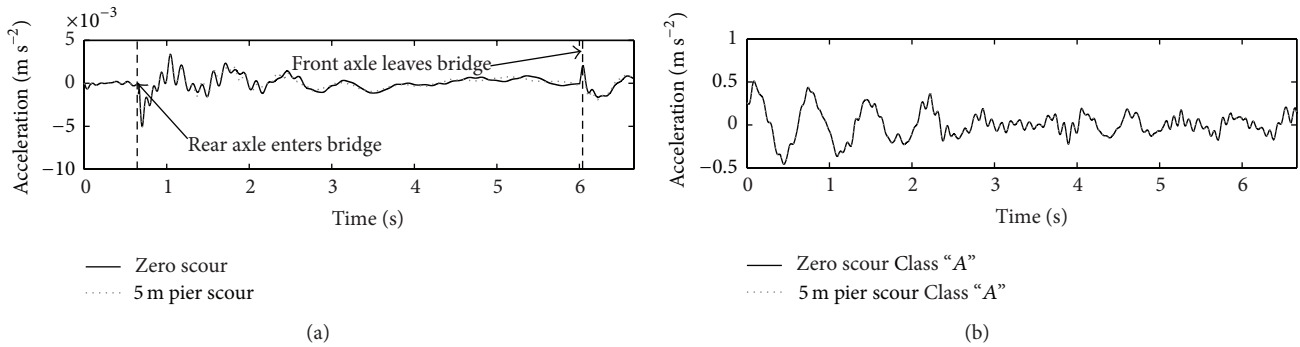


FIGURE 12: Effect of road roughness on vehicle body accelerations. (a) Vertical body acceleration over smooth road surface for zero and 5 m scour, (b) vertical body acceleration over Class “A” road surface for zero and 5 m scour.

vehicle is used to infer the damage condition of the bridge. For example, a number of authors have inferred the condition of the bridge deck by analysing the vehicle response as it crossed the bridge [41, 42]. The vehicle response is sensitive to the road profile; therefore in this section the effect of road surface roughness is examined in terms of detecting the presence of scour. Figure 12 shows the vertical acceleration response of the vehicle body as it traverses a bridge at 30 km hr^{-1} for zero and 5 m of pier scour. To make the simulation as realistic as possible the vehicle commences motion at an approach

distance of 100 m from the start of the bridge; however, here only the portion of the response when the vehicle is on the bridge is shown. A loose sand profile is adopted in the bridge model and the vehicle traverses a smooth road surface in Figure 12(a) and a Class “A” road surface in Figure 12(b) (see Figure 6 for road profile).

Figure 12 shows the effect of the road surface roughness on the clarity of the vertical acceleration response detected on the vehicle body as it traverses the bridge at 30 km hr^{-1} . Figure 12(a) shows the difference in vehicle body vertical

acceleration for zero and 5 m pier scour as it traverses a smooth road surface. Figure 12(b) shows that the difference between zero scour and 5 m pier scour vertical vehicle body accelerations is difficult to observe in the presence of a Class “A” road surface. The presence of a road profile may cause difficulty with some SHM schemes aiming to use vehicle measurements to detect damage/scour.

5. Conclusion

In this paper, the development of a novel Vehicle-Bridge-Soil Dynamic Interaction (VBSDI) model for modelling the effect of scour around integral bridge foundations is presented. The model is capable of rapidly modelling the scour response of integral bridges and incorporates realistic (validated) representations of the foundation soil stiffness as well as a realistic vehicle loading model. This paper discusses the mathematical theory and assumptions underlying the model. The model is capable of outputting dynamic displacements, velocities, and accelerations from any point on the bridge as well as on the vehicle with a view to allowing researchers to test emerging structural health monitoring techniques. Signals from the bridge can be used to test direct methods of health monitoring, whereby sensors are placed on the actual bridge structure. Signals measured on the vehicle as it traverses the bridge can also be used to test indirect methods of health monitoring, which rely on the bridge’s damage feature being detected in the vehicle response. The model can vary the soil conditions from loose sand to dense sand and vary the road surface roughness from Class “A” (very good) to Class “E” (very poor). The effects of measurement noise can also be incorporated using two separate methods to afford a more rigorous assessment of a particular SHM technique aiming to use real (noisy) signals. Finally, some typical response data from both a bridge and a two-axle vehicle are presented by way of a case study.

The model developed in this paper is intended to aid researchers working in the area of scour detection using vibration-based methods to test emerging algorithms that they may have in development. While every effort has been made to ensure the signals from the model are as realistic as possible, it is recommended where possible to test developed techniques on actual structures. The current model aims to serve as a preliminary tool for researchers to test their techniques under a range of modelling scenarios prior to field deployment.

Conflict of Interests

The authors declare that there is no conflict of interests regarding the publication of this paper.

Acknowledgments

The authors would like to acknowledge the support of the Earth and Natural Sciences (ENS) Doctoral Studies Programme, funded by the Higher Education Authority (HEA) through the Programme for Research at Third Level Institutions, Cycle 5 (PRTL-5), cofunded by the European

Regional Development Fund (ERDF), the European Union Framework 7 Project SMART RAIL (Project no. 285683), and the University College Dublin (UCD) Earth Institute.

References

- [1] C. R. Farrar and K. Worden, “An introduction to structural health monitoring,” *Philosophical Transactions. Series A, Mathematical, Physical, and Engineering Sciences*, vol. 365, no. 1851, pp. 303–315, 2007.
- [2] A. D. Dimarogonas, “Vibration of cracked structures: a state of the art review,” *Engineering Fracture Mechanics*, vol. 55, no. 5, pp. 831–857, 1996.
- [3] E. A. Johnson, H. F. Lam, L. S. Katafygiotis, and J. L. Beck, “Phase I IASC-ASCE structural health monitoring benchmark problem using simulated data,” *Journal of Engineering Mechanics*, vol. 130, no. 1, pp. 3–15, 2004.
- [4] S. Dyke, D. Bernal, J. Beck, and C. Ventura, “Experimental phase II of the structural health monitoring benchmark problem,” in *Proceedings of the 16th ASCE Engineering Mechanics Conference*, Seattle, Wash, USA, July 2003, http://authors.library.caltech.edu/34226/1/Report_bldg-shm_exp2.pdf.
- [5] S. Foti and D. Sabia, “Influence of foundation scour on the dynamic response of an existing bridge,” *Journal of Bridge Engineering*, vol. 16, no. 2, pp. 295–304, 2011.
- [6] W. Ostachowicz and M. Krawczak, “On modelling of structural stiffness loss due to damage,” in *Proceedings of the 4th International Conference Damage Assessment of Structures (DAMAS '01)*, Cardiff, UK, 2001.
- [7] M. I. Friswell and J. E. T. Penny, “Crack modeling for structural health monitoring,” *Structural Health Monitoring*, vol. 1, no. 2, pp. 139–148, 2002.
- [8] C. P. Ratcliffe, “Damage detection using a modified laplacian operator on mode shape data,” *Journal of Sound and Vibration*, vol. 204, no. 3, pp. 505–517, 1997.
- [9] M. A. Mahmoud, “Effect of cracks on the dynamic response of a simple beam subject to a moving load,” *Proceedings of the Institution of Mechanical Engineers, Part F: Journal of Rail and Rapid Transit*, vol. 215, no. 3, pp. 207–215, 2001.
- [10] X. Q. Zhu and S. S. Law, “Wavelet-based crack identification of bridge beam from operational deflection time history,” *International Journal of Solids and Structures*, vol. 43, no. 7-8, pp. 2299–2317, 2006.
- [11] D. Hester and A. González, “A wavelet-based damage detection algorithm based on bridge acceleration response to a vehicle,” *Mechanical Systems and Signal Processing*, vol. 28, pp. 145–166, 2012.
- [12] A. González, E. J. O'Brien, and P. J. McGetrick, “Identification of damping in a bridge using a moving instrumented vehicle,” *Journal of Sound and Vibration*, vol. 331, no. 18, pp. 4115–4131, 2012.
- [13] L. J. Prendergast and K. Gavin, “A review of bridge scour monitoring techniques,” *Journal of Rock Mechanics and Geotechnical Engineering*, vol. 6, no. 2, pp. 138–149, 2014.
- [14] S. H. Ju, “Determination of scoured bridge natural frequencies with soil-structure interaction,” *Soil Dynamics and Earthquake Engineering*, vol. 55, pp. 247–254, 2013.
- [15] C.-C. Chen, W.-H. Wu, F. Shih, and S.-W. Wang, “Scour evaluation for foundation of a cable-stayed bridge based on ambient vibration measurements of superstructure,” *NDT & E International*, vol. 66, pp. 16–27, 2014.

- [16] J. V. Klinga and A. Alipour, "Assessment of structural integrity of bridges under extreme scour conditions," *Engineering Structures*, vol. 82, pp. 55–71, 2015.
- [17] L. J. Prendergast, D. Hester, K. Gavin, and J. J. O'Sullivan, "An investigation of the changes in the natural frequency of a pile affected by scour," *Journal of Sound and Vibration*, vol. 332, no. 25, pp. 6685–6702, 2013.
- [18] S. Donohue, M. Long, K. Gavin, and P. O'Connor, "Shear wave stiffness of Irish glacial till," in *Proceedings of the 2nd International Conference on Site Characterization*, pp. 459–466, Porto, Portugal, 2004.
- [19] L. J. Prendergast, K. Gavin, and P. Doherty, "An investigation into the effect of scour on the natural frequency of an offshore wind turbine," *Ocean Engineering*, vol. 101, pp. 1–11, 2015.
- [20] S. M. Springman, A. R. M. Norrish, and C. W. W. Ng, "Cyclic loading of sand behind integral bridge abutments," TRL Report 146, Transport Research Laboratory, Wokingham, UK, 1996.
- [21] Steel Construction Institute, "Integral bridges," 2015, http://www.steelconstruction.info/Integral_bridges#References.
- [22] Y. W. Kwon and H. Bang, *The Finite Element Method using MATLAB*, CRC Mechanical Engineering Series, CRC Press, Boca Raton, Fla, USA, 2nd edition, 2000.
- [23] Y. Yang, J. Yau, and Y. Wu, *Vehicle-Bridge Interaction Dynamics*, World Scientific, 2004, http://www.worldscientific.com/doi/pdf/10.1142/9789812567178_fmatter.
- [24] J. W. Tedesco, W. G. McDougal, and C. Allen Ross, *Structural Dynamics: Theory and Applications*, Addison Wesley Longman, 1999.
- [25] E. Winkler, *Theory of Elasticity and Strength*, Dominicus, Prague, Czech Republic, 1867.
- [26] S. C. Dutta and R. Roy, "A critical review on idealization and modeling for interaction among soil–foundation–structure system," *Computers and Structures*, vol. 80, no. 20-21, pp. 1579–1594, 2002.
- [27] T. Lunne and H. P. Christoffersen, "Interpretation of cone penetrometer data for offshore sands," in *Proceedings of the Offshore Technology Conference*, Houston, Tex, USA, 1983.
- [28] API, "Recommended practice for planning, designing and constructing offshore platforms—working stress design," API RP2A, American Petroleum Institute, Washington, DC, USA, 2007.
- [29] Fugro, "Guide for estimating soil type and characteristics using cone penetration testing," Cone Penetration Tests, 2011, <http://www.fes.co.uk/downloads/CPT-general.pdf>.
- [30] R. J. Jardine, F. C. Chow, R. F. Overly, and J. Standing, *ICP Design Methods for Driven Piles in Sands and Clays*, Thomas Telford Publishing, London, UK, 2005.
- [31] G. Baldi, R. Belottini, V. N. Ghionna, N. I. Jamiokowski, and D. C. F. Lo Presti, "Modulus of sands from CPTs and DMTs," in *Proceedings of the 12th International Conference on Soil Mechanics and Foundation Engineering (ICSMFE '89)*, vol. 1, pp. 165–170, Rio de Janeiro, Brazil, August 1989.
- [32] S. A. Ashford and T. Juirnarongrit, "Evaluation of pile diameter effect on initial modulus of subgrade reaction," *Journal of Geotechnical and Geoenvironmental Engineering*, vol. 129, no. 3, pp. 234–242, 2003.
- [33] M. F. Green and D. Cebon, "Dynamic interaction between heavy vehicles and highway bridges," *Computers and Structures*, vol. 62, no. 2, pp. 253–264, 1997.
- [34] F. Yang and G. Fonder, "An iterative solution method for dynamic response of bridge–vehicles systems," *Earthquake Engineering & Structural Dynamics*, vol. 25, no. 2, pp. 195–215, 1996.
- [35] N. K. Harris, E. J. O'Brien, and A. González, "Reduction of bridge dynamic amplification through adjustment of vehicle suspension damping," *Journal of Sound and Vibration*, vol. 302, no. 3, pp. 471–485, 2007.
- [36] D. Cebon, *Handbook of Vehicle-Road Interaction*, Swets & Zeitlinger, Lisse, The Netherlands, 1999.
- [37] L. Fryba, *Vibration of Solids and Structures Under Moving Loads*, Thomas Telford, London, UK, 1999.
- [38] R. Lyons, *Understanding Digital Signal Processing*, Prentice Hall, Boston, Mass, USA, 3rd edition, 2011.
- [39] Concast, Civil Engineering Solutions, Civil Engineering Solutions, 2014, http://www.concastprecast.co.uk/images/uploads/brochures/Concast_Civil.pdf.
- [40] A. Elsaid, *Vibration based damage detection of scour in coastal bridges [Ph.D. thesis]*, North Carolina State University, Raleigh, NC, USA, 2012.
- [41] J. Keenahan, E. J. O'Brien, P. J. McGetrick, and A. Gonzalez, "The use of a dynamic truck-trailer drive-by system to monitor bridge damping," *Structural Health Monitoring*, vol. 13, no. 2, pp. 143–157, 2014.
- [42] A. Malekjafarian and E. J. O'Brien, "Identification of bridge mode shapes using short time frequency domain decomposition of the responses measured in a passing vehicle," *Engineering Structures*, vol. 81, pp. 386–397, 2014.

Research Article

Undecimated Lifting Wavelet Packet Transform with Boundary Treatment for Machinery Incipient Fault Diagnosis

Lixiang Duan,¹ Yangshen Wang,¹ Jinjiang Wang,¹ Laibin Zhang,¹ and Jinglong Chen²

¹*School of Mechanical and Transportation Engineering, China University of Petroleum, Beijing 102249, China*

²*School of Material Science and Engineering, Xian University of Architecture and Technology, Xian 710055, China*

Correspondence should be addressed to Jinjiang Wang; jiw09005@engr.uconn.edu

Received 26 May 2015; Revised 22 July 2015; Accepted 25 August 2015

Academic Editor: José V. Araújo dos Santos

Copyright © 2016 Lixiang Duan et al. This is an open access article distributed under the Creative Commons Attribution License, which permits unrestricted use, distribution, and reproduction in any medium, provided the original work is properly cited.

Effective signal processing in fault detection and diagnosis (FDD) is an important measure to prevent failure and accidents of machinery. To address the end distortion and frequency aliasing issues in conventional lifting wavelet transform, a Volterra series assisted undecimated lifting wavelet packet transform (ULWPT) is investigated for machinery incipient fault diagnosis. Undecimated lifting wavelet packet transform is firstly formulated to eliminate the frequency aliasing issue in traditional lifting wavelet packet transform. Next, Volterra series, as a boundary treatment method, is used to preprocess the signal to suppress the end distortion in undecimated lifting wavelet packet transform. Finally, the decomposed wavelet coefficients are trimmed to the original length as the signal of interest for machinery incipient fault detection. Experimental study on a reciprocating compressor is performed to demonstrate the effectiveness of the presented method. The results show that the presented method outperforms the conventional approach by dramatically enhancing the weak defect feature extraction for reciprocating compressor valve fault diagnosis.

1. Introduction

Fault detection and diagnosis play an important role in machinery condition monitoring to improve product quality and avoid catastrophic damage or huge production loss [1, 2]. Increasing demand on system reliability has accelerated the installation of sensors to acquire the machinery condition status. However, the signals caused by incipient fault components are usually weak and severely drowned out by the strong noise from machinery vibration and measurement system [3], which pose significant challenge on machinery fault diagnosis at early stage.

Much effort has been put on developing effective signal processing for fault detection and diagnosis during the past decades. Various signal processing techniques including wavelet transform [4], empirical mode decomposition [5], Wigner-Ville distribution [6], singular value decomposition (SVD) denoising [7, 8], and blind source separation [9, 10] have been investigated for noise suppression, enhanced weak feature extraction, and signal time-frequency decomposition.

Among these signal processing methods, wavelet transform is the most widely investigated technique. Peng and Chu conducted an overview of wavelet transform for machinery condition monitoring [11]. Yan et al. reviewed recent applications of wavelet transform in rotary machinery fault diagnosis [12]. Discrete wavelet transform was investigated to extract fault features for gearbox defect diagnosis [13]. A wavelet filter-based method with minimal Shannon entropy criterion was investigated for vibration signal denoising in bearing defect prognosis [14]. In [15], a multiscale enveloping order spectrogram based on continuous complex wavelet transform was developed for bearing incipient defect diagnosis under nonstationary operating conditions. A dual-tree complex wavelet transform based adaptive wavelet shrinkage technique was investigated for mechanical vibration signal denoising [16].

Lifting wavelet transform, which is also named as second-generation wavelet transform, has attracted considerable attention for machinery fault diagnosis. It is implemented through lifting scheme by recursive prediction and updating

operations to decompose the signal in time domain, which has the superiorities, for example, faster implementation, being independent of Fourier transform, and meanwhile retaining all advantages of traditional wavelet transform. In [17], a lifting wavelet packet decomposition method was presented to extract fault features for bearing performance degradation assessment. A redundant lifting wavelet packet transform was applied to diagnose gearbox and engine [18]. A multiwavelet lifting scheme to optimize lifting scheme was presented for gearbox diagnosis [19]. A combination of lifting wavelet and finite element method was investigated for the quantitative identification of pipeline cracks [20]. In the abovementioned studies, decimated lifting scheme using downsampling algorithm is commonly used which leads to frequency aliasing in the decomposition results [21]. On the other hand, the lifting scheme causes end distortion which confuses or misleads the diagnosis. Thus, an undecimated lifting wavelet transform with boundary treatment is needed to suppress frequency aliasing and end distortion.

Various boundary treatment methods are investigated to suppress end distortion in lifting wavelet transform. In [22, 23], the order of predictor in the lifting scheme is reduced by overlapping the edges to suppress end distortion. Different boundary extension methods, such as zero-padding extension, symmetric extension, periodic extension, zero-order smoothing extension, and one-order smoothing extension methods, are investigated in [24, 25]. These methods could suppress the end distortion to some degree, but not up to satisfaction. To address these issues, this paper presents a new signal processing method, named Volterra series assisted undecimated lifting wavelet packet transform, by extending our prior work [26]. First of all, Volterra series [27], as a boundary treatment method, is used to extend both ends of the signal. Then, the wavelet coefficients, decomposed by the undecimated lifting wavelet packet, are chopped back to original length to serve as the signals of interest for machinery incipient fault detection. Finally, the effectiveness of the presented method is demonstrated on valve incipient defect diagnosis in a reciprocating compressor. Thus, the intellectual merits of this paper are outlined including the following: (1) a Volterra series assisted undecimated lifting wavelet packet transform method is presented to suppress the end distortion and frequency aliasing issues in conventional lifting wavelet transform and (2) the formula to optimize the number of extended signal in boundary treatment using Volterra series is derived according to the decomposition property of undecimated lifting wavelet packet transform.

The rest of the paper is organized as follows. Section 2 introduces the theoretical background of lifting wavelet transform and Volterra series. Section 3 presents the theoretical framework of Volterra series assisted undecimated lifting wavelet packet transform and the equations of the undecimated lifting wavelet packet. Performance comparison of different boundary treatment methods is also discussed hereby. An experimental study of incipient fault detection of reciprocating compressor valve using the presented method is conducted, and the analysis results are discussed in Section 4. The conclusions are finally drawn in Section 5.

2. Theoretical Background

2.1. Lifting Wavelet Transform. Lifting wavelet transform was firstly presented by Sweldens in the 1990s [28]. Based on lifting scheme, it calculates the wavelet coefficients using polynomial interpolation method and constructs scaling function to obtain the low frequency coefficients of the signal. If the scaling function curve is smooth and the ringing artifact of boundary is reduced adequately, an ideal wavelet coefficient can be acquired using interpolator split schemes.

Lifting wavelet transform consists of three steps: split, prediction, and update [29].

(1) *Split.* Several methods for signal split are available. One method could be dividing signals into left and right halves. However, the result will be unsatisfying due to the low relativity degree between the left and the right halves. One more effective method is to divide the data $x[n]$ into even set $x_e[n] = x[2n]$ and odd set $x_o[n] = x[2n + 1]$, where n is the number of data.

(2) *Prediction.* The purpose of prediction is to eliminate the low frequency components of signals and preserve the high frequency part. The odd set $x_o[n]$ can be predicted from the even set $x_e[n]$ and the prediction operator $\mathbf{P} = [p_1, p_2, \dots, p_N]$. The prediction value is $\mathbf{P}(x_e[n])$. The difference between the practical value and the prediction value is defined as $d[n]$:

$$d[n] = x_o[n] - \mathbf{P}(x_e[n]), \quad (1)$$

where $d[n]$, also called detailed signal, reflects the high frequency component of the signals. Here, N is a dual vanishing moment that determines the smoothness of the interpolation function.

(3) *Update.* In order to reduce the frequency aliasing effect, the odd set $x_e[n]$ is updated using detail signal $d[n]$ and update operator $\mathbf{U} = [u_1, u_2, \dots, u_N]$. The result of this step is the approximation signal $c[n]$ that reflects the low frequency coefficient of the signals, which can be written as

$$c[n] = x_e[n] + \mathbf{U}(d[n])\mathbf{P}(x_e[n]). \quad (2)$$

Signals can be decomposed by lifting wavelet transform using the above iterative operation of approximation signal $c[n]$. Prediction coefficients can be calculated by the Lagrange interpolation formula. As long as the length of the update operator is the same as that of the prediction operator, the update coefficient value will be half of the corresponding prediction coefficient [30]. However, the downsampling algorithm used in the conventional lifting wavelet transform will lead to frequency aliasing because the transformed signal becomes half of its length in the previous layer. The update algorithm can reduce but not completely eliminate frequency aliasing. The signal after downsampling algorithm will not meet the conditions of sampling theorem, which leads to unexpected virtual frequency components. Thus, an undecimated lifting wavelet transform is outlined and discussed to eliminate frequency aliasing in this study.

2.2. Volterra Series. Volterra series was initially proposed by an Italian mathematician, named Vito Volterra, in the 1880s. Due to its powerful ability to model the behavior of nonlinear systems, the theory has attracted a great deal of attention and soon gained its applications in many fields. If the input of a nonlinear discrete time system is $\mathbf{X}(n) = [x(n), x(n-1), \dots, x(n-N'+1)]$ and the output is $y(n) = \widehat{x}'(n+1)$, the system function can construct nonlinear prediction model with the expansion of Volterra series as given by [31]

$$\begin{aligned} \widehat{x}'(n+1) &= h_0 + \sum_{i=0}^{+\infty} h_1(i) x(n-i) + \sum_{i=0}^{+\infty} \sum_{j=0}^{+\infty} h_2(i, j) \\ &\cdot x(n-i) x(n-j) + \dots \\ &+ \sum_{i=0}^{+\infty} \sum_{j=0}^{+\infty} \dots \sum_{k=0}^{+\infty} h_p(i, j, \dots, k) x(n-i) x(n-j) \\ &\dots x(n-k), \end{aligned} \quad (3)$$

where $h_p(i, j, \dots, k)$ is the p th order nucleus of Volterra.

The expansion of this infinite order series is extremely difficult in practical applications. Generally, the second-order truncation is employed as follows:

$$\begin{aligned} \widehat{x}'(n+1) &= h_0 + \sum_{i=0}^{N_1-1} h_1(i) x(n-i) \\ &+ \sum_{i=0}^{N_2-1} \sum_{j=0}^{N_2-1} h_2(i, j) x(n-i) x(n-j), \end{aligned} \quad (4)$$

where N_1 and N_2 represent the length of filters. The minimum embedding dimension m of the signal can be obtained using the fault near-neighbor method. Consequently, N_1 and N_2 can be set as m [32].

Volterra series is used to extend both ends of the signal to address the end distortion issue in lifting wavelet transform. The integrative approach of Volterra series and lifting wavelet transform is presented in detail in the following sections.

The input vector is $\mathbf{X}(n) = [1, x(n), x(n-1), \dots, x(n-m-1), x^2(n), x(n)x(n-1), \dots, x^2(n-m+1)]^T$. The prediction coefficient vector is $\mathbf{W}(n) = [h_0, h_1(0), h_1(1), \dots, h_1(m-1), h_2(0,0), h_2(0,1), \dots, h_2(m-1, m-1)]^T$. Thus, the expression of (4) can be rewritten as [33]

$$\widehat{x}'(n+1) = \mathbf{X}^T(n) \mathbf{W}(n). \quad (5)$$

The prediction coefficient vector $\mathbf{W}(n)$ is calculated using the recursive least-squares method (RLS). To elaborate, consider

$$\mathbf{Q}(0) = \delta^{-1} \mathbf{I}, \quad (6)$$

where δ is a very small normal number and \mathbf{I} is the identity matrix. Thus, $\mathbf{W}(0)$ is set as

$$\mathbf{W}(0) = 0 \quad (7)$$

and $\mathbf{W}(n)$ is calculated by carrying on the following iterative computation.

Consider

$$G(n) = \frac{\mu^{-1} \mathbf{Q}(n-1) \mathbf{X}(n)}{1 + \mu^{-1} \mathbf{X}^T(n) \mathbf{Q}(n-1) \mathbf{X}(n)}, \quad (8)$$

where μ is a forgetting factor.

Consider the following:

$$\alpha(n) = D(n) - \mathbf{W}^T(n-1) \mathbf{X}(n), \quad (9)$$

where $D(n)$ is an ideal output signal. Thus,

$$\begin{aligned} \mathbf{W}(n) &= \mathbf{W}(n-1) + G(n) \alpha(n), \\ \mathbf{Q}(n) &= \mu^{-1} \mathbf{Q}(n-1) - \mu^{-1} G(n) \mathbf{X}^T(n) \mathbf{Q}(n-1), \end{aligned} \quad (10)$$

where $\alpha(n)$ and $G(n)$ are intermediate variables.

The details of theoretical knowledge of lifting wavelet transform and Volterra series model have been discussed above. Volterra series is used to extend both ends of the signal to address the end distortion issue in lifting wavelet transform. The formulation of Volterra series assisted undecimated lifting wavelet transform is illustrated below.

3. The Proposed Method

A Volterra series-assisted undecimated lifting wavelet packet transform is proposed for machinery incipient defect diagnosis to eliminate the frequency aliasing and end distortion issues in traditional lifting wavelet transform, and its flow-chart is shown in Figure 1.

First, both ends of the original signal are extended and predicted with Volterra series model, in which the parameter of extension number is optimized. Next, the extended signal is decomposed by undecimated lifting wavelet packet transform and the subband with the highest energy ratio is selected as the band of interest. The selected subband signal is then trimmed back to its original length for envelope analysis. Finally, the machinery status is assessed according to the analysis results. The details of undecimated lifting wavelet packet transform with boundary treatment are discussed as below.

3.1. Formulation of Undecimated LWPT with Boundary Treatment. The undecimated algorithm can eliminate frequency aliasing because the length of coefficients at each level is equal to that of the raw signal. The \mathbf{P} and \mathbf{U} can be schemed out as initial prediction operator and initial update operator, respectively, and the undecimated algorithm is deduced as follows.

Assuming $\mathbf{P} = \{p_i\}$, where $i = 1, 2, \dots, N$, the expression of the undecimated prediction operator of the l th level is given by [34]

$$\mathbf{P}_j^{[l]} = \begin{cases} p_i, & j = 2^l \cdot i, \\ 0, & j \neq 2^l \cdot i, \end{cases} \quad j = 1, \dots, 2^l N. \quad (11)$$

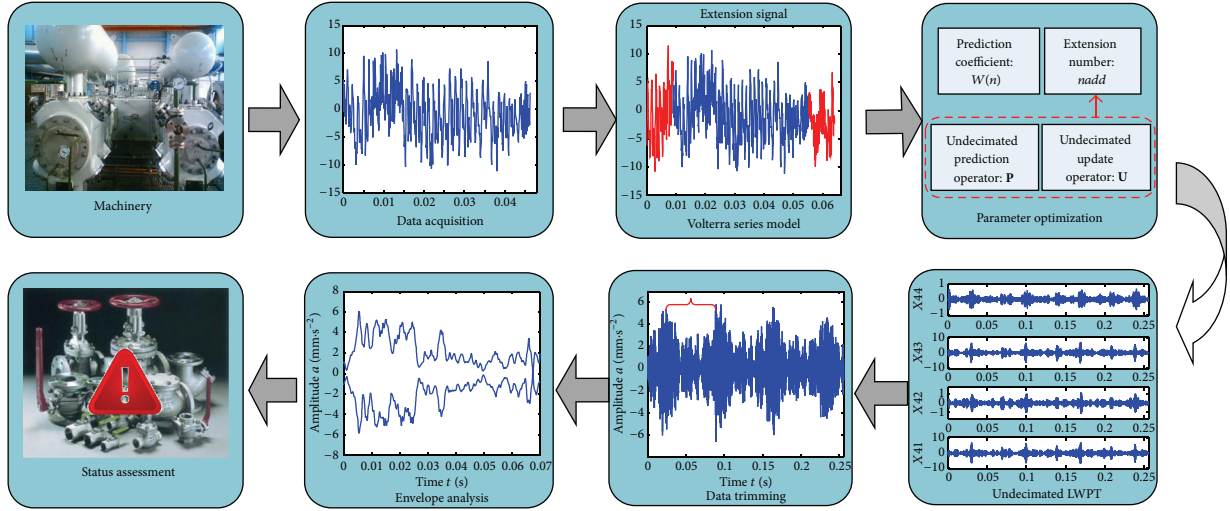


FIGURE 1: Flowchart of the proposed approach for machinery incipient defect diagnosis.

According to the principle of equidistance subdivision, the predictor coefficient p_i is calculated by Lagrange interpolation formula as [29]

$$p_i = \prod_{\substack{k=1 \\ k \neq i}}^N \frac{(N+1)/2 - k}{i - k}, \quad i = 1, 2, \dots, N, \quad (12)$$

where i is an index number and N is the predictor length.

Similarly, assuming $\mathbf{U} = \{u_i\}$, where $i = 1, 2, \dots, N'$, the expression of the undecimated update operator of the l th level is obtained by [34]

$$\mathbf{U}_j^{[l]} = \begin{cases} u_i, & j = 2^l \cdot i, \\ 0, & j \neq 2^l \cdot i, \end{cases} \quad j = 1, \dots, 2^l N', \quad (13)$$

where u_i is the update coefficient and is usually set as the half of the predictor coefficient p_i .

Assuming x_{lk} is the k th frequency band of the l th level signal decomposed from the original signal $x[n]$, $x_{l(k-1)}$ and x_{lk} can be obtained by dividing $x_{(l-1)(k/2)}$,

$$\begin{aligned} x_{l(k-1)}(n) &= x_{(l-1)(k/2)}(n) \\ &\quad - [p_1^{[l]} x_{(l-1)(k/2)}(n - 2^{l-1}(N+1) + 1) \\ &\quad + p_2^{[l]} x_{(l-1)(k/2)}(n - 2^{l-1}(N+1) + 2) + \dots \\ &\quad + p_{2^l N}^{[l]} x_{(l-1)(k/2)}(n + 2^{l-1}(N-1))], \\ x_{lk}(n) &= x_{(l-1)(k/2)}(n) \\ &\quad + [u_1^{[l]} x_{l(k-1)}(n - 2^{l-1}(N'+1) + 1) \\ &\quad + u_2^{[l]} x_{l(k-1)}(n - 2^{l-1}(N'+1) + 2) + \dots \\ &\quad + u_{2^l N'}^{[l]} x_{l(k-1)}(n + 2^{l-1}(N'-1))], \end{aligned} \quad (14)$$

where $k = 2, 4, 6, \dots, 2^l$; $p_i^{[l]}$ is the undecimated prediction operator of $x_{l(k-1)}$; and $u_i^{[l]}$ is the undecimated update operator of x_{lk} .

Assuming the undecimated prediction operator $\mathbf{P} = \{p_i\}$ and the undecimated update operator $\mathbf{U} = \{u_i\}$, where $i = 1, 2, \dots, 4$, x_i is the i th data of \mathbf{X} . The i th data of the first level detailed signal decomposed by undecimated lifting wavelet packet transform is obtained as follows:

$$\begin{aligned} d_{1,i} &= x_i - (x_{i-3} \times p_1 + x_{i-2} \times 0 + x_{i-1} \times p_2 + x_i \times 0 \\ &\quad + x_{i+1} \times p_3 + x_{i+3} \times p_4). \end{aligned} \quad (15)$$

It can be deduced that three numbers must be extended to the left end of x when calculating $d_{1,1}$ and the same number to the right when calculating the last data $d_{1,n}$. Similarly, for the second level, 6 more numbers should be extended to each end, and so on. More generally, assuming N_f is the decomposed level of undecimated lifting wavelet packet transform, the extension number of the original signal at each end can be calculated as

$$\begin{aligned} n_{\text{add}} &= \sum_{l=1}^{N_f} [2^{l-1}(N+1) - 1] \\ &\quad + \sum_{l=1}^{N_f} [2^{l-1}(N'+1) - 1]. \end{aligned} \quad (16)$$

According to (16), the length of extended signal in Volterra series model is determined, and the signal is extended based on the procedure of Volterra series model in Section 2. The performance of formulated method is discussed below.

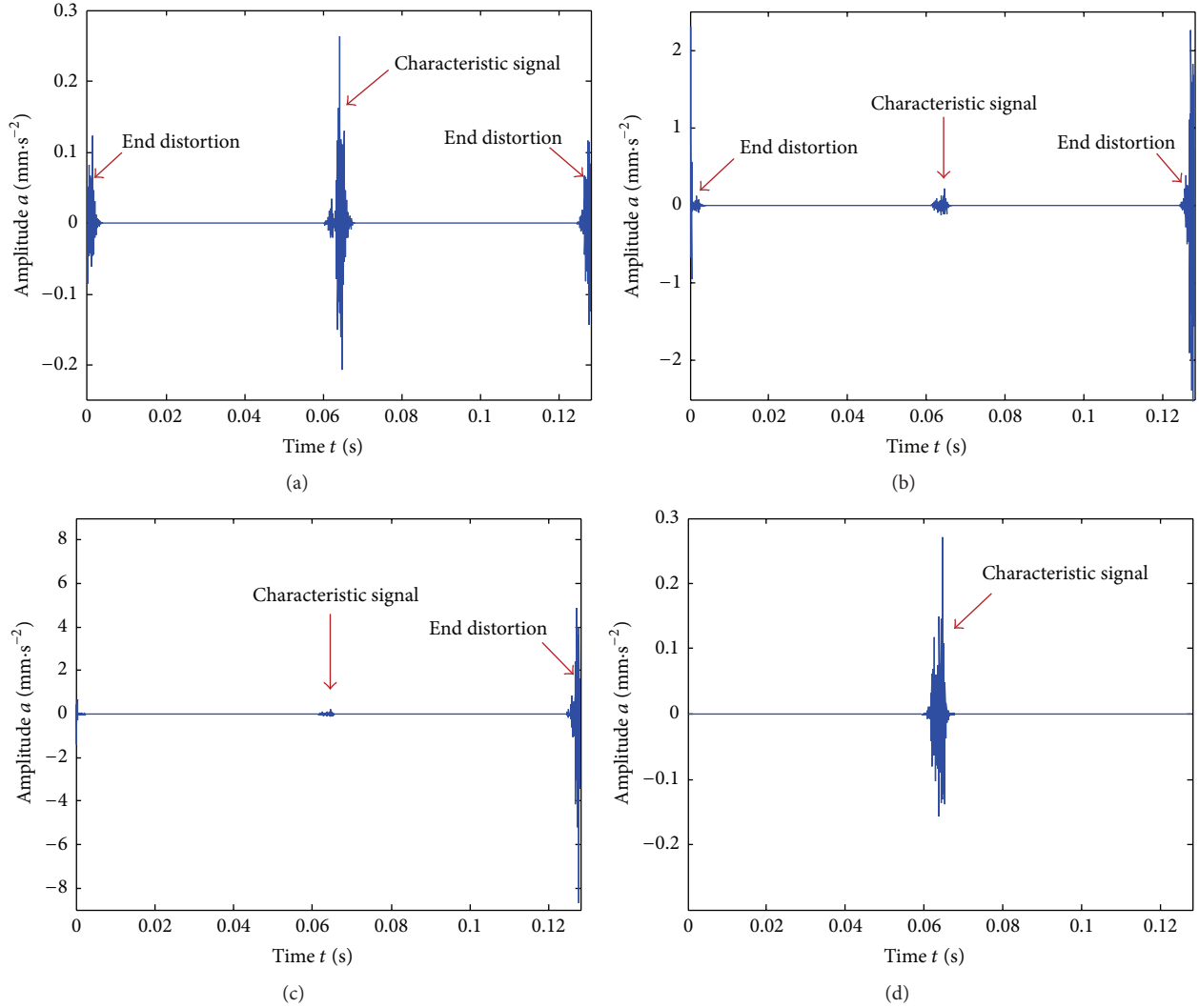


FIGURE 2: One subband in the fourth layer decomposed using wavelet packet and preprocessed by different methods: (a) no extension, (b) zero-padding extension, (c) periodic extension, and (d) second-order Volterra series prediction.

3.2. Performance Comparison of Boundary Treatment Methods. To evaluate the performance of various boundary treatment methods, a synthesized signal is constructed as follows:

$$\begin{aligned}
 x(t) = & 0.3 \exp(-2\pi \times 100t) \sin(2\pi \times 400t) \\
 & + 1.5 \sin\left(2\pi \times 50t + \frac{\pi}{4}\right) \\
 & + 3 \sin\left(2\pi \times 100t + \frac{\pi}{6}\right).
 \end{aligned} \quad (17)$$

The sampling frequency is set as 16,000 Hz. The synthesized signal is decomposed into four layers using the undecimated lifting wavelet transform. Figure 2 shows one subband of the fourth layer, corresponding to the pulse train signal, under different preprocessing scenarios, (a) no extension, (b) zero-padding extension, (c) periodic extension, and (d) second-order Volterra series prediction, respectively.

There are obvious end distortions shown by the arrows in Figures 2(a)–2(c). Therefore, if the characteristic signal is just

located in the end, it will be submerged by the end distortions. In Figures 2(b)–2(c), the characteristic signal in the middle is insignificant because the end distortion is strong. The Volterra series based preprocessing method shows the optimal performance since the end distortions have been restrained effectively as shown in Figure 2(d).

4. Experimental Study

A reciprocating compressor (model number 4HOS-6) in a petrochemical plant in China is used as the experimental testbed to evaluate the performance of the developed method, as shown in Figure 3. It is a 4-cylinder natural gas reciprocating compressor driven by an 8-cylinder gas engine with rated power of 1,600 kW. The rotating speed of crankshaft is 860 rpm which drives the plungers to strike 860 times per minute, back and forth. The motion of the plungers changes the volume of the cylinders. When the plunger moves down, the increased volume of cylinder opens intake valve and

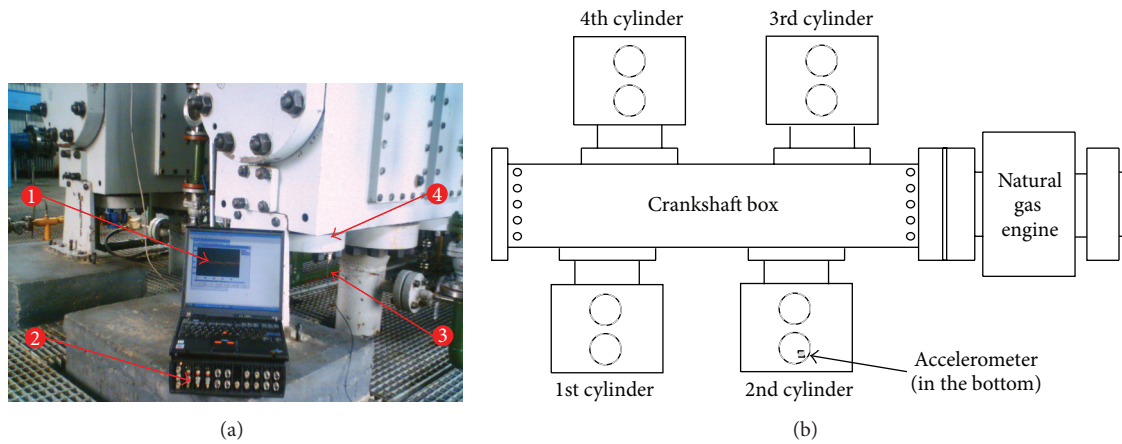


FIGURE 3: Illustration of experimental setup, (a) data acquisition system, ① control panel, ② data acquisition box, ③ accelerometer on the exhaust valve lid, ④ exhaust valve, and (b) diagram of reciprocating compressor.

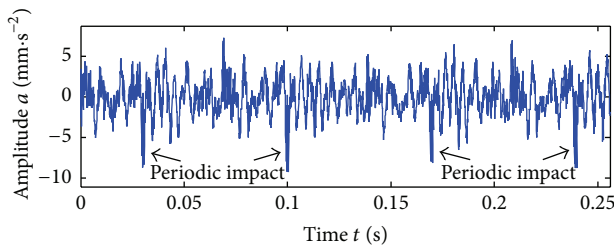


FIGURE 4: The time series vibrational signal of normal valve.

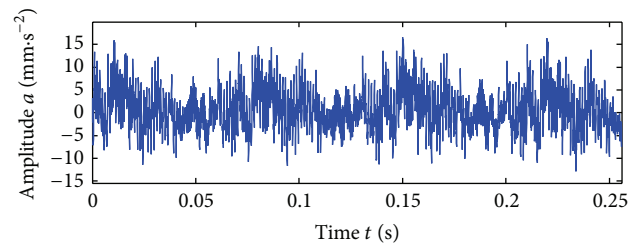


FIGURE 5: The time series vibrational signal of abnormal valve.

closes the exhaust valve. When the plunger moves up, the compression of cylinder opens the exhaust valve and closes the intake valve. Valve is composed of lifting limiter, spring, disc, and seat, of which spring is the most susceptible to failure.

To diagnose the valve failure in the 2nd cylinder, an accelerometer is placed on the exhaust valve lid. A customer designed data acquisition system (model number MDES-5) as shown in Figure 3(a) is used to acquire the measurements. It consists of a laptop and a data acquisition box configured in a master-slave system. The sampling rate is set as 16 kHz in this study. Figures 4 and 5 show the time series vibrational signals near the exhaust valve of 2nd cylinder under normal condition and abnormal condition, respectively. For comparison, the amplitude of the vibration signal under abnormal condition is greater than the one of the normal signal. Taking the RMS (root mean square) as the criterion, the RMS of the abnormal signal is calculated as $4.725 \text{ m}\cdot\text{s}^{-2}$ which is greater than that of the normal signal ($2.227 \text{ m}\cdot\text{s}^{-2}$). However, the periodic impact feature caused by the collision of the valve disc and seat is difficult to observe due to strong background noise.

For further analysis, the proposed method based on Volterra series and undecimated lifting wavelet packet transform is used to process the signals. The two ends of the original signal are extended and predicted by the Volterra series model. Then, the predicted signal is decomposed into four

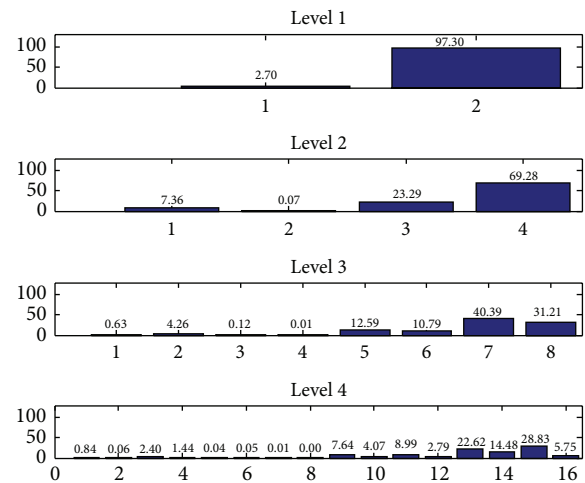


FIGURE 6: Energy distribution of four-level subbands.

layers by undecimated lifting wavelet packet transform, where $N = N' = 4$. From (11)–(13), the prediction operator \mathbf{P} and the update operator \mathbf{U} can be obtained as $\mathbf{P} = [-0.0625, 0.5625, 0.5625, -0.0625]$ and $\mathbf{U} = [-0.0313, 0.2813, 0.2813, -0.0313]$. Finally, the 16 subbands of the fourth level are obtained and the energy distribution of the subbands at different levels is shown in Figure 6. After undecimated lifting wavelet packet decomposition, the majority of the energy rests on the high frequency parts which

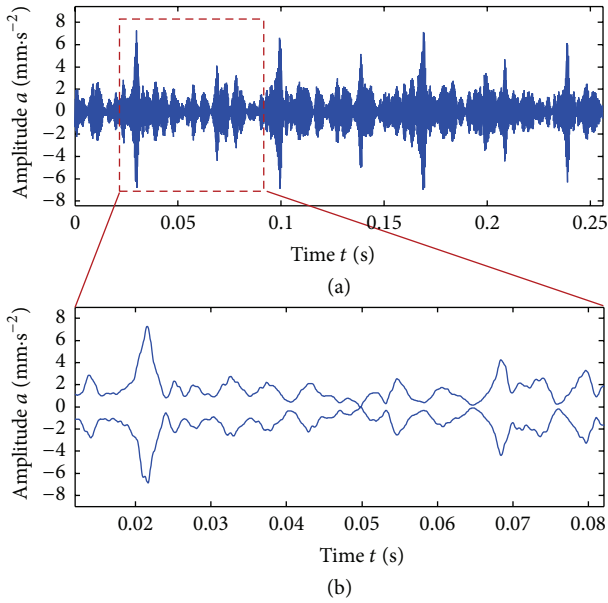


FIGURE 7: The wavelet coefficient at selected subband and its envelope under normal condition.

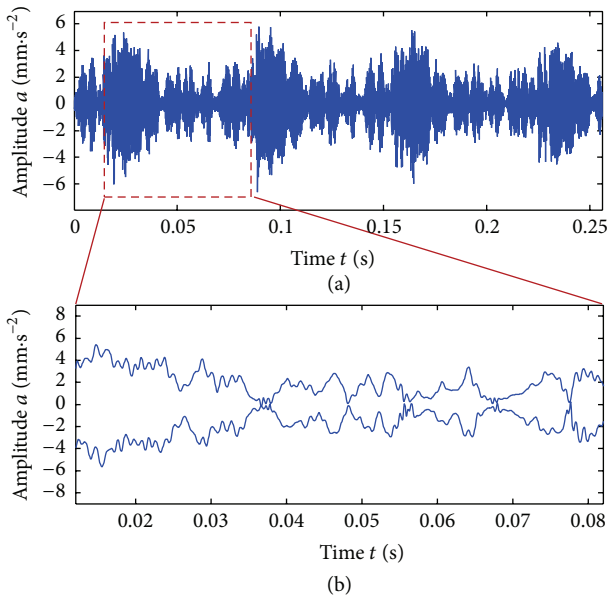


FIGURE 8: The wavelet coefficient at selected subband and its envelope under abnormal condition.

correspond to the detailed wavelet coefficients. The subband with the highest energy ratio is selected as the band of interest. The wavelet coefficients and their envelopes from the selected subbands are shown in Figures 7 and 8, corresponding to the normal condition and abnormal condition, respectively. From both figures, the periodic impact features are visible and easily identified.

The signal in one period, as shown by the red block in Figures 7(a) and 8(a), is extracted for detailed analysis. According to the working principle of exhaust valve, the front

half curve, from 0.012 to 0.047 sec, represents the valve-close phase while the latter one, from 0.047 to 0.082 sec, shows the exhaust phase. The exhaust valve closes at point A, and the valve opens again at point B. Under normal condition, there is no chattering when normal valve closes because the stiffness of spring is rigid enough to close tightly. By contrast, valve chatters significantly which is caused by the repeated collision of valve and seat during the time period T (indicating the aging and stretch decline of spring in the valve). The valve with aged spring cannot close tightly resulting in gas leak and efficiency degradation. When this compressor is stopped and checked, the spring failure is validated by visual inspection, and the exhaust valve is maintained. Therefore, the presented incipient fault diagnosis method avoids accidents and prevents huge production loss.

In addition, the energy of the selected band signal is used to evaluate the performance of the presented method. Figure 9(a) shows the energies of the selected band signals under four different scenarios: (I) undecimated LWPT (ULWPT) under normal machinery condition, (II) undecimated LWPT (ULWPT) under abnormal machinery condition, (III) Volterra series assisted undecimated LWPT (V-ULWPT) under normal machinery condition, and (IV) Volterra series assisted undecimated LWPT (V-ULWPT) under abnormal machinery condition. From the analysis results, it is found that the normal and abnormal machinery conditions can be differentiated according to energy of selected subband using undecimated lifting wavelet packet transform. Since Volterra series assisted ULWPT suppresses the end distortion, the energy of selected subband using V-ULWPT is less than that using ULWPT. However, the energy ratio of abnormal to normal conditions using V-ULWPT is larger than that using ULWPT as shown in Figure 9(b), thus validating the effectiveness of presented Volterra series assisted lifting wavelet packet transform method.

The computational efficiency of the developed technique has also been evaluated on a desktop (Lenovo Yangtian T4900d model, Lenovo Inc., Beijing, China) with a 3.3 GHz CPU and 4 GB memory. It takes approximately 1.19 seconds to process a data string containing 4,096 data points, which is equivalent to processing 0.256 seconds data length under a 16 kHz sampling rate. Thus the presented method is applicable for online machinery diagnosis in practical applications.

5. Conclusions

An enhanced weak feature extraction approach that combines Volterra series model and undecimated lifting wavelet packet transform has been presented for incipient fault detection. The analysis results show that Volterra series assisted undecimated lifting wavelet packet transform eliminates the frequency aliasing and end distortion issues in conventional lifting wavelet packet transform method; thus it is significant to machinery incipient defect diagnosis, especially for weak impact feature extraction. From the engineering application perspective, the weak impact signals caused by the fault of a valve in reciprocating compressor are analyzed using the presented method, and the early spring failure is detected from the extracted weak features using the presented method.

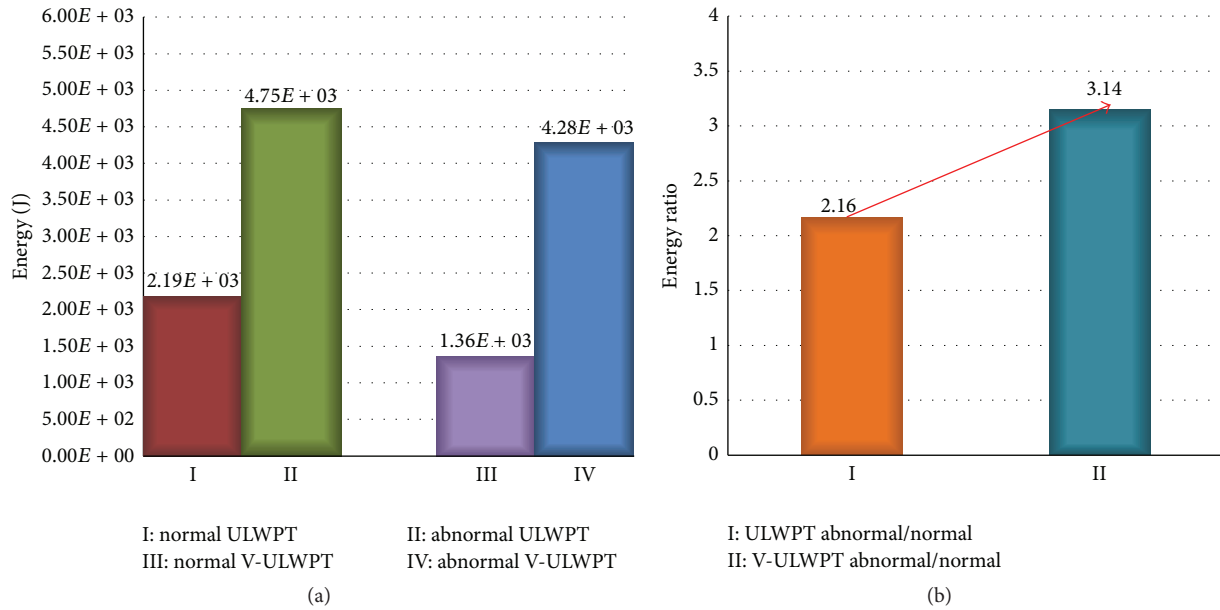


FIGURE 9: Energy comparison among different conditions: (a) energy comparison chart, (b) energy ratio chart.

Conflict of Interests

The authors declare that there is no conflict of interests regarding the publication of this paper.

Acknowledgments

This research acknowledges the financial support provided by National Science foundation of China (no. 51504274), Science Foundation of China University of Petroleum, Beijing (nos. 2462014YJRC039 and 2462015YQ0403), and Beijing Municipal Education Commission Cooperative Construction Project. Valuable comments from anonymous reviewers are greatly appreciated.

References

- [1] V. Venkatasubramanian, R. Rengaswamy, K. Yin, and S. N. Kavuri, "A review of process fault detection and diagnosis: part I: quantitative model-based methods," *Computers and Chemical Engineering*, vol. 27, no. 3, pp. 293–311, 2003.
- [2] M. Liang and I. S. Bozchalooi, "An energy operator approach to joint application of amplitude and frequency-demodulations for bearing fault detection," *Mechanical Systems and Signal Processing*, vol. 24, no. 5, pp. 1473–1494, 2010.
- [3] Z. Zhong, Z. Jiang, Y. Long, and X. Zhan, "Analysis on the noise for the different gearboxes of the heavy truck," *Shock and Vibration*, vol. 2015, Article ID 476460, 5 pages, 2015.
- [4] W. J. Wang, "Wavelet transform in vibration analysis for mechanical fault diagnosis," *Shock and Vibration*, vol. 3, no. 1, pp. 17–26, 1996.
- [5] Y. Lei, J. Lin, Z. He, and M. J. Zuo, "A review on empirical mode decomposition in fault diagnosis of rotating machinery," *Mechanical Systems and Signal Processing*, vol. 35, no. 1-2, pp. 108–126, 2013.
- [6] N. Baydar and A. Ball, "A comparative study of acoustic and vibration signals in detection of gear failures using Wigner-Ville distribution," *Mechanical Systems and Signal Processing*, vol. 15, no. 6, pp. 1091–1107, 2001.
- [7] W.-X. Yang and P. W. Tse, "Development of an advanced noise reduction method for vibration analysis based on singular value decomposition," *NDT & E International*, vol. 36, no. 6, pp. 419–432, 2003.
- [8] H. Hassanpour, A. Zehtabian, and S. J. Sadati, "Time domain signal enhancement based on an optimized singular vector denoising algorithm," *Digital Signal Processing*, vol. 22, no. 5, pp. 786–794, 2012.
- [9] J. Wang, R. X. Gao, and R. Yan, "Integration of EEMD and ICA for wind turbine gearbox diagnosis," *Wind Energy*, vol. 17, no. 5, pp. 757–773, 2014.
- [10] A. Sadhu and B. Hazra, "A novel damage detection algorithm using time-series analysis-based blind source separation," *Shock and Vibration*, vol. 20, no. 3, pp. 423–438, 2013.
- [11] Z. K. Peng and F. L. Chu, "Application of the wavelet transform in machine condition monitoring and fault diagnostics: a review with bibliography," *Mechanical Systems and Signal Processing*, vol. 18, no. 2, pp. 199–221, 2004.
- [12] R. Yan, R. X. Gao, and X. Chen, "Wavelets for fault diagnosis of rotary machines: a review with applications," *Signal Processing*, vol. 96, pp. 1–15, 2014.
- [13] N. Saravanan and K. I. Ramachandran, "Incipient gear box fault diagnosis using discrete wavelet transform (DWT) for feature extraction and classification using artificial neural network (ANN)," *Expert Systems with Applications*, vol. 37, no. 6, pp. 4168–4181, 2010.
- [14] H. Qiu, J. Lee, J. Lin, and G. Yu, "Wavelet filter-based weak signature detection method and its application on rolling element bearing prognostics," *Journal of Sound and Vibration*, vol. 289, no. 4-5, pp. 1066–1090, 2006.
- [15] J. Wang, R. X. Gao, and R. Yan, "Multi-scale enveloping order spectrogram for rotating machine health diagnosis," *Mechanical Systems and Signal Processing*, vol. 46, no. 1, pp. 28–44, 2014.

- [16] Y.-L. Chen, P.-L. Zhang, B. Li, and D.-H. Wu, "Denoising of mechanical vibration signals using quantum-inspired adaptive wavelet shrinkage," *Shock and Vibration*, vol. 2014, Article ID 848097, 7 pages, 2014.
- [17] Y. Pan, J. Chen, and X. Li, "Bearing performance degradation assessment based on lifting wavelet packet decomposition and fuzzy c-means," *Mechanical Systems and Signal Processing*, vol. 24, no. 2, pp. 559–566, 2010.
- [18] R. Zhou, W. Bao, N. Li, X. Huang, and D. Yu, "Mechanical equipment fault diagnosis based on redundant second generation wavelet packet transform," *Digital Signal Processing: A Review Journal*, vol. 20, no. 1, pp. 276–288, 2010.
- [19] J. Yuan, Z. He, and Y. Zi, "Gear fault detection using customized multiwavelet lifting schemes," *Mechanical Systems and Signal Processing*, vol. 24, no. 5, pp. 1509–1528, 2010.
- [20] Y. He, X. Chen, J. Xiang, and Z. He, "Adaptive multiresolution finite element method based on second generation wavelets," *Finite Elements in Analysis and Design*, vol. 43, no. 6-7, pp. 566–579, 2007.
- [21] W. Bao, R. Zhou, J. Yang, D. Yu, and N. Li, "Anti-aliasing lifting scheme for mechanical vibration fault feature extraction," *Mechanical Systems and Signal Processing*, vol. 23, no. 5, pp. 1458–1473, 2009.
- [22] R. L. Claypoole, G. M. Davis, W. Sweldens, and R. G. Baraniuk, "Nonlinear wavelet transforms for image coding via lifting," *IEEE Transactions on Image Processing*, vol. 12, no. 12, pp. 1449–1459, 2003.
- [23] R. L. Claypoole, R. G. Baraniuk, and R. D. Nowak, "Adaptive wavelet transforms via lifting," Report ECE TR-9304, 1999, <https://scholarship.rice.edu/handle/1911/19808>.
- [24] B. Appleton and H. Talbot, "Recursive filtering of images with symmetric extension," *Signal Processing*, vol. 85, no. 8, pp. 1546–1556, 2005.
- [25] B. Wohlberg and C. M. Brislawn, "Symmetric extension for lifted filter banks and obstructions to reversible implementation," *Signal Processing*, vol. 88, no. 1, pp. 131–145, 2008.
- [26] L. Duan, L. Zhang, and J. Chen, "Boundary treatment of lifting wavelet transform based on Volterra series model and its application," *Chinese Journal of Scientific Instrument*, vol. 33, no. 1, pp. 7–12, 2012.
- [27] D. Aiordachioaie, E. Ceanga, R. de Keyser, and Y. Naka, "Detection and classification of non-linearities based on Volterra kernels processing," *Engineering Applications of Artificial Intelligence*, vol. 14, no. 4, pp. 497–503, 2001.
- [28] W. Sweldens, "The lifting scheme: a custom-design construction of biorthogonal wavelets," *Applied and Computational Harmonic Analysis*, vol. 3, no. 2, pp. 186–200, 1996.
- [29] W. Sweldens, "The Lifting Scheme: a construction of second generation wavelets," *SIAM Journal on Mathematical Analysis*, vol. 29, no. 2, pp. 511–546, 1998.
- [30] A. Ben and T. Hugues, "Recursive filtering of images with symmetric extension," *Signal Processing*, vol. 85, no. 8, pp. 1546–1556, 2005.
- [31] D. Aiordachioaie, E. Ceanga, R. De Keyser, and Y. Naka, "Detection and classification of non-linearities based on Volterra kernels processing," *Engineering Applications of Artificial Intelligence*, vol. 14, no. 4, pp. 497–503, 2001.
- [32] M. B. Kennel, R. Brown, and H. D. I. Abarbanel, "Determining embedding dimension for phase-space reconstruction using a geometrical construction," *Physical Review A*, vol. 45, no. 6, pp. 3403–3411, 1992.
- [33] J. Zhang and X. Xiao, "Predicting low-dimensional chaotic time series using Volterra adaptive filters," *Acta Physica Sinica*, vol. 49, no. 3, pp. 403–408, 1999.
- [34] J. Hongkai, H. Zhengjia, D. Chendong, and C. Peng, "Gear-box fault diagnosis using adaptive redundant Lifting Scheme," *Mechanical Systems and Signal Processing*, vol. 20, no. 8, pp. 1992–2006, 2006.

Research Article

Experimental Study on Progressive Collapse Performance of Frame with Specially Shaped Columns Subjected to Middle Column Removal

Tiecheng Wang,^{1,2} Qingwei Chen,¹ Hailong Zhao,^{1,2} and Lei Zhang¹

¹School of Civil Engineering, Tianjin University, Tianjin 300072, China

²Key Laboratory of Coast Civil Structure Safety, Tianjin University, Ministry of Education, Tianjin 300072, China

Correspondence should be addressed to Hailong Zhao; hlongzhao.tju@163.com

Received 13 May 2015; Revised 27 August 2015; Accepted 31 August 2015

Academic Editor: Gilbert-Rainer Gillich

Copyright © 2016 Tiecheng Wang et al. This is an open access article distributed under the Creative Commons Attribution License, which permits unrestricted use, distribution, and reproduction in any medium, provided the original work is properly cited.

A static collapse experiment was carried out to study the progressive collapse resistance and failure mechanisms and modes of a 1/3-scale, 2 × 3-bay, and 2-story reinforced concrete frame with specially shaped columns subjected to middle column removal. A vertical concentrated load was applied to the top of the middle column to simulate the gravity load of the upper floors and the applied load was statically transmitted to the adjacent columns through the frame beams and slabs during the collapse process. The frame collapsed when the vertical displacement of the joint on the top of the failed column reached 170 mm due to the failure of beam-column joints. Based on the experimental phenomena and results, the progressive collapse-resistant behavior of the model frame is analyzed and the redistribution and transition of the load resisting mechanisms are discussed. It is concluded that the redistribution of internal force was mainly realized via the beam resisting mechanism and the compressive arch action in beams played an important role to improve the collapse-resistant capacity.

1. Introduction

Progressive collapse is defined as the spread of an initial local failure from element to element eventually resulting in collapse of an entire structure or a disproportionately large part of it [1]. Many practicing engineers and academic researchers have been engaged in the prevention of progressive collapse since the partial collapse of the Ronan Point apartment building in 1968. In particular, widespread concerns of progressive collapse of structures have accelerated since the 9/11 event leading to the collapse of the New York World Trade Center twin towers [2]. In recent years, the development of analysis methods for evaluating the progressive collapse potential of an existing or new building has been an imperative subject. Some nations are investigating progressive collapse resistance, and a series of design specifications and guidelines have been published [3–5]. One approach to evaluate progressive collapse of structures is to study the effects of instantaneous removal of a load-bearing element such as a column. A number of

experimental studies have been carried out to investigate progressive collapse performance of RC structures subjected to column removal. Sasani and Kropelnicki [6] carried out experiments to study the behavior of a scaled model of a continuous perimeter beam in a RC frame structure following removal of a supporting column. Sasani et al. [7] evaluated potential progressive collapse of an actual 10-story reinforced concrete structure following the explosion of an exterior column. Yi et al. [8] carried out a static experimental study of a three-story RC frame structure to investigate progressive failure due to the loss of a lower story column. A number of experimental studies also have been carried out to investigate large-deformation behavior of reinforced concrete beam-column assemblies. Kim and Yu [9] indicated that seismically designed RC moment frames could resist progressive collapse by activation of beam catenary force at large displacement. Su et al. [10] indicated a significant enhancement of the beam flexural strength because of the compressive arch action, which could be influenced by flexural reinforcement ratio and beam span-depth ratio. Yu and Tan [11] investigated the effect

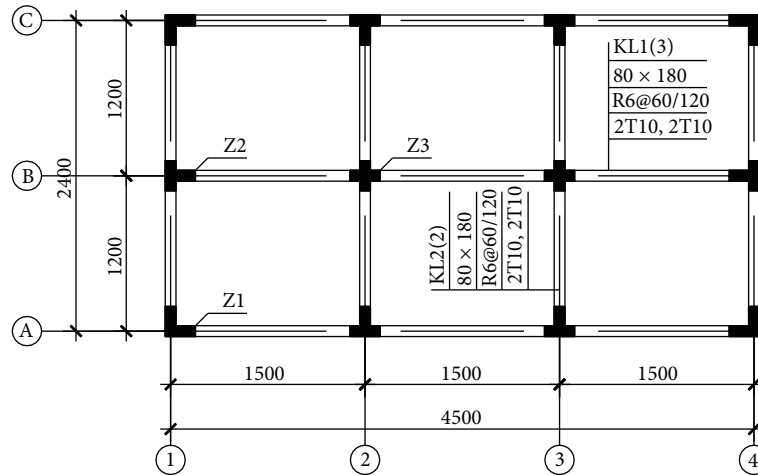


FIGURE 1: Dimensions of model frame.

of seismic detailing on structural behavior under a middle column removal scenario. Yap and Li [12] tested two series of specimens to study the structural behavior of exterior beam-column subassemblies for progressive collapse, one representing as-built design and the other representing improved design.

Reinforced concrete frame with specially shaped columns offers advantages such as avoiding prominent corners in a room, increasing usable floor area, and reducing dead load of structure combined with the use of lightweight material filler walls. However, specially shaped columns are weak at bearing capacity and seismic performance owing to the relatively smaller cross section area. Experiments on reinforced concrete frames with specially shaped columns and components had been carried out in recent years to study their seismic performance [13, 14]. However, studies on progressive collapse performance of structures are mainly concentrated on frame structures with rectangular columns and rarely involve frame structures with specially shaped columns. The frame structures with specially shaped columns are widely adopted in residential structures which will cause serious losses of lives and properties once collapse occurs. Therefore, it is necessary to conduct a further research on the progressive collapse performance of frames with specially shaped columns. A static experiment of a 1/3-scale, 2 × 3-bay, and 2-story RC frame with specially shaped columns was carried out to study the collapse-resistant behavior, redistribution of internal forces, and failure modes of RC frame with specially shaped columns following the loss of one column on the first story.

2. Design of Testing Model Frame

In order to study the progressive collapse performance and failure mechanism of RC frame with specially shaped columns when the vertical load-bearing component failed, a 1/3-scale, 2 × 3-bay, 2-story RC frame was designed and manufactured as a reduced order model of a prototype four-story RC frame structure with specially shaped columns

in accordance with requirements of concrete design code [15] and technical specification for concrete structures with specially shaped columns of China [16]. The design also satisfied the Chinese seismic design code for the category VII intensity, or regions with moderate seismicity. The geometrical dimensions of the model frame are shown in Figure 1 and the reinforcement details of beams, columns, and beam-column joints at the top floor are provided in Figures 2 and 3, respectively (all dimensions are in mm). The story height was 1000 mm, and the thickness of slab was 50 mm. T8 steel bars were orthogonally arranged inside the slab with the interval of 150 mm. During the concrete casting process of the model frame, B1 column at the first story designed as the failed column was substituted by a steel tube with welded spherical joint to support the superstructure. The model frame was built on a foundation beam that was fixed on the strong reaction floor of the laboratory by anchor bolts. Lap splices, anchorage of steel bars, and spacing of stirrups were strictly in accordance with Chinese code requirements [15, 16]. Picture of completed model structure is shown in Figure 4.

The strength grades of longitudinal bars and stirrups used in beams and columns were 400 MPa and 300 MPa, respectively. 400 MPa reinforcement was used in the slabs. C40 concrete was used for the model frame. The measured values of mechanical properties of reinforcing bars and concrete used to fabricate the specimen are shown in Table 1. The average compressive strength of concrete by cubic tests was 42.3 MPa at 28 days, which is equal to 33.84 MPa by cylinder tests. Three pieces of reinforcing steel bars were tested for each nominal diameter and average characteristic mechanical properties were calculated.

3. Experimental Program

This experiment was carried out in two steps, a dynamic collapse experiment and a static collapse experiment. During the dynamic collapse experiment, the middle column B1 was suddenly removed to study the dynamic response and internal force redistribution of the model frame under gravity

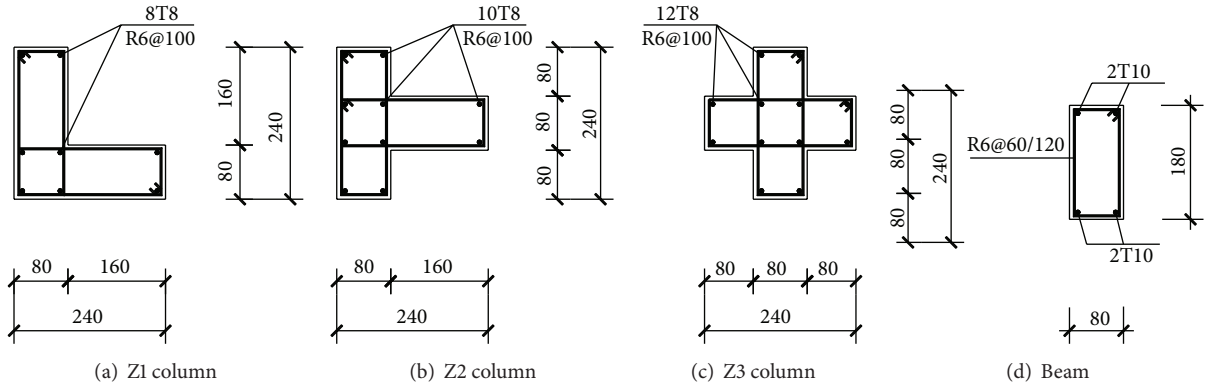


FIGURE 2: Section dimension and reinforcement details of beam and columns. (Note: R and T stand for steel bars with nominal yield strengths of 300 MPa and 400 MPa, resp.; the number following R or T represents the nominal diameter of a bar. @ stands for stirrup space. There is a decrease in spacing of stirrup by half of the near beam-column joint point according to Chinese seismic code.)

TABLE 1: Material properties of steel bars and concrete.

Bar type	Reinforcement				Concrete Cubic compressive strength (MPa)
	Yield strength (MPa)	Ultimate tensile strength (MPa)	Elastic modulus (MPa)	Ratio of elongation (%)	
300D6	417.0	541.4	2.12×10^5	30.5	42.3
400D8	454.1	640.3	2.65×10^5	28.5	
400D10	433.6	627.8	2.25×10^5	29.1	

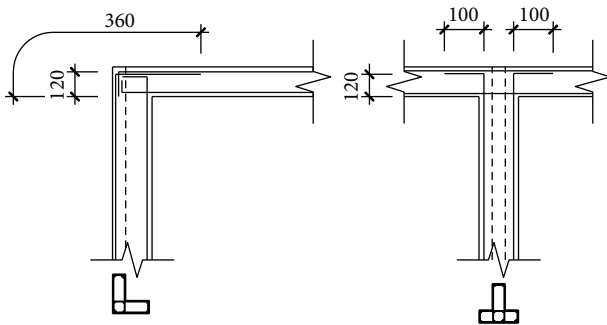


FIGURE 3: Reinforcement details of beam-column joints.



FIGURE 4: View of experimental model frame.

load. The experimental results of dynamic collapse test [17] show that the vertical displacement of the joint on the top of the failed column was only 0.176 mm and the dynamic response of the structure had no significant influence on the structure, which was still in the elastic stage, and collapse did not occur. Thus, a hydraulic jack placed on the top of the frame was used to apply a vertical load and conduct the static collapse test. The applied load is used to simulate the gravity load of the upper structure. The applied load was constantly increased until the damage of frame to study the resistance to progressive collapse, mechanism of collapse failure, and the final failure modes. The static collapse test was mainly introduced in this paper.

3.1. Loading Equipment and Protocol. As shown in Figure 4, the load in the dynamic collapse experiment was applied by

stacking sandbags uniformly on the slab. The load applied on the model frame was 2.8 kN/m^2 , which was the initial stress state of the frame. The static collapse test was conducted with a 100-ton hydraulic jack applying a vertical continuous load on the top of the frame. The loading device is schematically shown in Figure 5. The loading process was divided into two stages. Before the model frame yielded, the loading process was controlled by force. The load increment for each step was 10 kN with a rate of 20 kN/min. After the model frame yielded, a displacement-controlled manner was applied with a rate of 2 mm/min. In the beginning, the displacement increment for each step was 2 mm and then increased to 5 mm after the vertical displacement exceeding 38 mm. At the final stage, the load was continuously applied until the

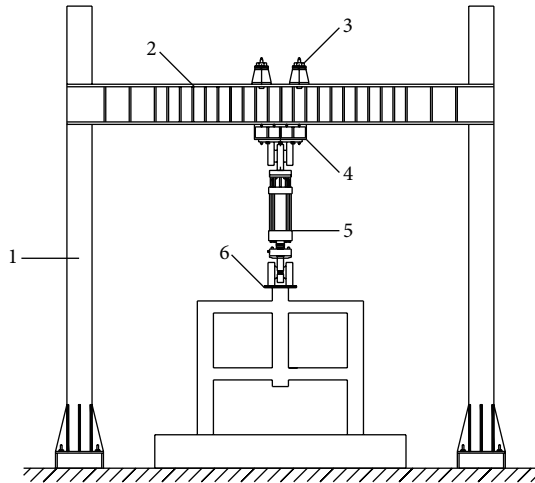


FIGURE 5: Schematic diagram of loading equipment. (Note: 1. column; 2. load-carrying beam; 3. girder; 4. box girder; 5. servo-hydraulic actuator; 6. steel plate.)

end of test. After each loading step, the load was held for 6–12 minutes to observe and record experimental phenomena such as crack development and variations.

3.2. Test Setup and Instrumentation. Strain gauges and displacement transducers were set up in key locations of the model frame. The displacement transducers were placed to measure the vertical displacement of the joint on the top of the failed column and the horizontal displacement of the model frame. Concrete strain gauges were attached onto the surface of concrete to obtain the strain data of concrete at the middle and bottom of the ground floor columns. Steel bar strain gauges were affixed on steel bars at the ends and midspan of the beams connected to the failed column. The detailed positions of the displacement transducers and strain gauges attached onto steel bars and concrete are shown in Figure 6.

4. Experimental Results

4.1. Experimental Phenomena and Failure Modes. Under monotonic vertical concentrated load on the top of the frame, the test frame experienced large displacements and rotations at the ends of the beams before failure. The failure was characterized by the following sequence: (1) crushing and spalling of concrete at the top of beam ends near the failed column and at the bottom of beam ends far away from the failed column; (2) development of flexural and shear cracks at beam ends and beam-column joints (deepening and widening); and (3) destruction of beam-column joint with a major crack opening at the joint. When the vertical displacement of the joint reached 170 mm with a corresponding beam chord rotation of 0.142 rad, obtained by dividing the center column displacement by the centerline-to-centerline beam span of 1200 mm, the top floor beam-column joints were heavily damaged and unable to provide enough anchorage for the longitudinal steel bars in beams. The frame entered an

irreversible collapse process and the test was terminated. The pictures of the damaged model frame are shown in Figure 7. As shown in the figure, the beam-column joints at the top floor of the frame were seriously damaged, indicating that the joints of frame structures with specially shaped columns were the weak areas to resist progressive collapse. This is contrary to the design principles “strong column and weak beam, strong shearing and weak bend, stronger nodes.” Moreover, the research results of Yi et al. [8] and Yu and Tan [11] show that the bearing capacities of the catenary action stage generally will increase and exceed that of flexural capacity of frame beam. However, the damage of beam-column joints limits the development of the catenary action when the joints damaged before the frame beam. Thus, these beam-column joints should be further enhanced in progressive collapse-resistant design to gain a better progressive collapse resistance.

4.2. Crack Patterns. Flexural cracks appeared in the frame beams near the middle column at both ground and top floor when testing commenced with vertical displacement of the joint. At a displacement of approximately 3.2 mm, diagonal cracks appeared along the beams as well as at joints of the top floor and the flexural cracks bend slightly due to shear and twist of the beam. When the displacement of the joint reached 3.5 mm, horizontal cracks appeared at the top of columns A1 and C1 in the top floor. It is seen that horizontal cracks appeared at the bottom of the top floor column B1 due to the twist of the beam. As the vertical displacement of the joint approached 19.5 mm, shear cracks developed at the bottom halves of the ground floor columns. At approximately the same stage, the concrete located in the tensile zone experienced spalling. The concrete located in the compressive zone experienced crushing and spalling at the later stage of loading. Figure 8 shows a map of cracks at a vertical displacement of approximately 105 mm. At this displacement, the maximum crack width was approximately 7 mm. With the increase of displacement, crack width increased continuously and penetrated through the beam without new cracks appearing. It was noted that cracks on the bottom surface of slabs extended to the cracks at the ends of beams along the diagonal line between column B1 and columns A2, C2 during the loading process, as shown in Figure 9.

4.3. Load-Displacement Relationship of Failed Column. The main purpose of the testing was to observe the load-displacement response of the failed column. Figure 10 shows the relationship between the load applied by the hydraulic jack and the vertical displacement of the joint. With the gradual increase of the vertical displacement, the bearing capacity also increased rapidly. The applied load reached the maximum value of approximately 256 kN at a vertical displacement of 65 mm. The whole loading process can be divided into four stages.

As illustrated in Figure 10, the OA segment can be considered as the elastic stage, during which the relationship between the load and the vertical displacement of the joint is linear, without obvious destruction in the model frame. The

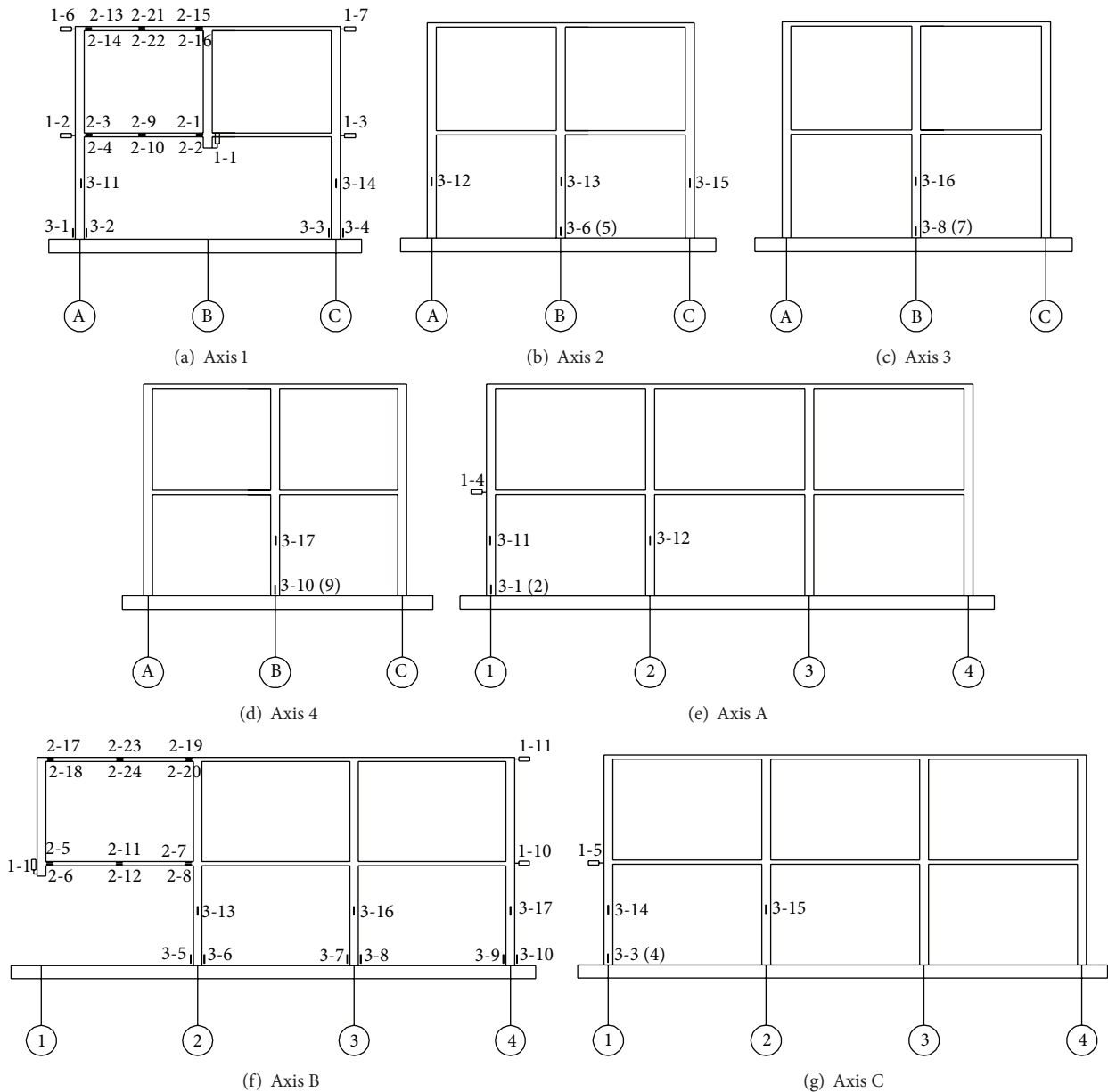


FIGURE 6: Details of testing setup and instrumentation. (Note: 1-1 to 1-11: displacement transducers; 2-1 to 2-24: steel strain gauges; 3-1 to 3-17: concrete strain gauges.)

AB segment is the elastoplastic or the start of the inelastic stage. The load is in a nonlinear relationship with the increase of displacement and the structural stiffness begins to decline at this stage. From the measured steel strains, it was observed that the longitudinal reinforcement at the ends of beams began to yield, indicating the formation of plastic hinges in the beams. And, most of the steel bars at the ends of beams had yielded at Point B. The BC segment is the plastic hinge stage. Plastic hinges at the ends of beams were all formed and the structure gradually became a plastic stress system. Serious concrete crushing was observed from Point B and the concrete spalling appeared at the later period in this stage. The progressive collapse resistance of the test frame

began to decrease after reaching its peak value of 256 kN. The CD segment is the catenary action stage. The flexural capacity of beams was almost lost at this stage. The tension cracks developed and penetrated through the compression zones, indicating the formation of the catenary mechanism in the beams. The measured strain in the upper steel bars changed to tension from compression, which indicates that the whole beam was in tension and the structure began to transfer load mainly by the steel bars. Because the beam-column joints at the top floor were unable to provide enough anchorage for the longitudinal steel bars in the beams, the bearing capacity of the structure at the catenary action stage decreased continuously with the increment of the vertical

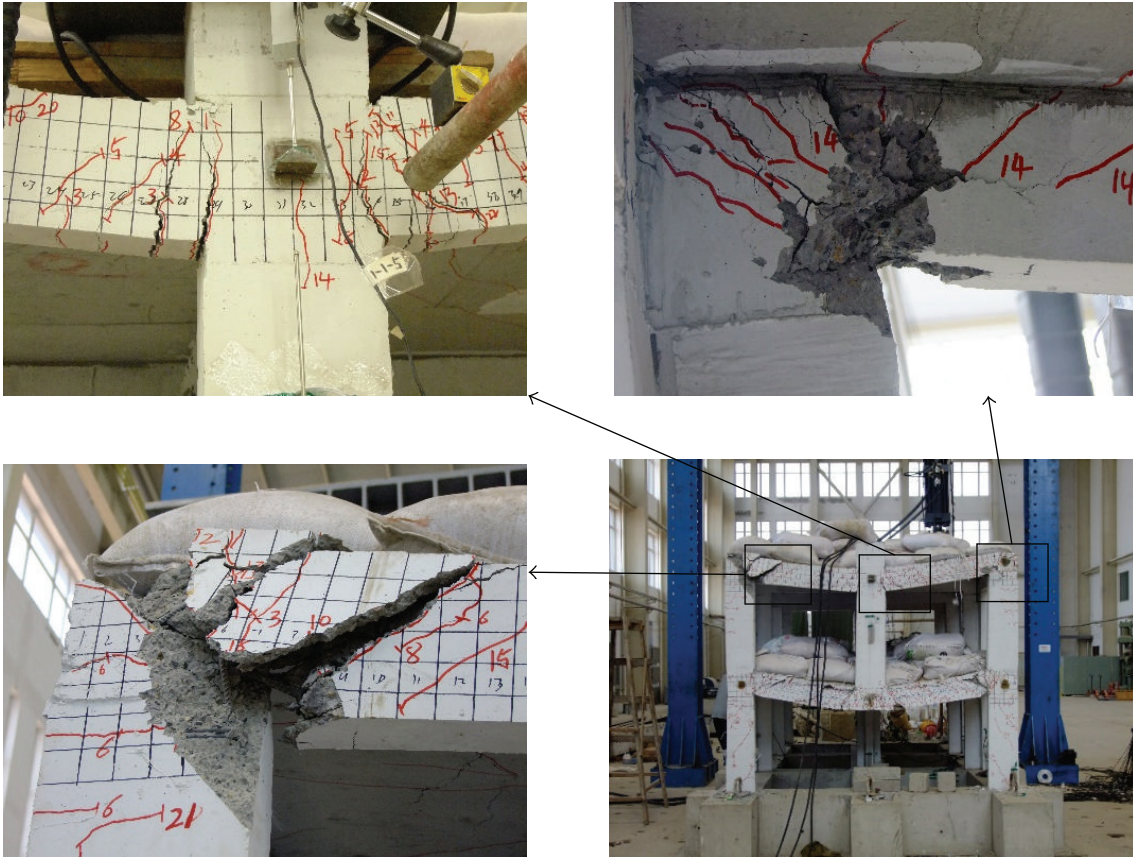


FIGURE 7: Failure modes of the test model.

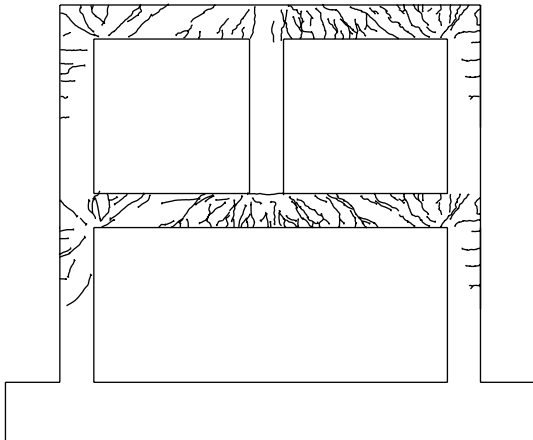


FIGURE 8: Crack pattern of model frame.



FIGURE 9: Crack on bottom surface of slab.

displacement. The structure entered an irreversible collapse process and the test was terminated since the serious damage of the beam-column joints at a vertical displacement of 170 mm (at Point D). The load transfer path was comparably more and the load variation was relatively stable without sudden drop of load during the catenary action stage due to the spatial action of the longitudinal frame beams and cast-in-place floor slabs. The frame beams and cast-in-place floors

significantly improved the ductility of the structure, leading to plastic failure during structural collapse, which played an important role in the delay and inhibition of structural collapse.

4.4. *Horizontal Displacement of Frame Column.* The relationship of the horizontal displacement of the adjacent columns, both at the ground floor and at the top floor, and the vertical displacement of the joint is shown in Figure 11(a). The increase of horizontal displacement indicates that the measurement point is moving away from the failed column,

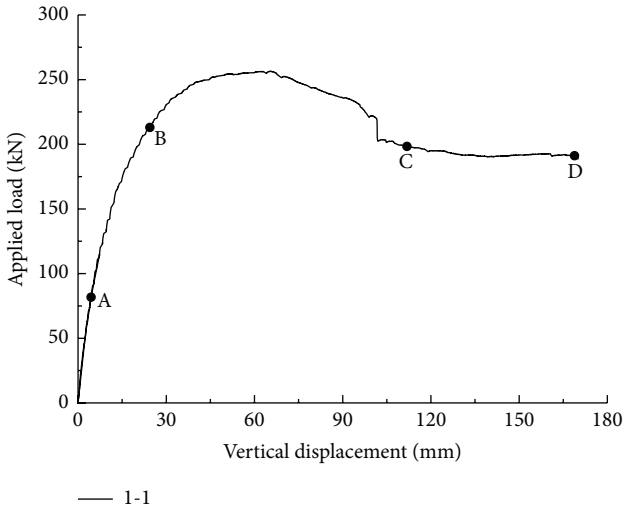


FIGURE 10: Applied load versus vertical displacement of the joint.

whereas the decrease means that it is moving towards the column. As exhibited in the figure, the adjacent columns moved outward during the initial loading stage under the influence of compressive arch action. The outward movement stopped after the vertical displacement exceeded about 65 mm with a maximum outward displacement of approximately 5 mm. With the development of plastic hinge in the frame beam, the compressive arch action disappeared, and the adjacent frame columns began to move toward their initial position. When the vertical displacement of the joint was about 135 mm, the adjacent frame columns moved back to their original position. As the vertical displacement increased, the adjacent frame columns tended to be pulled inward due to catenary action. The maximum inward displacement at the top of the adjacent frame columns was about 2 mm relative to the original position. During the whole experiment, the horizontal displacement of the top floor columns changed similarly to the ground floor columns, and the displacement of top floor columns was slightly higher after the frame entering the catenary action stage. When the vertical displacement exceeded 65 mm, cracking of the concrete at the top floor beam-column joint led to a larger value measured by the displacement transducers at the measurement point 1-6.

Figure 11(b) depicts the variation of the horizontal displacement along the longitudinal direction of the frame in B axis. At the early stage of the test, the columns far away from the failed column moved toward Axis 1. This was attributed to the fact that the side frames of Axis 4 were in tension under the combined action of the longitudinal frame beams and floor slabs during the time the failed column moved downward. The horizontal displacement of the top floor column was greater than that of the ground floor, and the displacement variation of the top floor frame was also more obvious. With the formation of plastic hinge and crush of concrete at the ends of B1-B2 beam and the floor slabs deactivated gradually since the development of cracks, the lateral force applied on the side frame declined, and the frame began to move outward (moving toward its initial position).

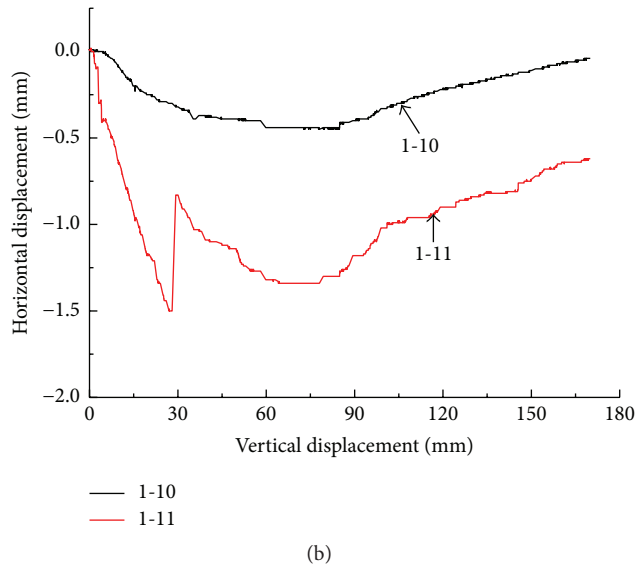
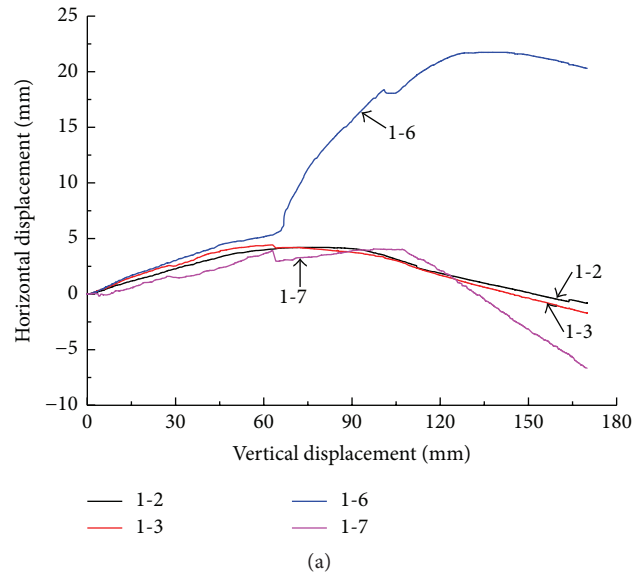


FIGURE 11: Relationship between the horizontal displacement and the vertical displacement of the joint.

During the test, the vertical displacement at the top of A4 column on the ground floor always changed around zero, indicating that the missing of B1 column had little influence on the corner column.

4.5. Strain of Steel Bars. The variation of the steel strain at the ends of A1-B1 beam as a function of the vertical displacement of the joint is shown in Figure 12. As depicted in the figure, the variation of the steel strains at the same cross sections at both the top and ground floors was similar. The steel strains in top floor beams were slightly greater than those in ground floor beams with a higher strain rate at corresponding sections. It is observed that most of the tensile reinforcement had yielded at the early stage of loading. The strain gauges on the tensile reinforcement fractured at a vertical displacement of about 30 mm. It is noted that the steel strain in measurement

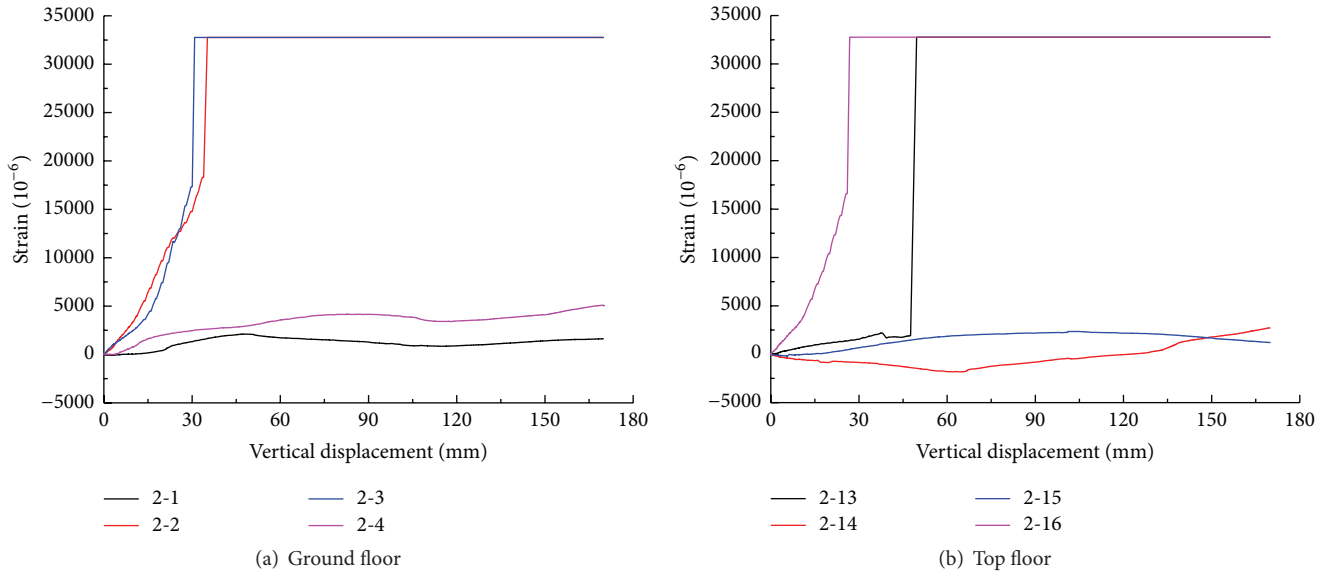


FIGURE 12: Strain response at the ends of beam A1-B1.

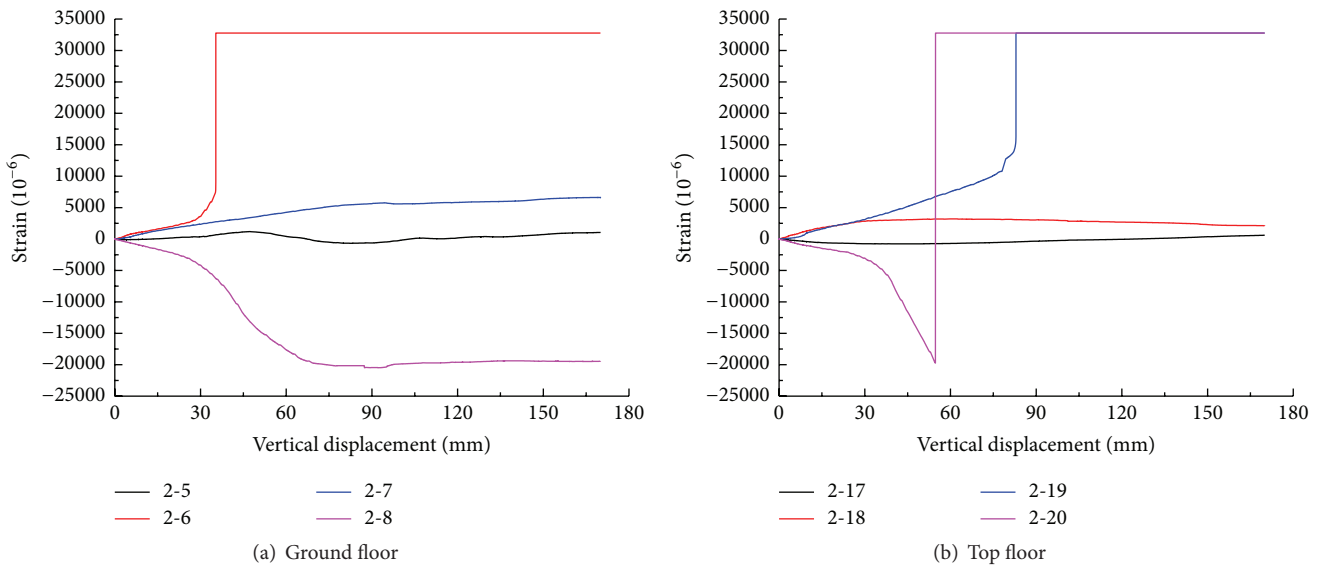


FIGURE 13: Strain response at the ends of beam B1-B2.

point 2-14 changed from compression to tension while the vertical displacement exceeded about 135 mm, which suggests the gradual forming of catenary action. Figure 13 shows the relationship of the steel strains at the ends of the longitudinal beam B1-B2 versus the vertical displacement of the joint. Steel bars at the bottom of the beam ends far away from the failed column were always in a compressive state indicating that the longitudinal frame beam connected to the failed column was in a cantilever state and the catenary action was unable to activate. The strain of this reinforcement monotonically increased and rapidly exceeded yielding strains with the crushing and spalling of concrete.

The relationship between the steel strains at the midspan of A1-B1 and B1-B2 beam and the vertical displacement of the

joint are displayed in Figure 14. At the early stage of loading, the compressive strain in the top steel bars at the midspan of the ground floor beam increased slowly indicating the formation of compressive arch action. The compressive strain decreased to zero at the vertical displacement of about 120 mm. Then, the frame beams changed to tension from the previous compression state, and the frame entered the catenary action stage. Meanwhile, the midspan section of the top floor beam was in tension all the time, indicating the restriction effect of frame beam on the columns. The horizontal displacement of the top floor columns should be two times that of the ground floor columns when the frame columns moved laterally with the column foot as the rotation center. However, the displacements of both the top floor and

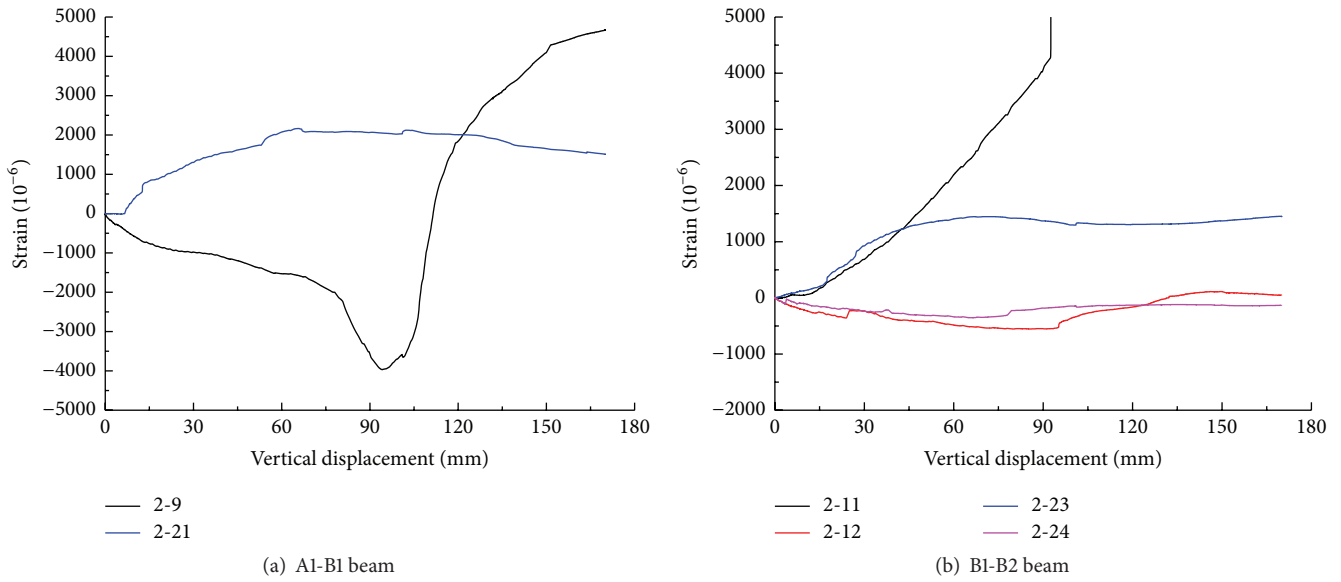


FIGURE 14: Strain response at the midspan of beam.

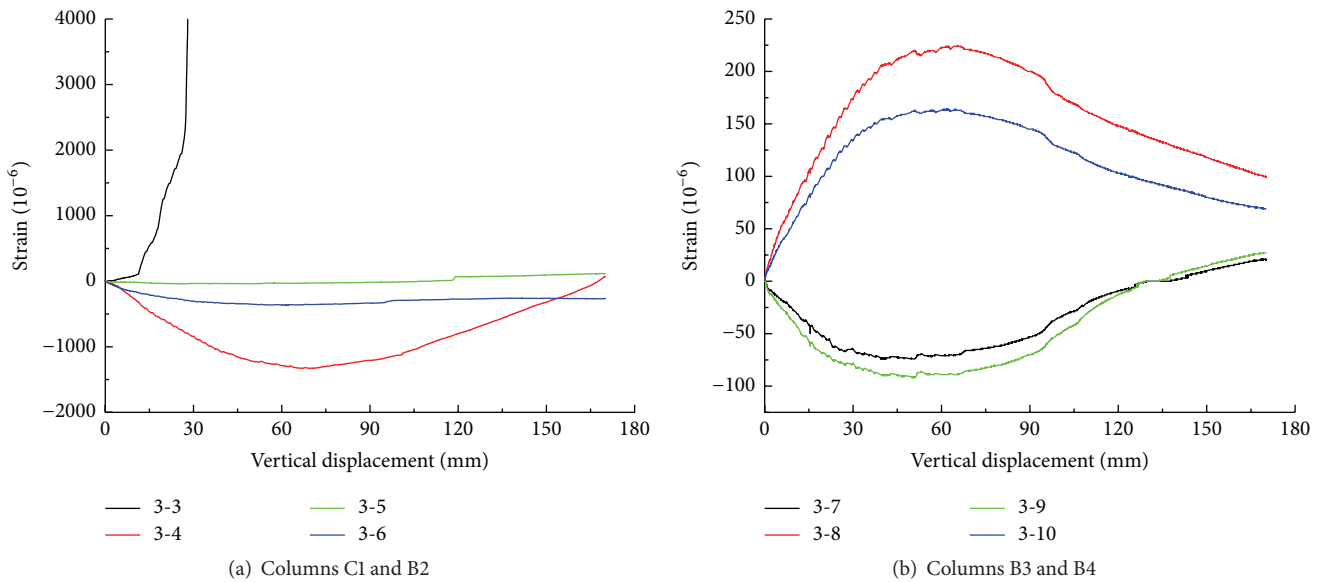


FIGURE 15: Concrete strain response at the bottom of frame column.

ground floor columns were close to each other under the spatial action of the superstructure, as shown in Figure 11(a), which suggested that the top floor beams limited the outward movement of the columns connected to it, leading to the tensile state of the whole beams. With the lateral displacement of the ground floor columns decreasing, the tensile strain in the top steel bars of the top floor beam also decreased. The frame beam B1-B2 was in a cantilever state and its load-carrying condition was relatively simple. The tensile strain in the top steel bars at the midspan increased slowly whereas the strain of the bottom steel bars remained small and tended to tension in the later stage.

4.6. Concrete Surface Strain. The variation of surface strain in concrete at the bottom of the ground floor columns as a

function of the vertical displacement of the joint is shown in Figure 15. The strain gauges were attached to the surface of concrete on two sides of the column feet along the bending direction, with a distance of 20 mm to the column foot. As shown in Figure 15(a), the compressive strains on the outside surface (the surface away from the failed column) of columns adjacent to the failed column reached their minimum values and began to increase after the vertical displacement reached approximately 65 mm. This is consistent with the trend observed for the horizontal displacements of ground floor columns previously, displayed in Figure 11(a), and confirms the existence of compressive arch action again. Because the strain gauge on the tensile side was located across a crack, the measured tensile strain in concrete increased rapidly and the strain gauges fractured while the displacement exceeded

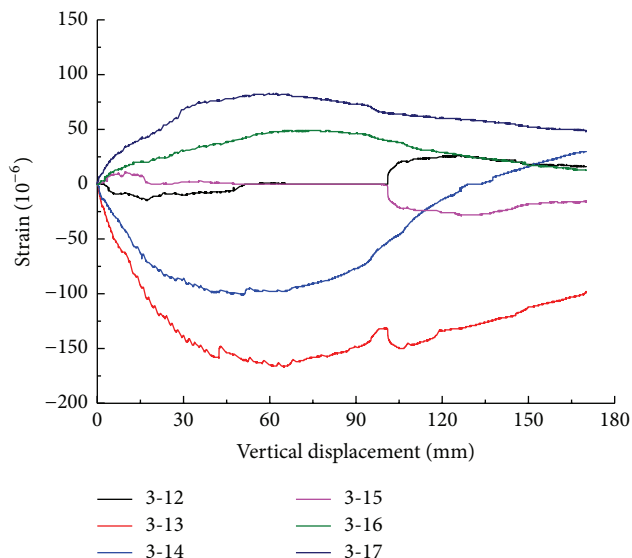


FIGURE 16: Concrete strain response at the middle of frame column.

30 mm. The concrete strain at the bottom of column far away from the failed column, as shown in Figure 15(b), changed gradually with tensile strain on the outside surface (the surface away from the failed column) and the compressive strain on the inside surface (the surface toward the failed column) under the combined action of moment and axial force. This was consistent with the variation of the frame's overall horizontal displacement along the long axis direction.

As illustrated in Figure 16, the compressive strain of concrete at the middle of C1 column, which was next to the failed column and in symmetry with the A1 column, along with the B2 column, reached its minimum value and began to increase gradually at a displacement of approximately 65 mm. This was because the internal force redistribution transferred the load carried by the failed column to the adjacent columns and increased the compressive stress of concrete. At the same time, the strains of other columns were in tension or approximate to zero with little variation due to the overall effect of the frame. The above results proved that, after the failure of the middle column at the ground floor, the load previously carried by the failed column was mainly transmitted to the frame columns adjacent to it; in contrast, the frame columns far away from the failed column share little. The internal force redistribution of the frame was primarily concentrated within the substructure adjacent to the failed column, with little influence on other components further away.

5. Finite Element Analysis

5.1. Finite Element Model. The OpenSees [18] platform was used in the simulations presented in this paper. The finite element model completely replicated the test model, in which the material properties and dimensions of the model were identical to the test model. The frame beam and

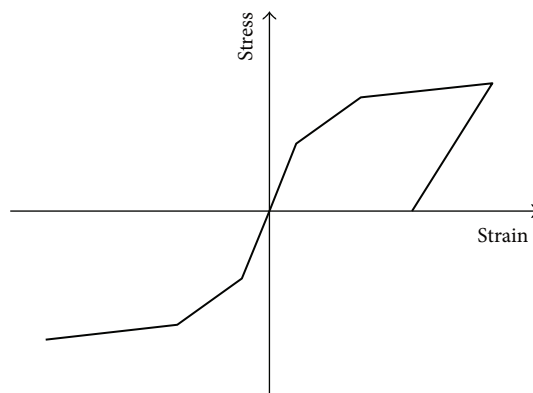


FIGURE 17: Stress-strain relationship of steel.

column components were simulated using the Force-Based Beam-Column Element, which was based on the iterative force-based formulation. A variety of numerical integration options can be used in the element state determination and encompass both distributed plasticity and plastic hinge integration. The resistance and tangent stiffness matrix of the whole element are integrated along the element length in accordance with Gauss-Lobatto integration on the basis of determining the resistance and stiffness matrix on the control section. The control section of the element was modeled by fiber element and the material properties of concrete and steel bars were, respectively, assigned to fibers. The finite element model was set up by beam elements with T-shaped or L-shaped sections, in which slabs were the flange of the frame beam, to consider the enhancement of slabs on beams. As shown in Figure 17, the steel reinforcing bars were modeled using the "Hysteretic Material" which allows the definition of trilinear behavior. The first branch was used to define the elastic response of the material, the second accounts for the hardening stage, while the final branch was specified with a negative slope up to bar rupture. The material used to define the concrete is the "Concrete02 Material," as shown in Figure 18, which utilizes the well-known Kent-Park model expanded by Scott et al. [19] in compression and linear elastic behavior in tension up to tension cracking followed by linear softening. There were two kinds of concrete: the core concrete (Confined Concrete) confined by stirrup and the cover concrete (Unconfined Concrete).

5.2. Comparison of Test and Analytical Results. The analytical results are compared with the experimental results in Figure 19. As can be seen from the figure, the calculated results are in good agreement with the experimental results in the initial stiffness and the whole bearing capacity. In general, the finite element model is accurate enough to conduct the progressive collapse analysis of RC frame structure with specially shaped columns, which can be used for further analysis in other scenarios such as frames of high rise buildings or a multibay frame.

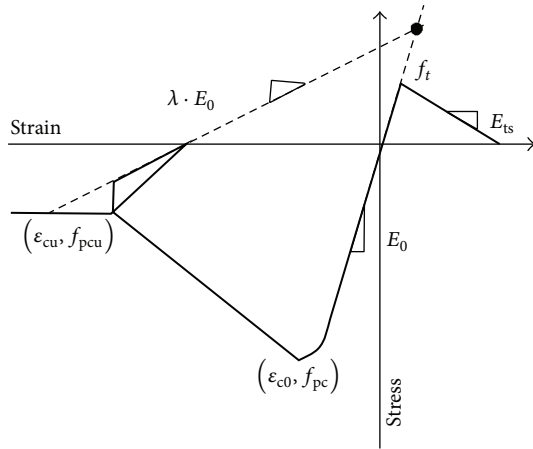


FIGURE 18: Stress-strain relationship of concrete.

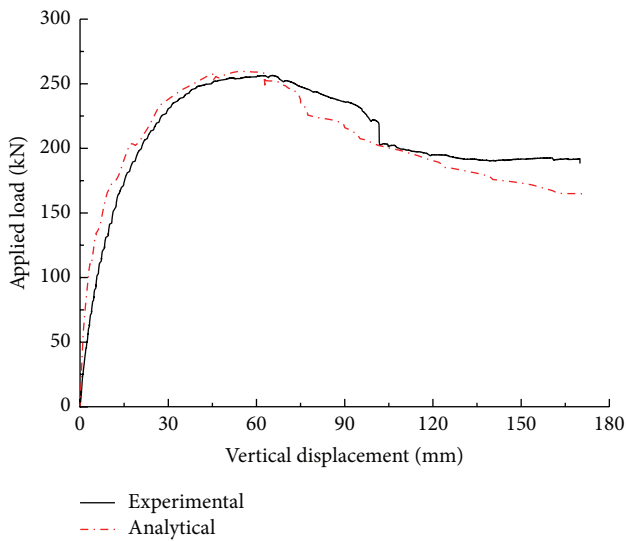


FIGURE 19: Applied load versus vertical displacement of the joint.

6. Discussion of Load Resisting Mechanisms

Figure 20 shows the transforming process of the load resisting mechanisms during the collapse of the frame with specially shaped columns. The transforming process can be summarized as a three-stage process: (1) a compressive arch action stage, in which compressive axial forces developed in the beams due to horizontal restraint at the beam ends, providing additional stiffness and load-carrying capacity; (2) a plastic hinge stage, in which flexural bending caused reinforcing bars to yield in tension and concrete to soften and crush in compression, causing a reduction in load-carrying capacity; and (3) a catenary action stage, in which tensile axial forces were mobilized in the beams as the deflection of the failed column exceeded the depth of the beam.

As shown in Figure 20, the structural deformation was small and minor cracks developed in the beams during the early stage of loading. These cracks, however, did not cause a significant decrease in the overall stiffness of the beams.

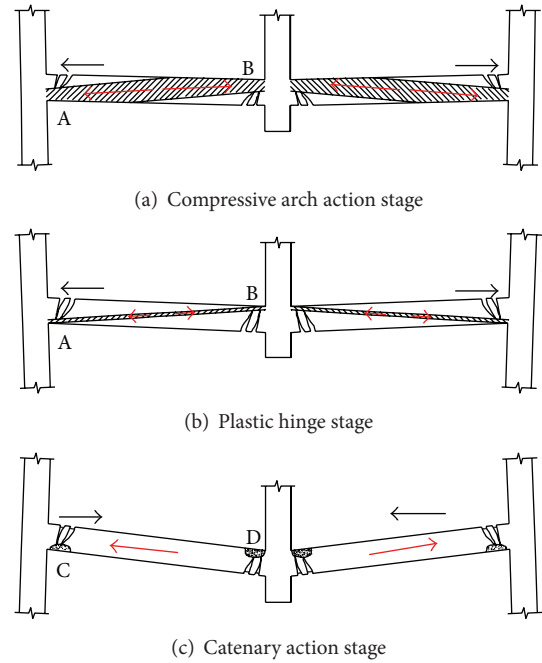


FIGURE 20: Load transfer mechanisms of frame with specially shaped columns.

At this stage, the beam ends near the failed column were in compression at the top and in tension at the bottom, while the beam ends far away from the failed column were in tension at the top and in compression at the bottom. A compressive arch formed within the beam due to the restraint provided by the end columns. The presence of beam axial compression enhances the flexural strength of a beam via standard flexural-axial interaction and, in turn, its resistance to progressive collapse. With the increase of the vertical displacement, the depth of the compression zone at the beam end decreased, and the height of the compression zone in the frame beam also decreased. The frame beam entered the plastic hinge stage. Pronounced degradation of the beam stiffness was observed at this stage because of yielding of the reinforcing bars. After reaching the initial peak load, the load began to drop with increasing vertical displacement. According to the study of Yu and Tan [11] and Bao et al. [20], the load will level off and start to increase again when the vertical displacement of the failed column exceeds the depth of the beam, and catenary forces will develop in the beams along with full-depth cracks. The development of catenary force was evidenced by tensile strains in reinforcing bars at midspan of beams. The catenary force is the total tension force in the cross section provided by the steel, which needs a good anchorage at the beam ends. However, anchorage for longitudinal steel bars depended mainly on the bond effect between the reinforcement and concrete. Specially shaped columns, whose width of column flanges and beams is imposed to be identical, are different from ordinary columns. Their limbs thickness is small, steel bars are dense, and the stress distribution is more complicated, leading to less bond strength of the steel bars and reinforced concrete in the

joints region. Moreover, the joints damaged before the frame beam during the test, which further weakened the bond anchorage of longitudinal steel bars. These factors lead to lack of anchorage for reinforcing bars at beam ends, which directly affected the development of the catenary forces. The bearing capacity of the structure at the catenary action stage decreased continuously rather than increasing. The frame failed due to the damage of joints with the failure load (191.6 kN) being 75% of the initial peak load (256.2 kN). That is, the ultimate bearing capacity of the frame with specially shaped columns was dominated by the flexural capacity of the beam while that of the frame with rectangular columns was dominated by the development of catenary action. For example, research results of Yu and Tan [11] show that the bearing capacities of the catenary action stage were 165% and 176% of flexural capacity with considering the presence of compressive arch action for specimens S1 and S2, respectively. This is a significant difference between the frame with specially shaped columns and the frame with rectangular columns.

7. Conclusion

Based on the observations and findings from the experimental study described in this paper, the progressive collapse performance and failure mechanism of frame with specially shaped columns were investigated, with the following conclusions obtained:

- (1) The frame finally failed due to the damage of the top floor beam-column joints. The damaged beam-column joints could not provide enough anchorage for longitudinal steel bars at the beam ends, which directly affected the development of the catenary forces. The beam-column joints were proved to be a weak area of the structure to resist progressive collapse and will require further enhancements during the design stage.
- (2) The collapse process of RC frame with specially shaped columns after one middle column removal experiences four distinct stages: elastic stage, elastoplastic stage, plastic hinge stage, and catenary action stage. Different from RC frame with rectangular columns, the redistribution of internal force for RC frame with specially shaped columns was mainly realized via the beam resisting mechanism and the compressive arch action in beams played an important role to improve the collapse-resistant capacity.
- (3) The redistribution of the load carried by the failed column occurred during the column failure. During the load redistribution, the load mainly transferred toward the adjacent columns, while little load was sustained by the columns further away. The redistribution of internal force in the frame was mainly concentrated in the components around the failed column, with little influence on the other components.

- (4) There was no sudden drop of load during the loading processing. The spatial connection action of the frame beams and cast-in-place slabs significantly increased the ductility of the structure and led to the plasticity failure of the structure during collapse. This could play an important role in the delay and inhibition of the structure collapse.
- (5) Progressive collapse performance of the reinforced concrete frame structures can be well predicted using the finite element model proposed in this paper. The finite element analysis method can be used for further analysis in other scenarios such as frames of high rise buildings or a multibay frame.

Conflict of Interests

The authors declare that there is no conflict of interests regarding the publication of this paper.

Acknowledgments

The work presented in this paper was funded by the National Natural Science Foundation of China (no. 51178304) and the Specialized Research Fund for the Doctoral Program of Higher Education of China (no. 20120032120055), which are gratefully acknowledged.

References

- [1] ASCE, *Minimum Design Loads for Buildings and Other Structures*, American Society of Civil Engineers, Reston, Va, USA, 2006.
- [2] P. Kotsovinos and A. Usmani, "The World Trade Center 9/11 disaster and progressive collapse of tall buildings," *Fire Technology*, vol. 49, no. 3, pp. 741–765, 2013.
- [3] GSA, *Progressive Collapse Analysis and Design Guidelines for New Federal Office Buildings and Major Modernization Projects*, US General Service Administration, Washington, DC, USA, 2003.
- [4] European Committee for Standardization, *EN 1991-1-7:2006, Eurocode 1: Actions on Structures. Part 1-7: General Actions—Accidental Actions*, European Committee for Standardization, Brussels, Belgium, 2006.
- [5] Office of the Deputy Prime Minister, *BS 5950-1. The Building Regulations 2000: Part-A: Schedule 1: A3, Disproportionate Collapse*, Office of the Deputy Prime Minister, London, UK, 2004.
- [6] M. Sasani and J. Kropelnicki, "Progressive collapse analysis of an RC structure," *The Structural Design of Tall and Special Buildings*, vol. 17, no. 4, pp. 757–771, 2008.
- [7] M. Sasani, M. Bazan, and S. Sagioglu, "Experimental and analytical progressive collapse evaluation of actual reinforced concrete structure," *ACI Structural Journal*, vol. 104, no. 6, pp. 731–739, 2007.
- [8] W.-J. Yi, Q.-F. He, Y. Xiao, and S. K. Kunnath, "Experimental study on progressive collapse-resistant behavior of reinforced concrete frame structures," *ACI Structural Journal*, vol. 105, no. 4, pp. 433–439, 2008.

- [9] J. Kim and J. Yu, "Analysis of reinforced concrete frames subjected to column loss," *Magazine of Concrete Research*, vol. 64, no. 1, pp. 21–33, 2012.
- [10] Y. Su, Y. Tian, and X. Song, "Progressive collapse resistance of axially-restrained frame beams," *ACI Structural Journal*, vol. 106, no. 5, pp. 600–607, 2009.
- [11] J. Yu and K.-H. Tan, "Experimental and numerical investigation on progressive collapse resistance of reinforced concrete beam column sub-assemblages," *Engineering Structures*, vol. 55, pp. 90–106, 2013.
- [12] S. L. Yap and B. Li, "Experimental investigation of reinforced concrete exterior beam-column subassemblages for progressive collapse," *ACI Structural Journal*, vol. 108, no. 5, pp. 542–552, 2011.
- [13] T.-C. Wang and X.-H. Zhang, "Frame property of unequal storey height with specially shaped columns under cyclic loading," *Journal of Central South University of Technology*, vol. 17, no. 6, pp. 1364–1369, 2010.
- [14] T. Wang, X. Liu, and H. Zhao, "Experimental study of the seismic performance of L-shaped columns with 500 MPa steel bars," *The Scientific World Journal*, vol. 2014, Article ID 105826, 11 pages, 2014.
- [15] *GB 50010-2010. Code for Design of Concrete Structures*, China Architecture & Building Press, Beijing, China, 2010, (Chinese).
- [16] JGJ, "Technical specification for concrete structures with specially shaped columns," JGJ 149-2006, China Architecture & Building Press, Beijing, China, 2006 (Chinese).
- [17] T. Wang, Q. Chen, H. Zhao, and L. Zhang, "Investigation on dynamic effects of frame with specially shaped columns subjected to column failure," *Journal of Vibroengineering*, vol. 17, no. 5, pp. 2455–2470, 2015.
- [18] F. McKenna, G. L. Fenves, and M. H. Scott, *Open System for Earthquake Engineering Simulation*, University of California, Berkeley, Calif, USA, 2000.
- [19] B. D. Scott, R. Park, and M. Priestley, "Stress-strain behavior of concrete confined by overlapping hoops at low and high strain rates," *ACI Journal Proceedings*, vol. 79, no. 1, pp. 13–27, 1982.
- [20] Y. Bao, H. S. Lew, and S. K. Kunnath, "Modeling of reinforced concrete assemblies under column-removal scenario," *Journal of Structural Engineering*, vol. 140, no. 1, Article ID 04013026, 2014.

Research Article

Experimental Design and Validation of an Accelerated Random Vibration Fatigue Testing Methodology

Yu Jiang,¹ Gun Jin Yun,² Li Zhao,² and Junyong Tao¹

¹Science and Technology on Integrated Logistics Support Laboratory, College of Mechatronics Engineering and Automation, National University of Defense Technology, Changsha, Hunan 410073, China

²Department of Civil Engineering, The University of Akron, Akron, OH 44321, USA

Correspondence should be addressed to Yu Jiang; jiangyu@nudt.edu.cn

Received 13 May 2015; Revised 17 July 2015; Accepted 22 July 2015

Academic Editor: Gilbert-Rainer Gillich

Copyright © 2015 Yu Jiang et al. This is an open access article distributed under the Creative Commons Attribution License, which permits unrestricted use, distribution, and reproduction in any medium, provided the original work is properly cited.

Novel accelerated random vibration fatigue test methodology and strategy are proposed, which can generate a design of the experimental test plan significantly reducing the test time and the sample size. Based on theoretical analysis and fatigue damage model, several groups of random vibration fatigue tests were designed and conducted with the aim of investigating effects of both Gaussian and non-Gaussian random excitation on the vibration fatigue. First, stress responses at a weak point of a notched specimen structure were measured under different base random excitations. According to the measured stress responses, the structural fatigue lives corresponding to the different vibrational excitations were predicted by using the WAFO simulation technique. Second, a couple of destructive vibration fatigue tests were carried out to validate the accuracy of the WAFO fatigue life prediction method. After applying the proposed experimental and numerical simulation methods, various factors that affect the vibration fatigue life of structures were systematically studied, including root mean squares of acceleration, power spectral density, power spectral bandwidth, and kurtosis. The feasibility of WAFO for non-Gaussian vibration fatigue life prediction and the use of non-Gaussian vibration excitation for accelerated fatigue testing were experimentally verified.

1. Introduction

Many engineering structures usually undergo vibration loading. Fatigue is the most commonly encountered type of failure for structures operating under dynamic loading. Vibration fatigue is more complicated than general cyclic fatigue. To ensure the reliability and safety of structures during the operation, we need timely validation of long-term durability of engineering structures under their service vibration environment. This is usually done by the laboratory vibration tests. However, operational life under normal vibration conditions could be too long that the laboratory vibration tests at those levels would not be possible for many structures and materials. Accelerated testing provides time and cost saving compared with testing at normal conditions. Therefore it is necessary to perform accelerated vibration testing in a laboratory environment, which in terms of loading is considerably more severe than the operative one. Then the operative life duration is estimated by relating the structural

fatigue life tested in the laboratory condition by a proper scaling factor.

In recent years, experimental methods for accelerated vibration fatigue testing are continuously under development. The work by Allegri and Zhang [1] addressed the usage of inverse power laws in accelerated fatigue testing under wide-band Gaussian random loading. The aim was not at predicting an absolute value of fatigue life but assessing the relative accumulation of fatigue damage. Özsoy et al. [2] proposed an accelerated life testing approach for aerospace structural components. A closed-loop system driven by power spectral density profiles was employed to run the constant amplitude resonance test. By changing the test durations and accordingly the mission profile amplitudes, a simple equation was proposed which relates accelerated test durations with the equivalent alternating stresses. Shires [3] discussed the time compression (test acceleration) of broadband random vibration tests. Conventionally, the test level is accelerated from the root mean acceleration and an

assumed power constant ($k = 2$) is applied. The Miner-Palmgren hypothesis of accumulated fatigue is used to reassess the potential error in test severity, which shows a substantially reduced sensitivity to the value of k depending on the distribution of actual vibration intensities around the time-compressed test intensity. Xu et al. [4] developed a method for extracting the information on the frequency of the events expected in the service life from a time series based on wavelet analysis, clustering, and Fourier analysis. The identified events and their corresponding data are used to generate the accelerated durability testing PSD profiles, which can be directly applied as the driven profile in the lab test. Yun et al. [5] developed a vibration-based closed-loop high-cycle resonant fatigue testing system. To minimize the testing duration, the test setup was designed for a base-excited multiple-specimen arrangement driven in a high-frequency resonant mode, which allows completion of fatigue testing in an accelerated period. Česnik et al. [6] proposed an improved accelerated fatigue testing methodology based on the dynamic response of the test specimen to the harmonic excitation in the near-resonant area with simultaneous monitoring of the modal parameters. The measurements of the phase angle and the stress amplitude in the fatigue zone were used for the real-time adjustment of the excitation signal according to the changes in the specimen's modal parameters. Pothula et al. [7] addressed applicability of various theories for estimation of failure time in normal usage and accelerated condition for Gaussian random vibration testing. Another issue addressed was whether application of damping material makes any difference. Experimentally observed failure time in random vibration for both bare and damped beams under random vibration was compared, and the exponent in terms of both g^2/Hz and G_{rms} for accelerated testing was obtained for bare and damped beams. Vibration fatigue analysis of a cantilever beam under white noise random input using several vibration fatigue theories was performed by Eldogan and Cigeroglu [8]. Fatigue life calculations by utilizing time domain (rainflow counting method) and frequency domain methods were repeated for different damping ratios and the effect of damping ratio was studied. Fatigue tests were performed on cantilever beam specimens and fatigue life results obtained experimentally were compared with that of in-house numerical codes. It was observed that the fatigue life result obtained from Dirlik method is considerably similar to that of the rainflow counting method.

The vibration loading in the above studies is limited to sinusoidal loading with constant amplitude or Gaussian random loading with alternating amplitude, and the random loading fatigue damage calculation is based on the assumption of Gaussian distribution. However, the dynamic loading shows non-Gaussianity in some practical applications, such as the ground vibration generated by wheeled vehicles travelling over irregular terrain, atmospheric turbulence for the aerospace sector, or wind pressure fluctuations on building envelopes [9]. Because traditional Gaussian random vibration test signals cannot accurately represent the non-Gaussian vibration signal with high-peak characteristics seen in the real-life use of many structures, the latest MIL-STD-810G standard also requires test engineers to “ensure that

test and analysis hardware and software are appropriate when non-Gaussian distributions are encountered” (refer to Method 525 on Page 514.6A-5 in literature [10]). For this purpose, the non-Gaussian vibration controller has just been developed by few manufacturers (such as Econ Corporation and Vibration Research Corporation) in recent years. Since the basic purpose of the non-Gaussian vibration controller is to simulate the real non-Gaussian vibration environment of some products, it is meaningful to carry out further experimental research on how to use non-Gaussian vibration in accelerated fatigue testing.

Generally, conservative or incorrect results will be obtained if non-Gaussianity is ignored during fatigue damage estimation and fatigue life prediction. Although in recent years there have been few studies on the non-Gaussian random vibration fatigue theory, the studies described in literature [11–14] are directly based on non-Gaussian response without considering non-Gaussian excitation and structural dynamics characteristic. However, in the laboratory vibration test, the main consideration is the vibration excitation profile. Therefore, there is a “gap” between theoretical research and engineering applications and it is necessary to establish a link between the Gaussian or non-Gaussian vibration excitation and structural vibration fatigue life, which will facilitate the design and statistical analysis of the accelerated vibration test.

Fatigue damage as a result of random loading can be assessed in either the time or frequency domain. In the time domain, the rainflow counting method is universally accepted for random vibration fatigue analysis. WAFO (Wave Analysis for Fatigue and Oceanography) is a toolbox of MATLAB routines for statistical analysis and simulation of random waves and random loads [15]. The main purpose of WAFO is for scientific research, and thus the aim of WAFO is not to contain all the features of the commercial software. Nevertheless, it is also widely used in industry. So far, there has been no report on WAFO applied to non-Gaussian vibration fatigue analysis. Therefore, this paper is not about proposing another method for predicting fatigue life. Rather, the objectives of this study are as follows: (1) develop a hybrid test strategy for the accelerated random vibration fatigue test, which can generate a design of the experimental test plan, significantly reduce test times and costs, and avoid complex finite element modeling and verification process and the risk of inaccuracies caused by modeling; (2) verify the feasibility of WAFO for non-Gaussian vibration fatigue life prediction; (3) experimentally and numerically investigate all the factors affecting the structure random vibration fatigue life; (4) explore the possibility of non-Gaussian vibration for accelerated fatigue testing.

2. Theoretical Analysis and Damage Model

2.1. Damage Model for Gaussian Random Vibration Excitation. Firstly the analysis starts from the most basic description of the material fatigue in terms of S - N curve. Typically ideal mathematical expression for S - N curve is written as follows:

$$N = cS^{-b}, \quad (1)$$

where S denotes the stress amplitude, N denotes the stress cycles resulting in the failure, and b and c are the constant fatigue parameters that depend on the material.

On the base of the famous Miner cumulative fatigue damage criterion, the fatigue damage under a joint action of different amplitudes of stress is

$$D = \sum_i \frac{n_i}{N_i}, \quad (2)$$

where n_i is the number of cycles applied at fixed stress amplitude S_i , N_i is the number of cycles the material can withstand at applied fixed stress amplitude S_i , and D is cumulative fatigue damage (fatigue failure generally considered to occur at $D = 1$).

Substituting (1) into (2), the following is obtained:

$$D = \sum_i \frac{n_i}{cS_i^{-b}} = \sum_i \frac{n_i}{c} S_i^b. \quad (3)$$

For continuous time histories of random stress, (3) can be written in the form of the following integral [16]:

$$D = v_0^+ T \int_0^\infty \left[\frac{p(S)}{(cS^{-b})} \right] dS = \frac{v_0^+ T}{c} \int_0^\infty p(S) S^b dS, \quad (4)$$

where T is the total time of exposure to the random vibration excitation, $p(S)$ denotes the probability density function of random stress response on the specimen, v_0^+ is the average number of the zero upcrossings per unit time in the stress time history.

The specimen under the vibration test generally can be approximated as a linear system and the excitation generated by the vibration test equipment can be regarded as the input of the system. As the frequency response characteristics of the specimen are similar to a narrow-band filter, it can be considered that, under stationary Gaussian random excitation (either broad-band or narrow-band), the stress response of the specimen is close to the stationary narrow-band Gaussian distribution. When the random stress response approximates a stationary narrow-band Gaussian distribution, according to the random-process theory, the amplitude probability density function of the stress $p(S)$ has the following Rayleigh form [16]:

$$p(S) = \frac{S}{\sigma_s^2} e^{-S^2/2\sigma_s^2}, \quad (5)$$

where σ_s is the RMS value of the stress (i.e., standard deviation). Substituting (5) into (4) and doing the integration, the following equation could be obtained:

$$D = \frac{v_0^+ T}{c} \left[\sqrt{2}\sigma_s \right]^b \Gamma \left[1 + \frac{b}{2} \right]. \quad (6)$$

Herein Γ represents the Gamma function.

Engineering practice shows that the damping ratio ξ of a general structure is usually much less than 1, for example, a small value of 0.05 or less. According to the literature [17],

on the assumption of a linear system with small damping, the approximate calculation formula for σ_s is

$$\sigma_s \approx k \sqrt{\frac{G_a(f_1)}{\pi f_1 \xi}}, \quad (7)$$

where f_1 is the first-order natural frequency of the specimen, ξ denotes the equivalent damping ratio (generally assumed as $\xi \leq 0.1$), k represents proportional constant related to the specimen, and $G_a(f_1)$ is the magnitude of the acceleration PSD of the input vibration excitation at the natural frequency f_1 of the specimen.

Under the assumption of small damping, $v_0^+ \approx f_1$. Then substitute (7) into (6) to obtain

$$\begin{aligned} D &\approx \frac{f_1 T k^b}{c} \left[\frac{2G_a(f_1)}{\pi f_1 \xi} \right]^{b/2} \Gamma \left[1 + \frac{b}{2} \right] \\ &= k_1 T \left[\frac{G_a(f_1)}{\xi} \right]^{b/2} f_1^{(1-b/2)}, \end{aligned} \quad (8)$$

where $k_1 = (k^b/c)[2/\pi]^{b/2}\Gamma[1+b/2]$. For the deterministic specimen material, k_1 is a proportional constant.

The fatigue failure is generally regarded to occur when $D = 1$. The structural vibration fatigue life T_G subject to Gaussian random vibration excitation can be obtained according to (8):

$$T_G = \frac{f_1^{(b/2-1)}}{k_1} \left[\frac{\xi}{G_a(f_1)} \right]^{b/2}. \quad (9)$$

Considering the commonly used engineering material, typically b has a value range of 4–25. From (9) it can be seen that, on the Gaussian random vibration excitation, when the structure dynamics parameters such as f_1 and ξ are fixed, the structural vibration fatigue life T_G is inversely proportional to the magnitude $G_a(f_1)$ of the PSD of the Gaussian random vibration excitation at the first natural frequency of the structure. As the increase (or decrease) of $G_a(f_1)$, T will undergo an exponential decay (or growth).

According to (9), the structural vibration fatigue lives under two different Gaussian random acceleration excitations are achieved, respectively, as

$$T_{G1} = \frac{f_1^{(b/2-1)}}{k_1} \left[\frac{\xi}{G_{a1}(f_1)} \right]^{b/2}, \quad (10)$$

$$T_{G2} = \frac{f_1^{(b/2-1)}}{k_1} \left[\frac{\xi}{G_{a2}(f_1)} \right]^{b/2}. \quad (11)$$

According to (10) and (11), the following can be obtained:

$$\frac{T_{G1}}{T_{G2}} = \left[\frac{G_{a2}(f_1)}{G_{a1}(f_1)} \right]^{b/2}. \quad (12)$$

Obviously, (12) above is the inverse power-law model in the literatures, which is often used to describe the accelerated

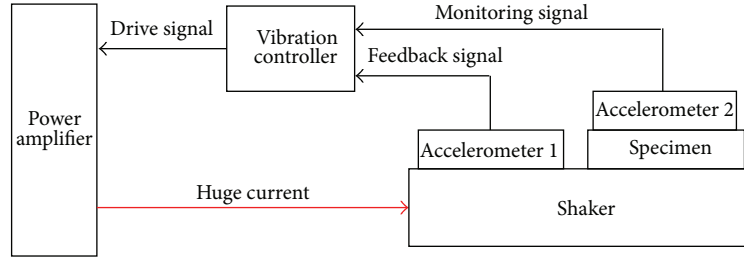


FIGURE 1: Closed-loop vibration fatigue test system configuration.

vibration test. From the derivation above, as long as the structural FRF of a system is similar to a narrow-band filter (actually this condition is applicable in most engineering structures) and the structural random response is subject to a Gaussian distribution, then it is able to use (12) to model the vibration acceleration test. Thus, (12) applies only to describe the accelerated Gaussian random vibration fatigue test.

2.2. Damage Model for Non-Gaussian Random Vibration Excitation. The following will continue to discuss the damage model for non-Gaussian random vibration excitation. When the random stress response approximates a stationary narrowband non-Gaussian distribution, it is possible to add non-Gaussian correction factor λ based on (8) to describe the impact of the kurtosis value of the stress response on the cumulative vibration fatigue damage:

$$D = \lambda k_1 T \left[\frac{G_a(f_1)}{\xi} \right]^{b/2} f_1^{(1-b/2)}. \quad (13)$$

It is obvious that the non-Gaussian correction factor λ is proportional to the kurtosis value of stress response. Furthermore, the kurtosis value of stress response depends on the kurtosis value of vibration excitation and the kurtosis transfer function of the structure. However, according to the existing random vibration theory, it is difficult to obtain the kurtosis transfer function similar to frequency response function by theoretical analysis. Therefore, this paper will study the influence factors for the kurtosis value of the stress response or the non-Gaussian correction factor λ by experimental method, which will be described in detail in Section 4.1.

3. Accelerated Random Vibration Fatigue Test System

3.1. Design of Random Vibration Fatigue Test System. The vibration fatigue test system consists of vibration table, power amplifiers, vibration controller, and accelerometers. As shown in Figure 1, the vibration controller used is a VT-9008 vibration controller from Econ Corporation, which contains up to 12 control modules. In addition to the traditional sine, Gaussian random, and shock tests, it is capable of generating a non-Gaussian random vibration signal with the specified power spectrum density and kurtosis and can be

TABLE 1: Material properties for Al 6061-T6 aluminum.

Mass density	Young's modulus	Poisson's ratio	Yield strength
2,700 kg/m ³	68.9 GPa	0.33	276 MPa

used to study the non-Gaussian random vibration fatigue. The vibration table (Brüel & Kjær's V406 series) is able to output a maximum acceleration of 100 g and a frequency range of 5–9000 Hz. The model of the two accelerometers is Dytran's 3030B4 with one providing the feedback signal to the controller and the other monitoring the vibration response of the specimen. The sensitivities of these two accelerometers were 9.86 mv/g and 9.71 mv/g, respectively.

3.2. Design of Test Specimen and Fixture. In order to complete the vibration fatigue test within an appropriate time, the following notched specimen and supporting fixture were designed as shown in Figures 2 and 3. Four holes at one end of the specimen are used for mounting it on the shake table. On the other end, it was also designed with two holes: one for the installation of additional mass to accelerate the process of vibration fatigue failure and another hole for the installation of accelerometer to acquire the vibration response of the specimen. The material of specimen is Al 6061-T6 aluminum, due to its excellent mechanical properties and wide application in aerospace, machinery parts, structural engineering, modern architecture and transportation, and so forth. Material properties of Al 6061-T6 aluminum are shown in Table 1.

In order to obtain dynamic stress response, Vishay Micro-Measurements & SR-4 strain gauges were used to measure the strain signal at the dangerous point, that is, the notch in the specimen. Strain gauges have a resistance value of $350 \pm 0.6\%$ (Ohms) and a gauge factor of $2.125 \pm 0.5\%$. Strain gauges in the form of quarter-bridge were mounted on the specimen as shown in Figure 4.

High-precision strain measurement system (Model 8000-8-SM) from Vishay Micro-Measurements Corporation is used for the acquisition, analysis, and processing of the strain signal. The strain apparatus communicates with the measurement software StrainSmart on the host computer using the network interface and is able to acquire and analyze 8-channel strain signals simultaneously. The sampling frequency of each channel has 5 options of 1000/500/200/100/10 Hz and up to 1 kHz. The strain measurement system has a self-calibration

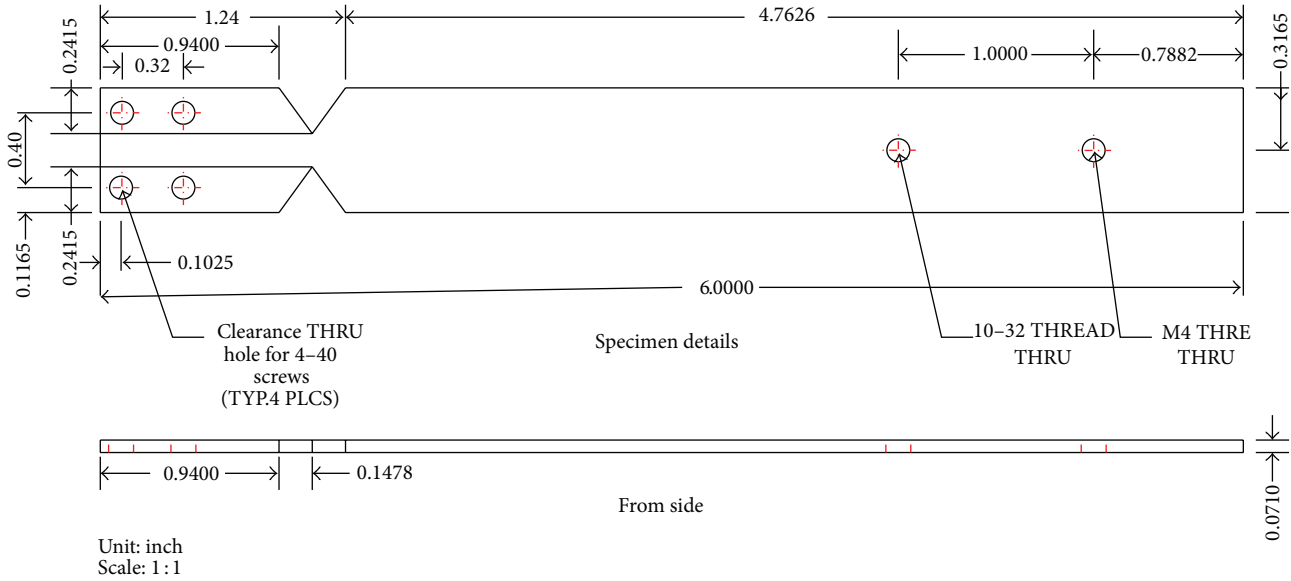


FIGURE 2: Specimen dimension.

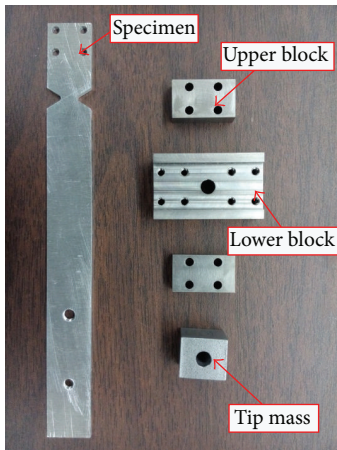


FIGURE 3: Fixture and specimen.

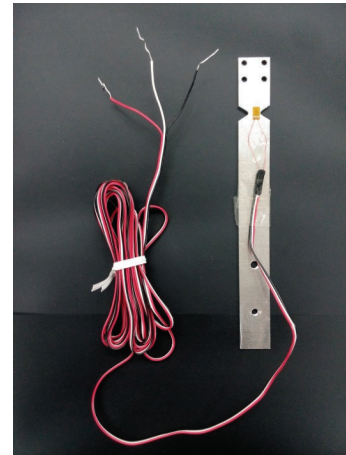


FIGURE 4: Specimen and strain gauge.

function. The strain measurement ranges up to $\pm 310000 \mu\epsilon$ and measurement resolution is up to $0.5 \mu\epsilon$.

4. Experimental Design of Accelerated Random Vibration Fatigue Test Plan

4.1. Design Considerations for Non-Gaussian Random Vibration Fatigue Test. One of the objectives in this paper is to investigate the influence factors associated with non-Gaussian random vibrational excitation on the vibration fatigue life of a structure. Based on the random vibration theory, the systematic response depends on two factors, that is, the vibration excitation and the dynamic transfer characteristics of structure. Once the material, size, shape, and mounting are fixed, the dynamic characteristics are

determined correspondingly. In order to ensure the credibility of the results of accelerated test, structural dynamics are normally kept same as service environment during the vibration test. Therefore, it is preferable to achieve accelerated results by changing some properties of the random vibration excitation. A complete description of the related parameters in the random vibrational excitation is necessary to be worked out before the experimental design.

The most common parameter used to describe the random vibration is power spectral density (PSD). However, PSD is not able to adequately portray all the characteristics of the random vibration. For example, with the same PSD and root mean square (RMS), the random signals can have completely different properties of the probability density distribution, as shown in Figure 5. Because the higher-order

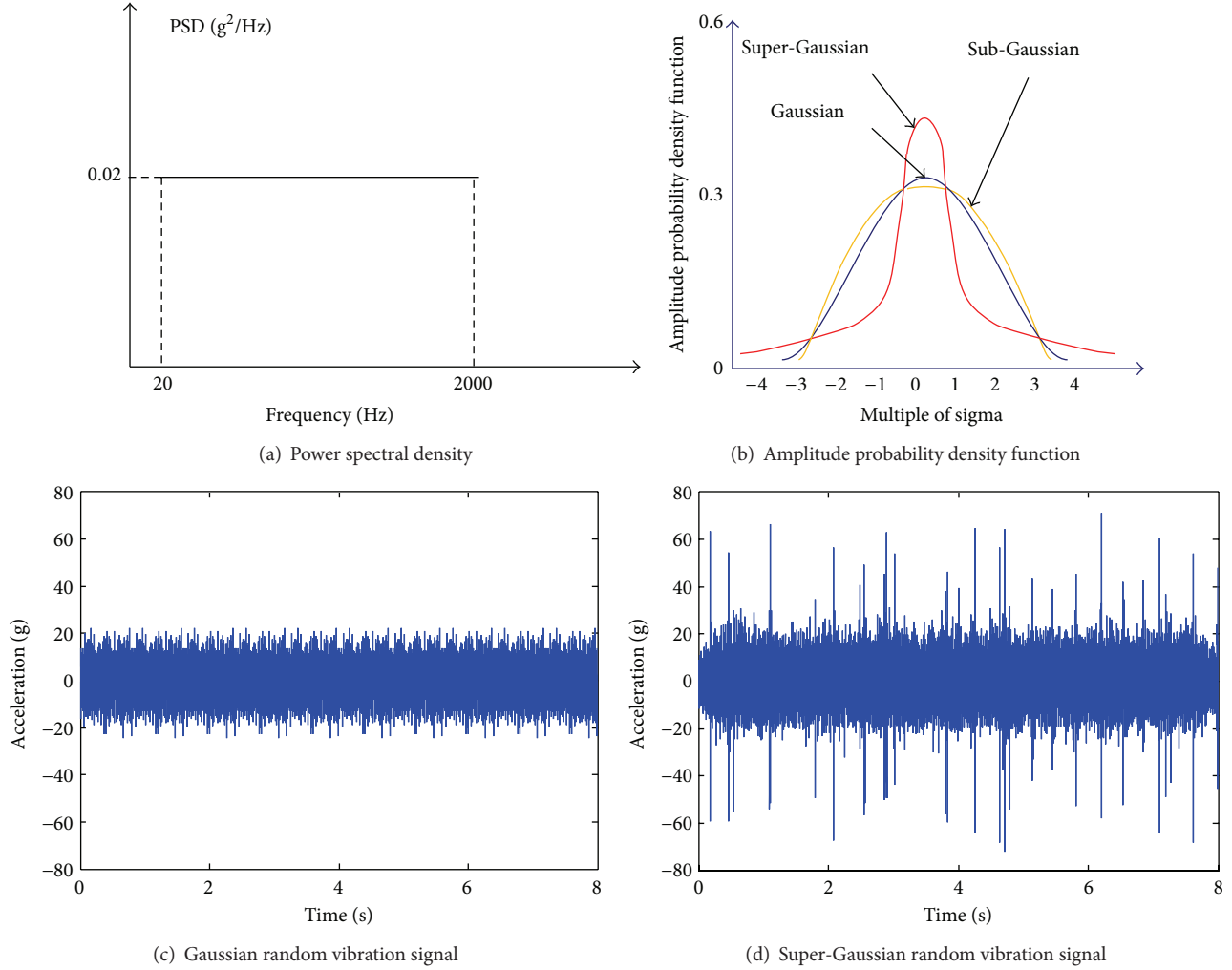


FIGURE 5: Gaussian and super-Gaussian vibration signals with the same PSD.

statistics over the second order are constantly zero for a Gaussian random process, only using the PSD function or self-correlation function can fully describe the characterization of the Gaussian random process. In addition to the PSD function, higher-order statistics (above the second order) also need to be supplied for a complete description of a non-Gaussian random process. Skewness S and kurtosis K are the two parameters widely used in engineering to describe non-Gaussian random process X , defined as follows:

$$S = \frac{E[X - E(X)]^3}{\{E[X - E(X)]^2\}^{3/2}}, \quad (14)$$

$$K = \frac{E[X - E(X)]^4}{\{E[X - E(X)]^2\}^2}.$$

Skewness and kurtosis values of a Gaussian random process are 0 and 3, respectively, while the kurtosis value for a non-Gaussian random process certainly is not equal to 3 and the skewness value may or may not be equal to 0.

The skewness is used to describe the magnitude of a random process deviation from the symmetric probability density distribution. The nonzero skewness indicates the asymmetric distribution of the probability density. Kurtosis is a parameter describing the trailing probability density distribution of a random process, which not only can be used to distinguish between Gaussian and non-Gaussian random process, but also further classifies the non-Gaussian random process into sub-Gaussian and super-Gaussian random processes where sub-Gaussian random process $K < 3$ and super-Gaussian random process $K > 3$. The non-Gaussian vibration signals in engineering are usually super-Gaussian signals with high-peak characteristics.

In this paper, the five parameters used to fully describe a random vibration excitation are RMS, PSD, power spectral bandwidth, kurtosis, and skewness. Since most of the vibration signals in engineering and laboratory simulations are often symmetric, this paper focuses on investigating the influence of the first four parameters on the damage accumulation in vibration fatigue process.

TABLE 2: Group A.

Number of test profile	Test profile parameters					
	Lower frequency (Hz)	Upper frequency (Hz)	PSD bandwidth (Hz)	Acceleration PSD magnitude (g^2/Hz)	G_{rms} (g)	Kurtosis
A1	15	215	200	0.031	2.50	3
A2	15	115	100	0.031	1.80	3
A3	15	65	50	0.031	1.25	3

TABLE 3: Group B.

Number of test profile	Test profile parameters					
	Lower frequency (Hz)	Upper frequency (Hz)	PSD bandwidth (Hz)	Acceleration PSD magnitude (g^2/Hz)	G_{rms} (g)	Kurtosis
B1	15	65	50	0.031	1.25	3
B2	15	65	50	0.020	1.0	3
B3	15	65	50	0.010	0.7	3

TABLE 4: Group C.

Number of test profile	Test profile parameters					
	Lower frequency (Hz)	Upper frequency (Hz)	PSD bandwidth (Hz)	Acceleration PSD magnitude (g^2/Hz)	G_{rms} (g)	Kurtosis
C1	15	65	50	0.02	1.0	3
C2	15	65	50	0.02	1.0	5
C3	15	65	50	0.02	1.0	7

TABLE 5: Group D.

Number of test profile	Test profile parameters					
	Lower frequency (Hz)	Upper frequency (Hz)	PSD bandwidth (Hz)	Acceleration PSD magnitude (g^2/Hz)	G_{rms} (g)	Kurtosis
D1	15	115	100	0.02	1.4	5
D2	15	65	50	0.02	1.0	5
D3	15	35	20	0.02	0.63	5

For this purpose, four groups of vibration fatigue tests were designed and listed in Tables 2–5.

In Table 2, Group A aims to investigate the influence of RMS and bandwidth of Gaussian random vibration excitation on the vibration fatigue.

In Table 3, Group B aims to investigate the influence of the PSD magnitude of Gaussian random vibration excitation at the structural first-order natural frequency on the vibration fatigue.

In Table 4, Group C is designed to investigate the influence of kurtosis value of a non-Gaussian random vibration excitation on the vibration fatigue.

In Table 5, Group D is designed to investigate the influence of the bandwidth of a non-Gaussian random vibration excitation on the vibration fatigue.

It can be seen that there is the same cross-sectional test parameter in every two adjacent groups such as A3 and B1, B2 and C1, and C2 and D2. The benefits of this sort of design are that the comparative analysis can be implemented by taking advantage of the test data in the previous group and it can also significantly reduce the total number of tests and sample size. In the following, a hybrid test method of actual test and numerical simulation will be presented that is used to derive test groups A, B, C, and D.

4.2. Hybrid Test Strategy for Accelerated Random Vibration Fatigue Test. According to the experimental design above, the test setup was eventually built as shown in Figure 6.

In order to save test time and ensure the validity of the test results, an idea of combining random vibration fatigue

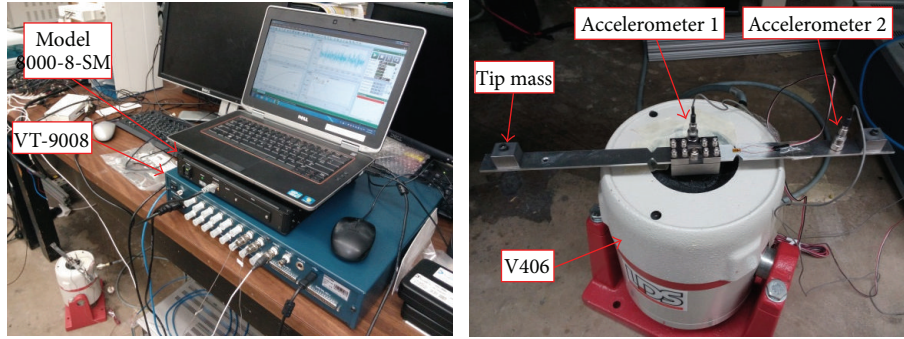


FIGURE 6: Experimental setup for accelerated random vibration fatigue test.

test and numerical simulation was proposed in this paper. Specifically the detailed idea and implementation process are introduced as follows.

Step 1 (determine the appropriate mass block by diagnostic tests). The first set of experiments were carried out by applying A1 from the experimental profile of Group A as the basic excitation condition of the shake table. Specimens were tested by adding three different mass blocks, that is, 15 g, 20 g, and 30 g, at one end of the specimen aiming to obtain the corresponding time duration until fatigue fracture. It was found that only using the mass block of 20 g can obtain the best result. Also the length of the test time can be controlled in 1 to 2 hours, while 15 g mass block takes too long and 30 g mass block too short, and therefore ultimately 20 g mass was selected.

Step 2 (determine the natural frequency and damping ratio of the specimen through sine sweep test). Sine sweep test was implemented in a frequency range of 5–2000 Hz. Two accelerometers installed on the shake table and the specimen were used to acquire the vibration excitation and the response signals, respectively, for the calculation of the frequency response function. They were also used to determine the structural natural frequency of the specimen and damping ratio to ensure the frequency band of random vibration excitation covering the first-order natural frequency and fully exciting the resonant modes of the specimen to generate vibration fatigue. Figure 7 shows the frequency response function of the entire specimen structure.

It can be seen that there is only one specimen resonant frequency of 26.270 Hz within the frequency range of 5–2000 Hz. According to the literature [5], when the vibration fatigue cracks occur to a structure, its natural frequency generally decreases slightly; however, the decline is not very significant and is generally only a few Hz. Therefore, the four previously designed vibration excitation bands of 15–35 Hz, 15–65 Hz, 15–115 Hz, and 15–215 Hz can guarantee covering its natural frequency in the whole testing process. Therefore it does not require to continuously track changes of the resonant frequency of the structure as the conventional sinusoidal vibration fatigue test and the random excitation is also much closer to the real vibrational service environment

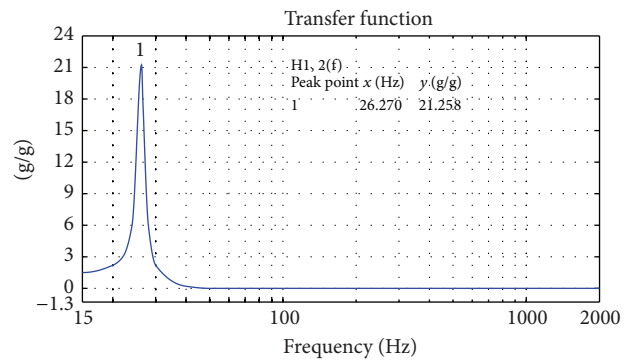


FIGURE 7: Frequency response function from sweep sine test.

of the specimen. Obviously it is an advantage of the random vibration fatigue testing. According to the measured frequency response function, the structural damping ratio was estimated as 2.52% using the half-power bandwidth method.

Step 3 (strain signal acquisition test (nondestructive vibration test)). From Section 2.1, the experimental program designed for the fatigue test, there are totally 9 different testing profiles if the two neighboring coincident experimental profiles are removed. Taking into account the dispersion characteristics of the fatigue life, in order to make the test results more credible, four specimens were tested for each test profile. In the meantime, the four test results were averaged to a final fatigue life. In this way, it requires $9 \times 4 = 36$ trials, which will be very time consuming. In order to tackle this problem, two strategies were used: The first one is if the fatigue failure times of the first three specimens are concentrated with a small dispersion, it is unnecessary to test the fourth specimen under the same fatigue test condition. The second one is the use of a combination of experimental tests and numerical simulations to actually reduce the number of destructive fatigue tests, that is, acquiring strain signals from the tests under nine different profiles at the stress concentration point under different random excitations by using strain apparatus and strain gauges and further obtaining the stress response signals according to the material properties; then, based on the stress response, using WAFO numerical analysis

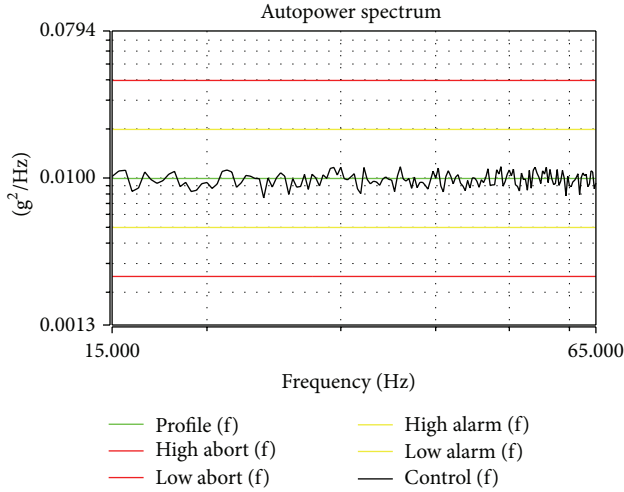


FIGURE 8: Test profile parameters (B3).

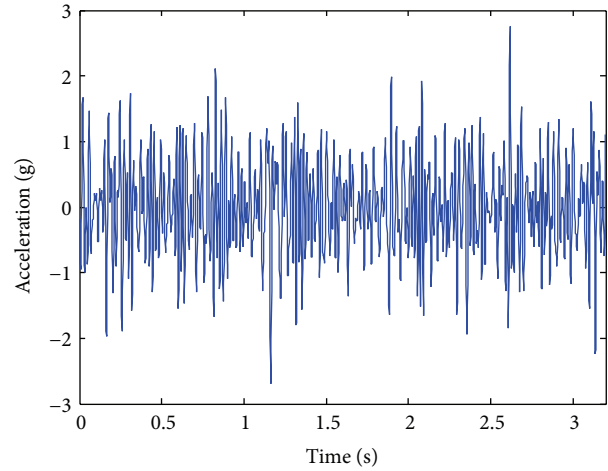


FIGURE 9: Vibration excitation signal under test profile B3.

techniques to predict the structural fatigue life under different vibration test conditions which also provides a reference for the choice of test conditions to do the next vibration fatigue test; further selecting several test profiles having a predicted fatigue life within 3 hours to validate the effectiveness of the WAFO method under different random loadings. Once the effectiveness of WAFO method in predicting structural vibration fatigue life is fully validated, it is able to only carry out the vibration fatigue tests under a test profile with a predicted life within 3 hours while only strain signals acquired for the test profile have a predicted life of more than 3 hours. Therefore, the overall fatigue test time can be significantly reduced.

It should be noted that, in the acquisition process of test strain signals, a large measurement error can occur as the time accumulation of the vibration test and the likely damage of the specimen and the strain gauges. Thus once it is found that the measurement strain data becomes abnormal, the strain gauges and specimens are needed to be replaced timely. In this test, there were 5 strain gauges and 5 specimens used to ensure the accuracy of measurement strain data under different loading conditions. Figure 8 shows a schematic sectional view of test profile B3 and Figure 9 illustrates a time domain excitation signal according to B3. The acceleration response signal was measured by the monitoring accelerometer and shown in Figure 10. Figure 11 shows the strain response signal measured at the stress concentration point of the structure by the strain apparatus. Figure 12 shows the stress response signal obtained on the base of strain signals and material properties of the specimen.

After obtaining the stress response signal at the dangerous point, the material fatigue *S-N* curves or related parameters of the structure are still required for the application of WAFO method in predicting the structural vibration fatigue life. In this paper, the fatigue properties of Al 6061-T6 aluminum alloy discussed in the literature [18] are adopted and show a good agreement with the actual test results.

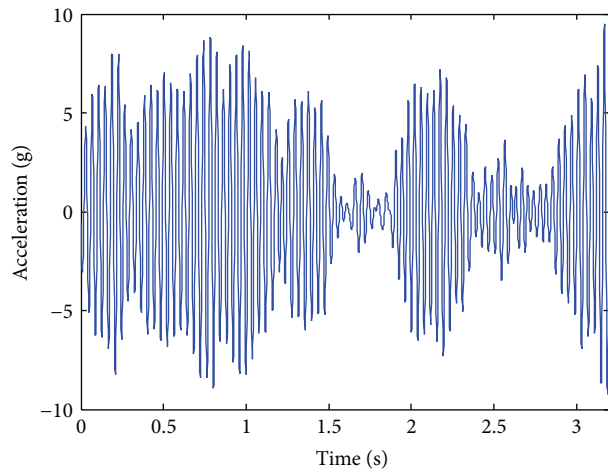


FIGURE 10: Vibration response signal under test profile B3.

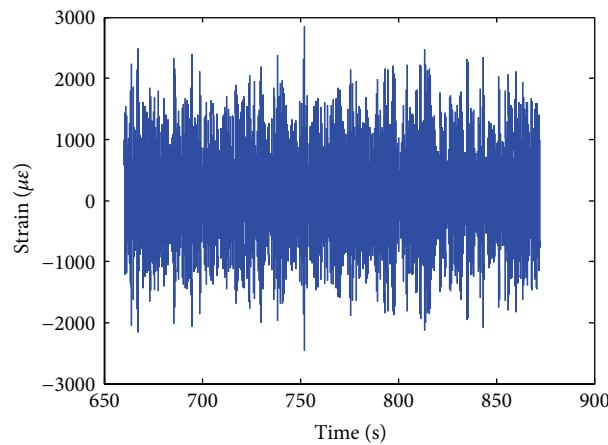


FIGURE 11: Strain signal under test profile B3.

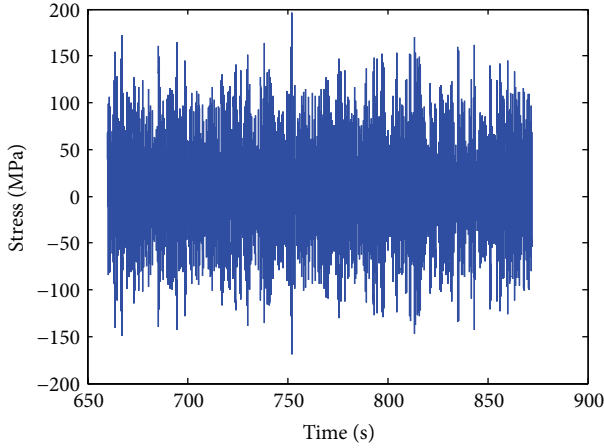


FIGURE 12: Stress signal under test profile B3.

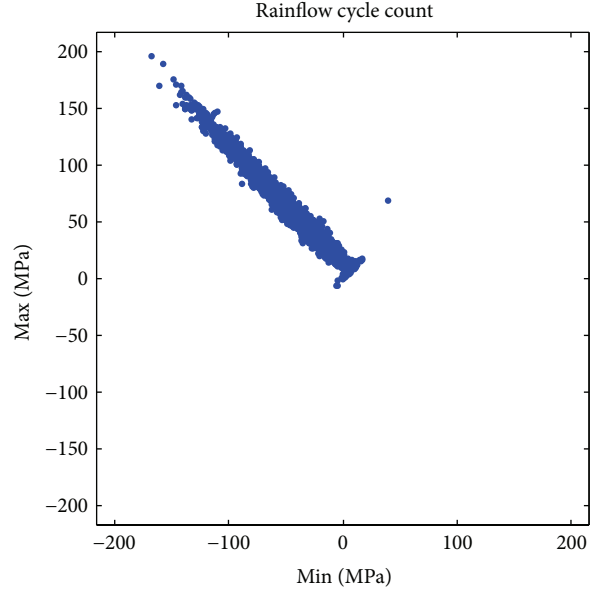


FIGURE 14: Rainflow cycle counts for stress signals in Figure 12.

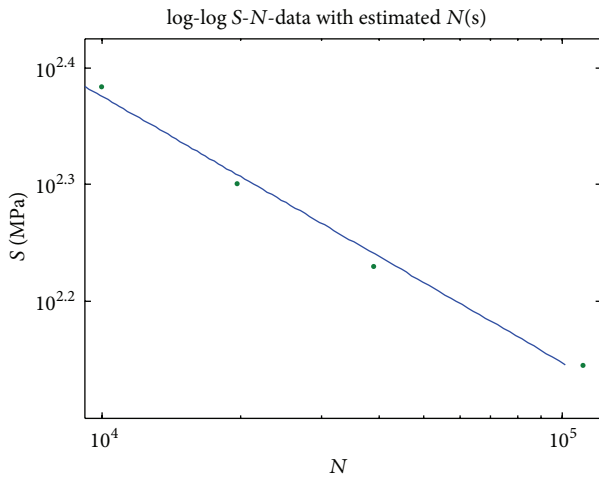


FIGURE 13: S-N curve for Al 6061-T6.

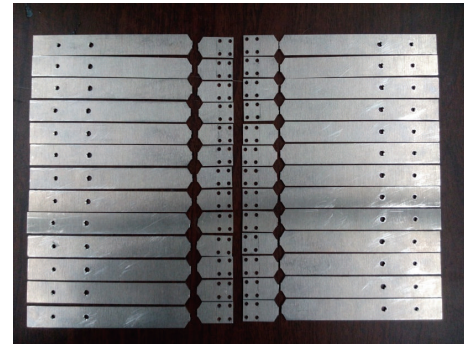


FIGURE 15: Fatigue specimens broken during this experiment.

The double logarithmic fatigue S-N curve used in this study is illustrated in Figure 13. Figure 14 shows results from the rainflow fatigue counting method by applying WAFO to the stress response sequence shown in Figure 12. According to the rainflow counting results and material fatigue S-N curves, the corresponding fatigue life is easy to be predicted.

Step 4 (vibration fatigue failure test (destructive vibration fatigue test)). According to the stress response signals obtained from the acquired strain signals in the last step, WAFO numerical analysis techniques are employed to predict the fatigue life of the structure. It was found that only fatigue lives corresponding to test profiles B3 and D1 are relatively longer, that is, 14.86 and 3 hours, respectively, while in other tests the corresponding fatigue lives of the profiles are all less than 3 hours. Therefore, in order to fully validate accuracy of the WAFO method in the prediction of structural vibration fatigue life, the vibration fatigue failure test was carried out to the other 7 testing profiles except B3 and D1;

in other words, the test continued until the specimens are completely fatigue-failed. Finally, 23 specimens were actually used to conduct the destructive fatigue test. If we consider the 3 broken specimens in the diagnostic test, a total of 26 specimens undertook fatigue fracture failure, as shown in Figure 15.

In the destructive fatigue test, in addition to the natural frequency drop with the fatigue crack initiation mentioned in other literature, another interesting phenomenon of natural frequency bifurcation was also observed, as shown in Figure 16. When the specimen has fatigue cracks, the first natural frequency declines slightly and then the curve of the transfer function changes from “single peak” into the neighboring “Twin Peaks.” The amplitude of the transfer function at each peak is also smaller than the initial amplitude. Further, once the “Twin Peaks” phenomenon occurs, the complete fatigue fracture of the specimen will take place around 5 minutes later. Therefore, this phenomenon can be used as an

TABLE 6: Test matrix and results.

Test group	Number of test profile	n	T (minute)	T_e (minute)	T_p (minute)
A	A1	4	64; 60; 62; 66	63	68
	A2	4	77; 64; 55; 58	63.5	55
	A3 (B1)	3	77; 52; 53	61	69
B	B1 (A3)	3	77; 52; 53	61	69
	B2 (C1)	3	155; 133; 145	144	156
	B3		Strain acquisition test		892
C	C1 (B2)	3	155; 133; 145	144	156
	C2 (D2)	3	102; 117; 110	110	106
	C3	3	59; 73; 87	73	90
D	D1		Strain acquisition test		180
	D2 (C2)	3	102; 117; 110	110	106
	D3	3	93;74;89	85	88

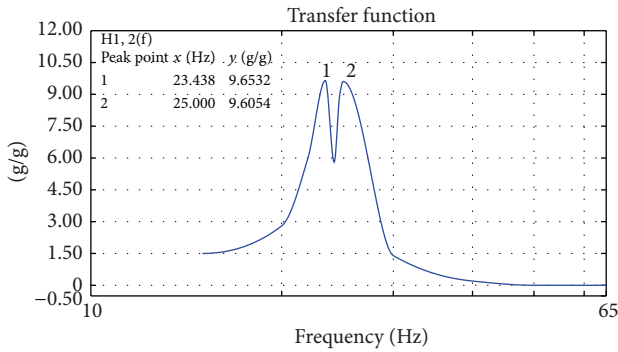


FIGURE 16: Bifurcation of natural frequency when fatigue cracks were developed.

effective means of real-time monitoring of the fatigue damage of the specimen in the vibration fatigue test process.

5. Experimental Results and Discussions

Detailed test results are shown in Table 6, where n is the number of tests conducted at a test profile level; T is the real experimental time until fatigue broken failure; T_e is its mean; T_p is the predicted fatigue life by WAFO method based on the strain acquisition test results.

First, it is good to review the effectiveness of WAFO numerical analysis method. As can be seen from Table 6, the fatigue life T_e obtained through the actual fatigue test was close to the fatigue life T_p predicted by WAFO and they matched very well. It illustrates that WAFO fatigue life prediction method is applicable to both the Gaussian and non-Gaussian random vibration fatigue and can be used as an effective means of vibration fatigue simulation test. Next, the test results from each group are analyzed to reveal all possible impact factors for the structural vibration fatigue.

From the test results of Group A, though RMS values and bandwidths of A1, A2, and A3 are different, there is

no significant difference between the test result T_e and the simulation result T_p due to the same PSD magnitude designated at first-order natural frequency of the structure.

This shows that, considering the structural random vibration fatigue, as long as the first-order natural frequency of the structure is included in the excitation band and the PSD magnitude of a Gaussian random vibration excitation at the first-order natural frequency of the structure is kept consistent, the RMS value and excitation bandwidth of Gaussian random vibration have a limited impact on the vibration fatigue life. This is easy to understand and interpret as the magnitude of the structural random response depends on the energy distribution of the excitation at the resonance frequency of the structure.

The results of Group B further confirmed the above rules. Though B1, B2, and B3 have the consistent bandwidth, the vibration fatigue life of the structure has undergone a significant change by changing the PSD magnitude of Gaussian random vibration excitation at the first-order natural frequency of the structure to alter the excitation RMS.

The test results of Group C showed that the kurtosis value of non-Gaussian random vibration excitation also has a significant impact on the structural vibration fatigue life. With the same PSD and RMS, the higher the kurtosis value of non-Gaussian random vibration excitation is, the shorter the structural vibration fatigue life is. This supports the fact that the use of non-Gaussian vibration excitation for accelerated fatigue tests is possible.

Results from Group D showed that the bandwidth of non-Gaussian random vibration excitation also has a significant impact on the structural vibration fatigue life. Under the condition of the same kurtosis value and the same PSD magnitude, the narrower the bandwidth of non-Gaussian random vibration excitation is, the shorter the structural vibration fatigue life is. This reveals that the use of non-Gaussian vibration excitation for accelerated fatigue tests must consider the bandwidth factor.

In summary, a test strategy for the accelerated random vibration fatigue test is developed based on the hybrid

method of actual test and numerical simulation. Detailed steps are introduced as follows:

- (1) The characteristics of random vibration environment of engineering structures under actual service conditions should be measured and analyzed including both the PSD and kurtosis value in order to ensure whether a non-Gaussian distribution is applicable. The structural dynamics also need to be tested and analyzed including natural frequency, damping ratio, and other parameters.
- (2) Based on the PSD of service vibration environment obtained in the last step, the corresponding Gaussian vibration environment is firstly reproduced on the shake table and the same or similar mounting of the structure is also applied for the purpose of ensuring that the structural dynamic parameters such as the natural frequency and damping ratio are consistent with the reality. According to the design idea of the test profile in Group B, the PSD is increased gradually while the stress response is measured at the critical points in the structure under different vibrational excitation until it is close to the material yield limit.
- (3) If the actual vibration environment of the structure is subject to a non-Gaussian distribution, the corresponding non-Gaussian vibration environment is supposed to be reproduced on the shake table. In accordance with the design idea of the test profile in Group C, the kurtosis value of the random vibration excitation is increased gradually. Simultaneously the stress response is measured at the critical points in the structure under different vibrational excitation until it is close to the material yield limit.
- (4) On the base of all the stress response measured in the second and third steps, WAFO numerical simulation analysis is used to predict the vibration fatigue life of the structure under different loading conditions. According to the predicted fatigue life, a few test profiles with shorter life are selected to carry out the actual vibration fatigue destructive tests. Also the results of destructive fatigue tests are used to validate and correct the results of WAFO method.

6. Conclusions

In this paper, a closed-loop system for the random vibration fatigue test was set up. The experimental procedure of the vibration fatigue test was carefully designed and combined with the WAFO fatigue simulation analysis. Finally a variety of influence factors on the structural vibration fatigue life were systematically studied in a significantly reduced time. The related main conclusions are listed as follows:

(1) For the Gaussian random vibration, the biggest factor affecting the structural vibration fatigue life is the PSD magnitude of a Gaussian random vibration excitation at the first-order natural frequency of the structure. On the other hand, the RMS value, bandwidth, and other factors of the

Gaussian random vibration excitation have a small effect on the structural vibration fatigue life.

(2) For the non-Gaussian random vibration, in addition to the PSD magnitude at the first-order natural frequency, both the bandwidth and kurtosis value of non-Gaussian random vibration excitation have a significant effect on the stress response of the structure and further significantly affect the structural vibration fatigue life.

(3) The WAFO-based fatigue life prediction method is applicable to both the Gaussian and non-Gaussian random vibration fatigue, in good agreement with the actual test results, and can be used as an effective means of vibration fatigue simulation test.

(4) A new test strategy for the accelerated Gaussian/non-Gaussian random vibration fatigue test is developed based on the hybrid method of the actual test and numerical simulation, which avoids the complex finite element modeling and verification process (especially in the case of a complex structure) and the risk of inaccuracies in the model. Also it avoids the long testing time caused by the complete fatigue destructive test and reduces the sample size and, at the same time, ensures the accuracy and the effectiveness of the assessment results, which can be used to assess the long-term durability and fatigue reliability of engineering structures under random vibration environment.

Conflict of Interests

The authors declare that there is no conflict of interests regarding the publication of this paper.

Acknowledgments

The authors would like to proclaim sincere gratitude to all those who contributed to the success of the research project reported in this study. The authors gratefully acknowledge the financial support provided by National Natural Science Foundation of China (50905181). The authors appreciate the experimental support provided by Ph.D. candidate Ali Imani Azad (from Intelligent Structural Engineering and Health Monitoring Laboratory at The University of Akron). Without his help, the experimental work would not have been accomplished in time. The authors also would like to thank research technician Bill Wenzel (from College of Engineering, The University of Akron) for his strong support in manufacturing and machining of materials.

References

- [1] G. Allegri and X. Zhang, "On the inverse power laws for accelerated random fatigue testing," *International Journal of Fatigue*, vol. 30, no. 6, pp. 967–977, 2008.
- [2] S. Özsoy, M. Çelik, and F. S. Kadioglu, "An accelerated life test approach for aerospace structural components," *Engineering Failure Analysis*, vol. 15, no. 7, pp. 946–957, 2008.
- [3] D. Shires, "On the time compression (test acceleration) of broadband random vibration tests," *Packaging Technology and Science*, vol. 24, no. 2, pp. 75–87, 2011.

- [4] K. Xu, Y. Wu, and Q. Wu, "Development of vibration loading profiles for accelerated durability tests of ground vehicles," in *Proceedings of the Dynamic Systems and Control Conference and Bath/ASME Symposium on Fluid Power and Motion Control (DSCC '11)*, pp. 717–724, Arlington, Va, USA, November 2011.
- [5] G. J. Yun, A. B. M. Abdullah, and W. Binienda, "Development of a closed-loop high-cycle resonant fatigue testing system," *Experimental Mechanics*, vol. 52, no. 3, pp. 275–288, 2012.
- [6] M. Česnik, J. Slavić, and M. Boltežar, "Uninterrupted and accelerated vibrational fatigue testing with simultaneous monitoring of the natural frequency and damping," *Journal of Sound and Vibration*, vol. 331, no. 24, pp. 5370–5382, 2012.
- [7] A. Pothula, A. Gupta, and G. R. Kathawate, "Fatigue failure in random vibration and accelerated testing," *Journal of Vibration and Control*, vol. 18, no. 8, pp. 1199–1206, 2012.
- [8] Y. Eldogan and E. Cigeroglu, "Vibration fatigue analysis of a cantilever beam using different fatigue theories," in *Topics in Modal Analysis, Volume 7: Proceedings of the 31st IMAC, A Conference on Structural Dynamics, 2013*, Conference Proceedings of the Society for Experimental Mechanics Series, pp. 471–478, Springer, New York, NY, USA, 2014.
- [9] Y. Jiang, J. Y. Tao, and D. Z. Wang, "Simulation of non-Gaussian stochastic processes by amplitude modulation and phase reconstruction," *Wind and Structures*, vol. 18, no. 6, pp. 693–715, 2014.
- [10] Department of Defense, *MIL-STD-810G, Test Method Standard for Environmental Engineering Considerations and Laboratory Tests*, Department of Defense, 2008.
- [11] D. Benasciutti and R. Tovo, "Fatigue life assessment in non-Gaussian random loadings," *International Journal of Fatigue*, vol. 28, no. 7, pp. 733–746, 2006.
- [12] H. W. Cheng, J. Y. Tao, X. Chen, and Y. Jiang, "A method for estimating rainfall fatigue damage of narrowband non-Gaussian random loadings," *Proceedings of the Institution of Mechanical Engineers, Part C: Journal of Mechanical Engineering Science*, vol. 228, no. 14, pp. 2459–2468, 2014.
- [13] H. W. Cheng, J. Y. Tao, X. Chen, and Y. Jiang, "A spectral method to estimate fatigue life under broadband non-Gaussian random vibration loading," *Journal of Vibroengineering*, vol. 16, no. 2, pp. 596–607, 2014.
- [14] H. Cheng, J. Tao, X. Chen, and Y. Jiang, "Fatigue reliability evaluation of structural components under random loadings," *Proceedings of the Institution of Mechanical Engineers, Part O: Journal of Risk and Reliability*, vol. 228, no. 5, pp. 469–477, 2014.
- [15] P. A. Brodtkorb, P. Johannesson, G. Lindgren, I. Rychlik, J. Rydén, and E. Sjö, "WAFO—a Matlab toolbox for analysis of random waves and loads," in *Proceedings of the 10th International Offshore and Polar Engineering Conference*, pp. 343–350, Seattle, Wash, USA, June 2000.
- [16] S. H. Crandall and W. D. Mark, *Random Vibration in Mechanical Systems*, Academic Press, New York, NY, USA, 1963.
- [17] H. Himelblau, D. L. Kern, J. E. Manning, A. G. Piersol, and A. Rubin, "Dynamic environmental criteria: NASA-HDBK-7005," in *NASA Technical Handbook*, NASA, Washington, DC, USA, 2001.
- [18] G. T. Yahr, "Fatigue design curves for 6061-T6 aluminum," *Journal of Pressure Vessel Technology*, vol. 119, no. 2, pp. 211–215, 1997.